



Deliverable

5.1. Basin-scale sectorial drought impacts for future scenarios

Edited by Tobias Conradt

Potsdam-Institute for Climate Impact Research
Telegrafenberg, Potsdam, Germany

Finalized in March 2023

Contents

Preface 5

1 A modelling study of the Havel basin as central part of the German Elbe river basin 7

- 1.1 Introduction 7
- 1.2 Catchment characteristics 8
- 1.3 Materials and methods 13
- 1.4 Calibration results – the *base* run 16
- 1.5 Sensitivity study 19
- 1.6 Scenario modelling 27
- 1.7 Discussion and conclusions 48

2 Crop drought risk in Moldova under global warming and possible crop adaption strategies 51

- 2.1 Introduction 52
- 2.2 Data and Methods 54
- 2.3 Results 59
- 2.4 Discussion and Conclusions 78

3 Data and studies of the Boyne (IE) and Upper Aragón (ES) river basins relevant for future research 83

- 3.1 Boyne River catchment, Ireland 83
- 3.2 Upper Aragón River basin, Spain 86

References 89

Preface

This is the first of three CROSSDRO Deliverables reporting results obtained in Workpackage 5 (WP5). The original idea of WP5 – Scenarios of drought risk and impacts under climate change scenarios – was to deliver a future outlook of what we can expect from drought on the European continent in the upcoming decades, based on the research findings and models developed in the other work packages and utilizing the most advanced climate scenarios available.

While we were able to not only access recent EURO-CORDEX climate scenario data of much higher resolution and quality than expected (Coppola et al. 2021a, Vautard et al. 2021) but also to subject these to a trend-preserving bias-adjustment (Lange 2019) developed at the Potsdam Institute for Climate Impact Research (PIK), there remained two general problems we could not solve within the project run time. First, we could not really finalize the set-up of our models in multiple regions and integrate their results towards a European drought prospect. Producing eco-hydrological scenarios as shown for the Havel basin in Chapter 1 turned out to be extremely resource binding as many model errors (e.g. soil profiles below the maximum depth of plant roots not being considered, or interception storage only working for rain, not snow) became only visible during model calibration and had to be fixed in the first place. Second, the reliability of even the most advanced climate scenarios seems rather questionable when it comes to drought trends. Practically no contemporary dynamical climate model is able to reproduce drought tendencies and trends recently observed in Europe (Piniewski 2022; see also the CROSSDRO-publication of Vicente-Serrano et al. 2022).

Nevertheless we present here our scenario research on the regional level focusing on a relevant part of the German Elbe River basin and on the Republic of Moldova. This has to be seen in context to the case study-related Deliverables and peer-reviewed articles published on behalf of CROSSDRO (Vicente-Serrano et al. 2021a,c; Peña-Angulo et al. 2021; Conradt et al. 2023), the data published from CROSSDRO-funded hydrologic modelling (O'Connor et al. 2021) serving as basis for further drought research in Ireland (O'Connor et al. 2022, 2023), as well as CROSSDRO's share in the development of agricultural drought impact models for climate-driven scenario studies (Conradt 2022). The related Deliverables 5.2 and 5.3 are devoted to the pan-European aspects of drought impacts, scenarios, and data evaluation.

1 A modelling study of the Havel river basin as central part of the German Elbe river basin

*by Henry Engelhardt, Tobias Conradt, Christoph Menz and
Fred F. Hattermann*

1.1 Introduction

Recent years have shown a strong increase in drought intensity and duration in central Europe. In Germany, the years 2018 and 2019 were characterized by extraordinary high temperatures, low precipitation, and record sunshine, especially during spring and summer. Vegetation was suffering under the conditions which showed up through low crop yields (BMEL 2019) and high rates of tree mortality (Obladen et al. 2021). Evaporating the small amount of water resources left in the soils, hardly any water percolated to the aquifers leading to the depletion of groundwater resources (Wriedt 2020). Future climate change is assumed to increase the probability of such drought events (Hari et al. 2020)

The east of Germany was especially suffering under the drought conditions. The mean summer temperature was above 20°C and the climatic water balance was below -50 mm during springs and summers of 2018 and 2019 in most parts of Eastern Germany (DWD 2022). Unlike to other parts of Germany, soils did not fully recover in 2020 and 2021 and the soil drought increased again drastically into September 2022 (UFZ 2022).

Among the most affected regions was the German Havel River basin, a central part of the larger Elbe River basin. Regarding the spatial distribution of precipitation in Germany in the period 1992–2021, 85% of the Havel River basin fell below the 20th percentile (519 mm yr⁻¹), and 44% fell below the 10th percentile (482 mm yr⁻¹) of the spatial distribution of mean precipitation in Germany (own evaluation based on DWD-CDC 2022b). Sandy soils with low water holding capacities complete the characteristics of a water-scarce landscape; lakes and wetlands covering about 10% of the area do not contradict this, because much water is lost from here through evaporation.

We modelled the ecohydrological system of the Havel River basin with SWIM (Krysanova et al. 1998, 2015) to get insights about internal cause-effect chains and system stability under drought conditions. Here we first give an account of the extensive calibration efforts and the resimulation of the recent drought years, then we present a climate scenario analysis to evaluate future drought pressures in the natural systems and specific challenges under climate change.

1.2 Catchment characteristics

1.2.1 Physical features and hydrography

The Havel River basin covers an area of 23,860 km² with 23,790 km² in the East-German federal states of Berlin, Brandenburg, Mecklenburg-Western Pomerania, Saxony-Anhalt, and Saxony (Fig. 1.1). Only a small part of 70 km² near the Spree River spring in the Ore Mountains belongs to the Czech Republic (FGG Elbe 2021). Unless stated otherwise, we use the term Havel area when referring to the German part of the Havel River basin.

The Havel River originates from source lakes close to the Müritz Lake in the Mecklenburg Lake District and joins the Elbe River at the town of Havelberg. The Spree River is the largest affluent of the Havel River and its confluence in Berlin divides the sections of Upper Havel and Lower Havel. At the confluence the Spree contributes the main discharge ($MQ = 28.4 \text{ m}^3 \text{ s}^{-1}$) of almost three times the Havel discharge ($MQ = 10.8 \text{ m}^3 \text{ s}^{-1}$; own calculations for the years 2001–2020 based on data from Wasserportal Berlin 2022a,b).

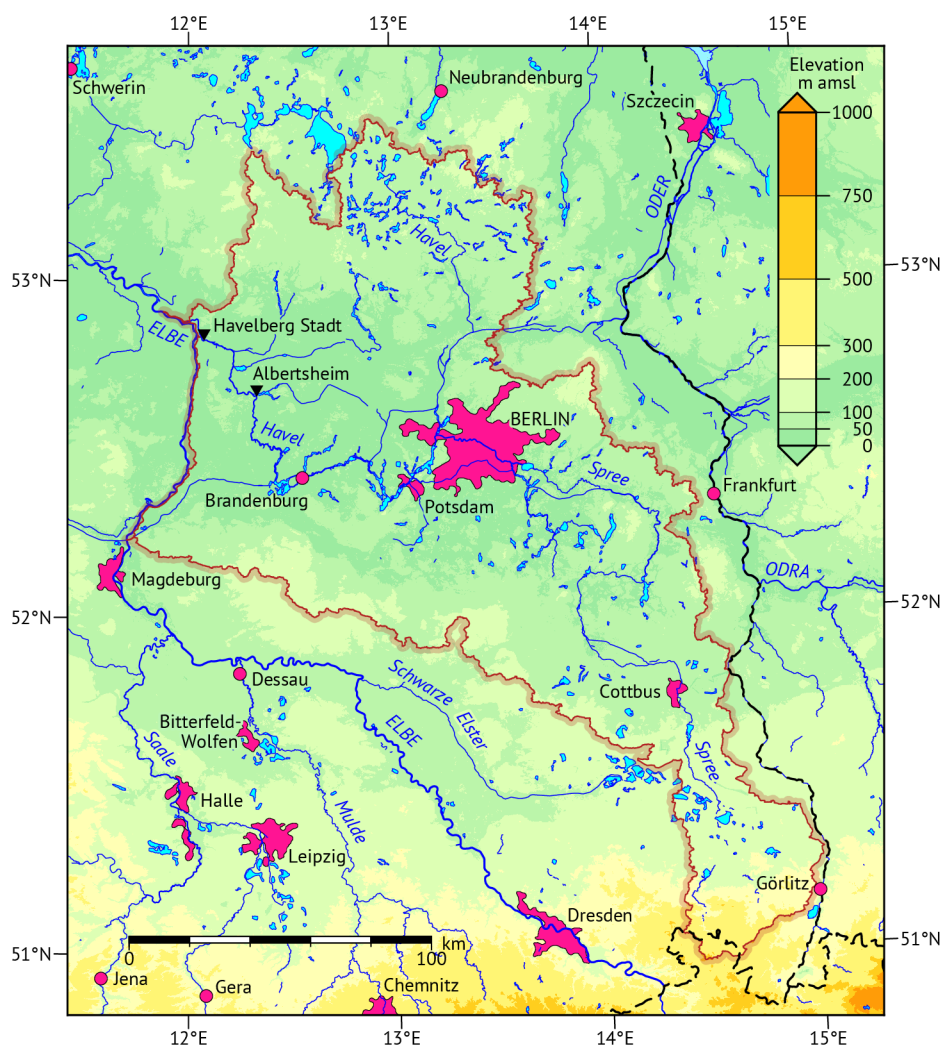


Figure 1.1: Map of the Havel River basin. Data sources: Copernicus (2016, 2020), Eurogeographics (2020), and BfG (2020).

Both-rivers are characterized by very low flow velocities along their courses through the lowlands due to small gradients and occasional stream widenings to river lakes. The natural conditions of the rivers are however often heavily artificially modified by impoundments, different water uses and the channelized water system (LfU 2015). Among the most extensive artificial modifications are processes underlying the operation of open-cast lignite mines in lower Lusatia.

In order to access the lignite, groundwater depletion is a necessary treatment, and for several decades the Spree River discharge was consequently much higher than under natural conditions. At the peak of coal mining in the end of the 1980s (Kohlenstatistik 2019), the additional discharge was $38.1 \text{ m}^3 \text{ s}^{-1}$, whereas in the first years of the 21st century the value decreased to an additional discharge of about $14 \text{ m}^3 \text{ s}^{-1}$ (Schoenheinz et al. 2011) which is further reduced by cooling water evaporation from the power plants and infiltration losses (Kaltofen et al., 2004).

The mining-related water management created a water deficit in the groundwater body and the dry opencast pits. In 1990, the cumulated deficit without active mines was about 9 billion m^3 which was subsequently reduced by river inflows. The annual Spree River contributions amounted to 38–124 million m^3 (equalling average flows of $1.2\text{--}3.9 \text{ m}^3 \text{ s}^{-1}$) in the years 2008–2020 (LMBV 2021). Consequently the area of lakes in Lower Lusatia increased from about 3,000 ha in 1990 to about 7,500 ha in 2013 which is projected to increase to 26,000 ha after the end of open cast mining (Deshaias 2017).

1.2.2 Climatology

Timeseries for temperature and precipitation in the Havel area are presented in Fig. 1.2. The series are calculated from gridded monthly mean weather data (DWD-CDC 2022a,b). Regional values were obtained by averaging over the 1-km grid-cells inside the Havel area.

The average temperature between 1961 and 2021 was 9.2°C . Annual temperature resembles the global warming trend visibly with the highest temperatures on record appearing in the recent drought and heat years 2018–2020. Average annual temperatures exceeded 11.0°C in 2019 whereas the lowest temperature appeared in 1996 with 7.4°C . The linear trend of annual temperatures between 1961 and 2021 exposes an increase of 0.34 K per decade and is highly significant ($p = 2 \cdot 10^{-8}$).

Besides the precipitation extracted from DWD-CDC (2022b), averages from RADKLIM grids (Winterrath et al. 2018) are included in Fig. 1.2 for the years 2001–2020. The 1961–2020 average annual precipitation from interpolated DWD observations amounts to 575.3 mm . Taking into account only 2001–2020, the annual amounts to 591.2 mm which is complemented by 578.1 mm obtained from the RADKLIM grids.

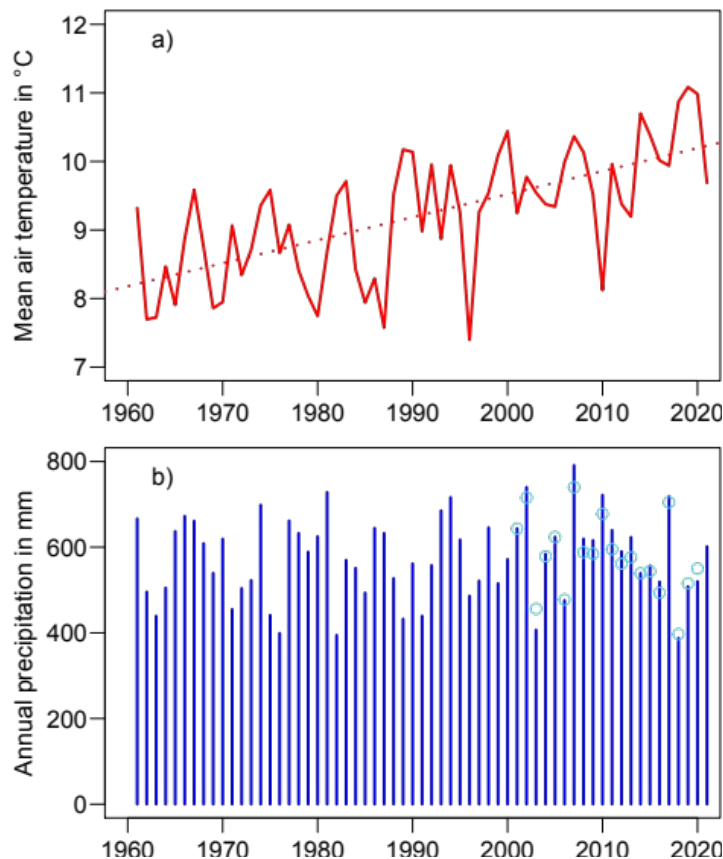


Figure 1.2: Average 2 m air temperature and precipitation timeseries for the German part of the Havel basin generated from monthly DWD grids (DWD-CDC 2022a,b). The dashed line in the temperature graph is a trend line based on linear interpolation. Light blue circles in the precipitation graph (years 2001–2020) are from RADKLIM data (Winterrath et al., 2018).

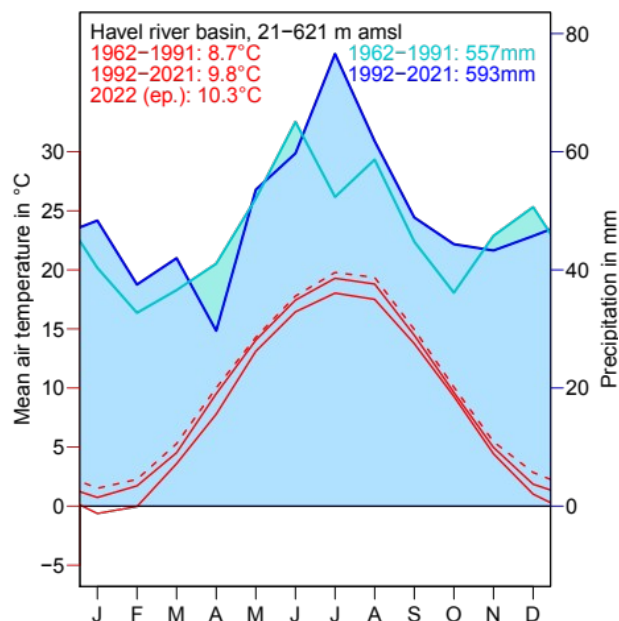


Figure 1.3: Climogram of the Havel area. The lower one of the two solid red line belong to the 1962–1991 period, the upper one to the 1992–2021 period and the dashed red line is an estimation of the monthly average temperature by linear regression. Data comes from monthly DWD grids (DWD-CDC, 2022a, 2022b).

The highest annual precipitation in both series fell in 2007 with 791 mm and 740 mm in the two data sources, respectively. This is also the largest single-year difference between the two grids. The lowest year on record, again in both timeseries, was 2018 with 387.2 mm for the monthly grid and 396.8 mm for the RADKLIM data.

Following Kottek et al. (2006), the Köppen and Geiger classification of the Havel area for the years 1992–2021 is Cfb, a code for temperate humid climate with warm summer (Fig. 1.3). Precipitation is highest in summer but note the fluctuations between the climate normal periods shown in Fig. 1.3. Mean annual precipitation has risen by 35 mm between the two periods. It should be noticed that the Havel climate is not far from another class. Following the approach of Peel et al. (2007), a Dfb code (cold humid with warm summer) must be assigned for the 1962–1991 period, since the coldest month (January) was on average -0.7°C cold back then ($+0.7^{\circ}\text{C}$ in the recent three decades), and Peel et al. use a 0°C limit instead of the -3°C of Kottek et al. (2006).

Mean annual temperature has increased by 1.1 K from 8.7°C in the 1962–1991 period to 9.8°C in the three recent decades. The temperature increase is present in all months and most amplified in winter and spring; autumn exposes the weakest increase.

1.2.3 Soils

The Havel area is dominated by sandy soils with low available field capacity. There are boulder clay and boulder marl on about a third of the area, but often with sandy top layers. More elevated regions are frequently rather pure, sometimes aeolic, sands. Lowlands and glacial valleys – whose fluvial sediments are not rich in clay or silt as well – cover about a fourth of the area (BGR 2014). Also agricultural soils are mostly of poor (54%) or very poor quality (30%) (own calculation, based on BGR 2014). The few exceptions are mountainous loess soils in the very southern part and a small stripe of loess in the central western part of the basin (Mueller et al., 2007; Hennings, Höper and Mueller, 2016).

1.2.4 Land use

The Havel area is dominated by agriculture (46.4%) and forests (39.2%). Most of the forest area are coniferous forests, mostly pines. Settlement areas (approx. 8.5%) concentrate in and around Berlin. There are many lakes and river-lakes, currently covering 2.6% of the area and slowly progressing towards 3.0%, because former open-cast lignite mining pits are slowly being flooded to form new, water-rich landscapes (Table 1.1).

Table 1.1 Land use in the Havel area according to Copernicus (2020). Categories covering less than 0.1% are summarized under Other.

CLC Category		Area	Share
Code	Land use	km ²	%
111	Continuous urban fabric	48.34	0.20
112	Discontinuous urban fabric	1,535.18	6.46
121	Industrial or commercial units	345.39	1.45
124	Airports	38.85	0.16
131	Mineral extraction sites	175.39	0.74
141	Green urban areas	53.69	0.23
142	Sport and leisure facilities	169.72	0.71
211	Non-irrigated arable land	7,223.88	30.39
222	Fruit trees and berry plantations	26.92	0.11
231	Pastures	3,526.90	14.83
243	Agriculture, with significant areas of natural vegetation	253.35	0.15
311	Broad-leaved forest	1,013.53	4.26
312	Coniferous forest	7,829.18	32.93
313	Mixed forest	480.69	2.02
321	Natural grasslands	71.48	0.30
322	Moors and heathland	214.59	0.90
324	Transitional woodland-shrub	218.19	0.92
411	Inland marshes	65.43	0.28
511	Water courses	50.58	0.21
512	Water bodies	606.02	2.55
XXX	Other	43.68	0.18
TOTAL		23,774.75	100.0

1.2.5 Population

The population of the Havel basin grew from 5.378 million inhabitants in the census year 2011 to 5.847 million at the end of 2020, this means an average annual surplus of about 55,000 people or 1%. Most of this growth can be attributed to the city state of Berlin, the most densely populated area in the basin with a population of about 3.664 million people at the end of 2020 (4,112 per km²) (DESTATIS 2021 and own GIS analyses). The population growth was projected to slow to more moderate rates between 3 and 24 thousand additional inhabitants per year between 2021 and 2030 (Senatsverwaltung 2019).

1.3 Materials and Methods

1.3.1 The SWIM model

We investigated the eco-hydrological trends in the Havel basin under climate change scenarios. For the assessment we used the Soil and Water Integrated Model (SWIM) (Krysanova et al. 1998, 2000). The model allows analysis of climate change impacts on hydrological processes, agricultural production and water quality.

SWIM uses sub-basins and hydrotopes as geographical units. Sub-basins are defined by the catchment system and consist of multiple hydrotopes which are distinguished by land use, soil type and elevation. Processes concerning water, crop- and vegetation growth and nutrients are performed for each hydrotope, and outflows are aggregated for river routing on the sub-basin level (Krysanova et al. 2000).

The model requires six climate variables on a daily time step: average, minimum, and maximum temperature; precipitation; relative humidity; and solar radiation. Among the possible outputs are river runoff at subbasin outlets, data for evapotranspiration mapping, soil moisture, or agricultural yields.

1.3.2 Weather and climate scenario data

Historical weather data were observation time series of weather stations by the German Weather Service (DWD) obtained via their Climate Data Centre (DWD-CDC, 2022c). The data we used were limited to the years 2001–2020 due to the parallel availability of RADKLIM, consistently radar-interpolated precipitation data in 1-km resolution (Winterrath et al. 2018).

The station measurements were interpolated towards the 669 SWIM sub-basins using the R software package gstat (Pebesma 2004; Gräler et al. 2016), the gridded precipitation data were averaged within each sub-basin.

The climate scenario data are based on CMIP5 EURO-CORDEX simulations at 0.11 degrees (approx. 12.5 km) resolution (Jacob et al. 2014; Coppola et al. 2021a, Vautard et al. 2021). We used 21 simulations from the RCP 8.5 scenario (IPCC 2014) for the 21st century. The forcing global climate models (GCMs) are listed in Table 1.2 and the regional climate models (RCMs) in Table 1.3. The scenario simulations were bias-adjusted at PIK with the ISIMIP3BASD v2.1 approach (Lange 2019) using E-OBS data (Cornes et al. 2018) as reference. Seventeen realisations cover the 95-year-period 2006–2100 whilst the Hadley model driven realisations Hc, Hd, Hk, and Hs already end by 2099.

Table 1.2 Global climate models forcing the EURO-CORDEX simulations

Acronym	Origin	Letter
CERFACS-CNRM-CM5	Centre National de Recherches Météorologiques—Groupe d'études de l'Atmosphère Météorologique (France) and Centre Européen de Recherche et de Formation Avancée (CERFACS)	F
EC-EARTH	Irish Centre for High-end Computing (Ireland)	E
HADGEM2-ES	Met Office Hadley Centre (United Kingdom) and Instituto Nacional de Pesquisas Espaciais (Brazil)	H
MPI-ESM-LR	Max-Planck-Institut für Meteorologie (Germany)	M
NCC-NORESML-M	Norwegian Climate Centre (Norway)	N
IPSL-CM5A-MR	Institut Pierre-Simon Laplace (France)	I

Table 1.3 Regional climate models working in the EURO-CORDEX domain

Acronym	Origin	Letter	Runs
CCLM	Climate Limited-area Modelling Community (CLM-Community)	c	Ec, Fc, Hc, Mc
HIRHAM	Danish Meteorological Institute (DMI)	d	Ed1, Ed2, Ed3, Fd, Hd, Nd,
RACMO	Royal Netherlands Meteorological Institute (KNMI)	k	Ek1, Ek2, Ek3, Fk, Hk,
RCA	Swedish Meteorological and Hydrological Institute (SMHI)	s	Es1, Fs, Hs, Is, Ms, Ns

In the following, single simulation runs will be referred to by their GCM-RCM combination indicated by two letters, the capital letter given in the last column of Table 1.2 and the lowercase letter in the second-last column of Table 1.3. In case of variant runs generated by the same model chain, numbers are used for differentiation, e.g. Ek3. All combinations are listed in the last column of Table 1.3

The bias-adjustment approach ISIMIP3BASD (Lange, 2019) is based on a parametric quantile mapping procedure. The fundamental assumption of the quantile mapping approach is that modelled values are biased, but the distribution is correct. Therefore, observational data is necessary to establish a quantile-dependent correction function which is applied to the quantiles of the simulated variable. The approach preserves trends and was extended for handling multivariate data. However, for the present dataset the univariate version was used. Trend preservation was only applied to variables with a significant trend, namely mean temperature and air pressure (the latter not being relevant for this assessment). Minimum and maximum temperature were not directly bias adjusted but the temperature range considering the skewness of temperature.

The observational data for the bias corrections consisted of two data sets. One was the German part of the ensemble version of the E-OBS temperature and precipitation data sets v23.e (Cornes et al. 2018), and the other one was a combination of a gridded ground observation dataset of the German weather service (DWD) interpolated with the REGNIE procedure (Rauthe et al. 2013) and a PIK-made grid-interpolation of the DWD station observations.

1.3.3 Discharge and cropping data for model calibration

River discharge measurements for the period 2001–2020 were provided by LfU Brandenburg, the state authority for environment, for the downstream Havel gauges Albertsheim (52°39'21"N, 12°20'01"E; catchment area covering approximately 82 % of the river basin) and Havelberg-Stadt (52°49'24"N, 12°04'36"E; practically the basin outlet) were used for model calibration and validation. The discharge data for Havelberg-Stadt were adjusted for negative values indicating phases of inversed flow during the passage of extreme flood waves in the Elbe river, e.g. in August 2002. Months including the negative discharges and the preceding months were excluded from the analysis.

Silage maize (SLMA), winter wheat (WWHT) and winter rape (RAPE) are the most frequently grown crops with a cumulated area share of about 50 % (20 % each for SLMA and WWHT and 10 % for RAPE (cf. DESTATIS 2021a). This distribution was approximated in SWIM by time-shifted crop rotation schemes in the agricultural hydrotopes (Table 1.4); most other crops in the landscape are cereals with similar growth dynamics, so they are not explicitly considered. The yields were calibrated by growth parameters (Table 1.5) targeting the average yields in Brandenburg between 2011 and 2017 (the seven years before the drought) which were 68.3 dt ha⁻¹ for WWHT, 34.1 dt ha⁻¹ for RAPE, and 340.3 dt ha⁻¹ for SLMA.

Table 1.4: Crop rotation scheme used in SWIM. Up to three operations (op1–op3) on Julian days (day1–day3). The tags + and – mean sowing and harvesting, respectively, and / indicates no operation.

Year	op1	day1	op2	day2	op3	day3
1	SLMA+	115	SLMA–	269	WWHT+	270
2	WWHT–	210	RAPE+	220	/	/
3	RAPE–	200	/	/	/	/

Table 1.5: Basic specific parameters for agricultural crops used in SWIM

Crop	base temperature	optimum temperature	heat units
	°C	°C	–
SLMA	5.0	25	2400
WWHT	–0.5	18	2300
RAPE	0.0	17	2500

1.4 Calibration results – the *base run*

The simulated discharge during the calibration period 2002–2012 was about 2% higher than observed in Havelberg-Stadt. The high correlation level for the annual-daily average discharge with an R^2 of 0.972 and a Nash–Sutcliffe coefficient (NSE) of 0.936 replicate the observation extremely well.

As expected, given the decreasing groundwater discharge from mining, the validation for the years 2013–2020 showed the volume overestimation increased to about 7%. The R^2 decreased slightly to 0.956, and the NSE dropped to 0.827. Especially the low discharges during spring were overestimated by the model.

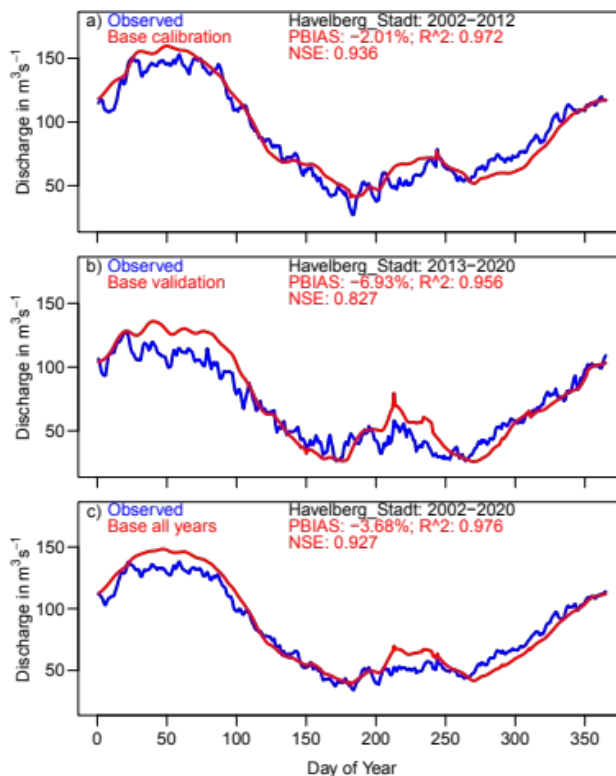


Figure 1.4 Annual daily discharge for Havelberg-Stadt in the calibration (a) and validation period (b) and in all years (c).

Figures 1.4 and 1.5 show that the annual cycles are well simulated. Winter discharge is mostly overestimated. The largest underestimation appears in 2011. The reason for this underestimation is probably related to inaccurate precipitation in the RADKLIM data which could also explain the large difference to the monthly grid aggregations (Fig. 1.2b). Low discharge is modelled more accurately, especially well during the low flow periods in the drought years 2003 and 2018–2020.

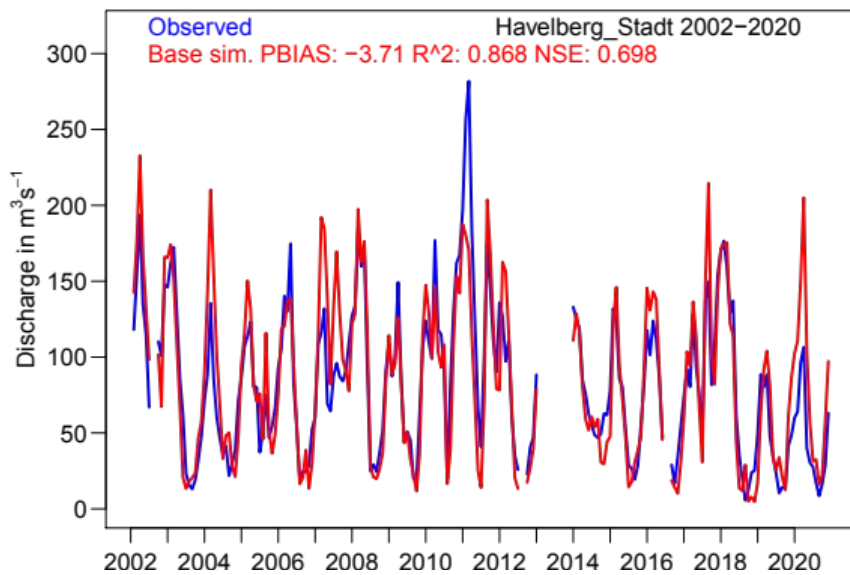


Figure 1.5: Monthly timeseries of observed and simulated discharge at Havelberg-Stadt.

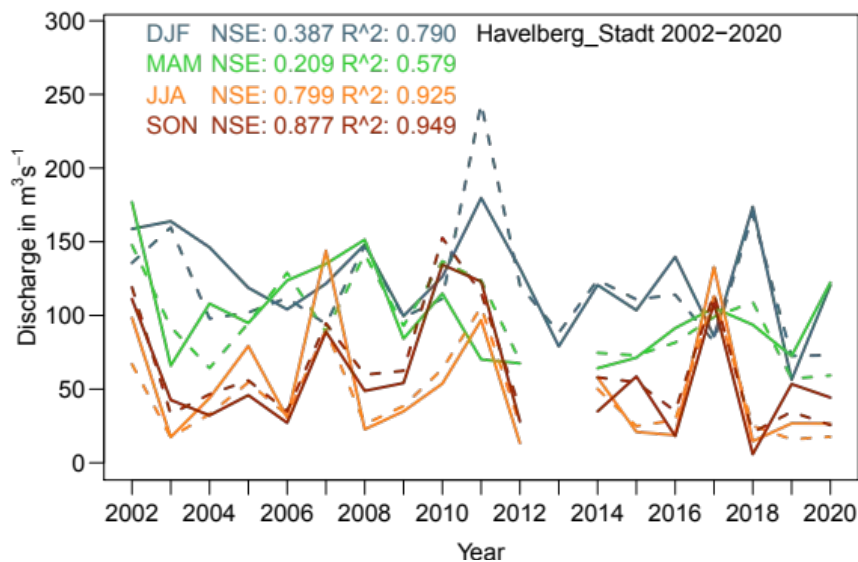


Figure 1.6: Observed and simulated seasonal discharges for Havelberg-Stadt. The DJF values include December discharges from the respective foregoing years.

Figure 1.6 presents seasonal time series. Regarding NSE and Pearson correlation, autumns are most accurately modelled followed by the summer season, probably because the well-simulated low flow phases concentrate during this part of the year.

Mean crop yields in the 2002–2020 period in the base run were 281.3 dt ha⁻¹ for SLMA, 78.1 dt ha⁻¹ for WWHT, and 41.9 dt ha⁻¹ for RAPE. The modelled yields resemble the Brandenburg observations sufficiently with a maximum relative difference of 20% for WWHT (Table 1.6).

Table 1.6: Time averages of observed agricultural yields in Brandenburg (DESTATIS 2012ff) and averaged yields modelled for the Havel area.

2012–2017	SLMA	RAPE	WWHT
	dt ha ⁻¹	dt ha ⁻¹	dt ha ⁻¹
Observation	340.3	34.1	68.3
Simulation	287.8	40.9	78.3
relative Difference	-15.4%	14.6%	20.0%

1.5 Sensitivity study

For testing the hydrological drought effects of potential climatic shifts (and the plausibility of the model) a sensitivity study was pursued. The variables evapotranspiration, radiation, precipitation and temperature were deliberately altered for that purpose. Radiation and potential evapotranspiration (ETp) were individually increased by 5% and 10% (*ep105*, *ep110*, *rad105*, *rad110*), temperature was increased by 1K and 2K (*T1*, *T2*) and precipitation was reduced by 5% and 10% (*p95*, *p90*).

1.5.1 Discharge

Annual discharges at Havelberg-Stadt were reduced in all sensitivity runs during the 2002–2020 period (Fig. 1.7). The daily discharges of the average year are below the Base run on all days but in winter in the *T1* and *T2* runs. This is due to precipitation form change from snow to rain of 5.8 mm a⁻¹ and 8.7 mm a⁻¹, a reduction of the appearance of snow of 35% and 54%, respectively, resulting in concentrated winter runoff. Strongest effects in terms of discharge were observed for the reduction of precipitation by 5% and 10%. In the *p90* run, annual average discharge reduced from 84.8 m³ s⁻¹ in the *base* run to 69.0 m³ s⁻¹ in the *p90* run which is a reduction of 20.9 mm a⁻¹ (–18.6%). The *rad110* run and the *ep110* run both end up in average discharge reduced by about 7%.

Table 1.7 summarizes the changes of discharge relative to the *base* run. The relative change is most pronounced in summer and autumn of the *p90* run with about a quarter less discharge during these seasons. The only season with an increase in discharge is the winter season in run *T1*. As mentioned above, this is due to changes in snowfall. The highest sensitivity in terms of relative discharge change divided by relative change in the input variable is found for the reduction of precipitation with a nearly twofold effect on annual discharge.

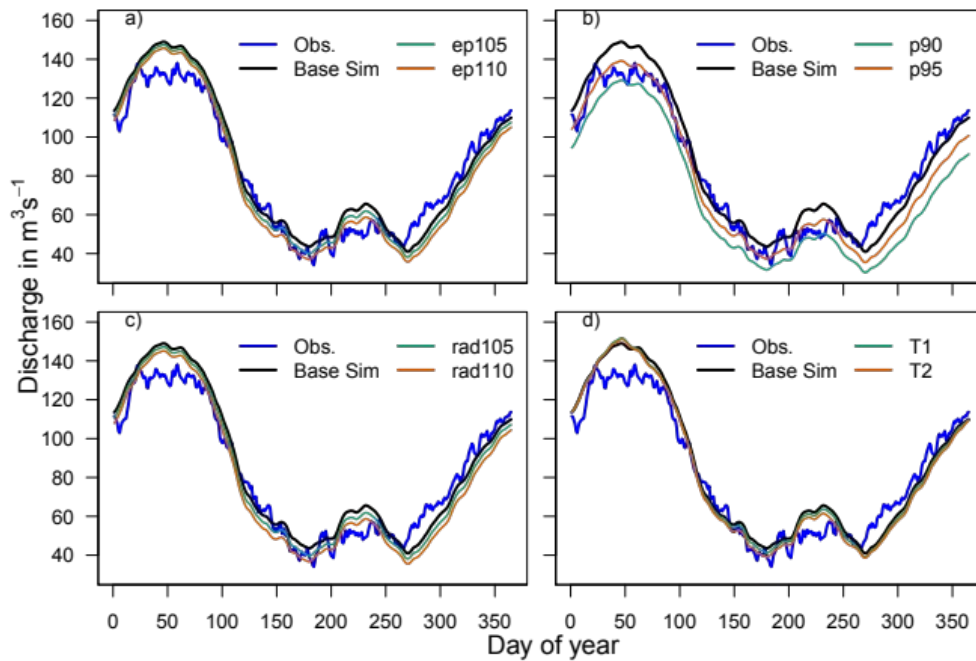


Figure 1.7: Observed and simulated discharge with the simulated discharge in the sensitivity runs, a) evapotranspiration, b) precipitation, c) radiation and d) temperature.

Table 1.7: Change of sensitivity run discharges towards the base run.

Run	Relative change of discharge in %				
	Winter	Spring	Summer	Autumn	Year
ep105 (+5%)	-1.7	-2.8	-6.4	-5.6	-3.5
ep110 (+10%)	-3.5	-5.5	-11.9	-10.7	-6.7
p95 (-5%)	-7.6	-7.9	-12.8	-12.5	-9.4
p90 (-10%)	-15.5	-15.8	-24.5	-24.5	-18.6
rad105 (+5%)	-1.9	-3.2	-6.5	-5.9	-3.7
rad110 (+10%)	-4.0	-6.2	-12.1	-11.3	-7.2
T1	+0.2	-1.6	-3.4	-3.2	-1.5
T2	-0.4	-2.6	-7.3	-5.5	-3.1
	Differential quotient of change of the variable and change in discharge				
ep105 (+5%)	-0.35	-0.56	-1.27	-1.12	-0.70
ep110 (+10%)	-0.35	-0.55	-1.19	-1.07	-0.67
p95 (-5%)	1.53	1.59	2.56	2.49	1.88
p90 (-10%)	1.55	1.58	2.45	2.45	1.86
rad105 (+5%)	-0.39	-0.63	-1.31	-1.17	-0.75
rad110 (+10%)	-0.40	-0.62	-1.21	-1.13	-0.72

1.5.2 Evapotranspiration

Seasonal differences between *base* run and sensitivity runs are presented in Fig. 1.8 for the actual evapotranspiration (ETa). ETa is increased in all runs except those with reduced precipitation. The highest increases towards the base run is modelled for spring, led by the runs with a ten percent increase in radiation and ETp. Runs with a temperature increase experience an increase in spring whereas there is almost no change in summer and a slight increase in autumn evapotranspiration. The highest deficit for runs with reduced precipitation is modelled for summer; the other seasons are less affected.

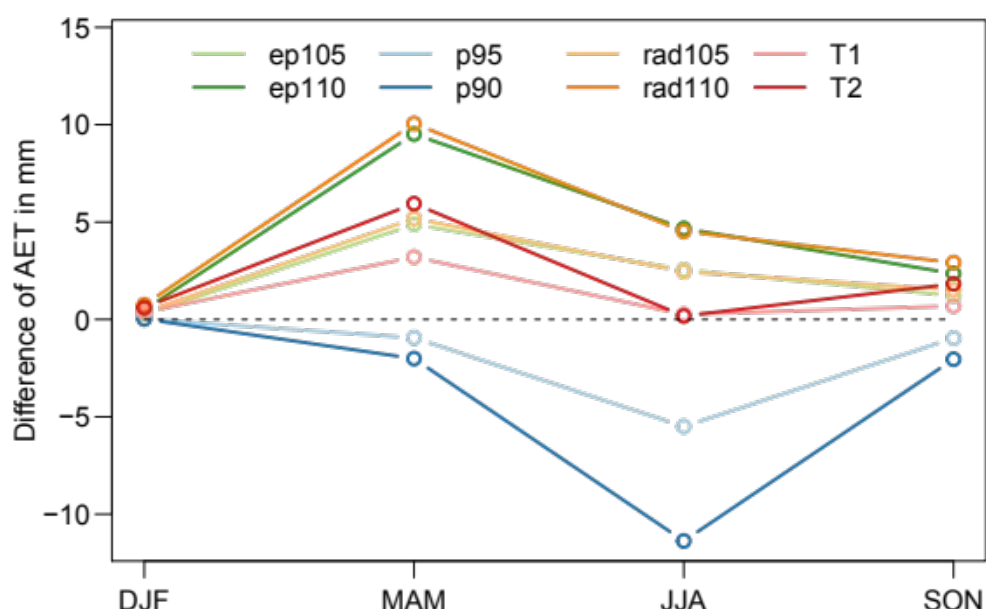


Figure 1.8: Seasonal ETa differences between *base* and sensitivity runs

1.5.3 Soil water

Seasonal changes in soil water index (SWIND) effected by switching from *base* to the sensitivity runs are shown in Fig. 1.9. Whereas there are small changes in the winter season due to sufficient precipitation and low evapotranspiration, changes are increasing in spring and summer. The runs with increased temperatures reach the highest effect on SWIND in spring owing to an earlier start of the growing season and enhanced evapotranspiration rates but also caused by changes in snowfall and snowmelt. Other runs experience the strongest change in summer. This is most pronounced for increased radiation and potential evapotranspiration, followed by the runs with decreased in precipitation. In all experiments, the differences decrease slightly from the summer to the autumn season, however maintaining a high effect level.

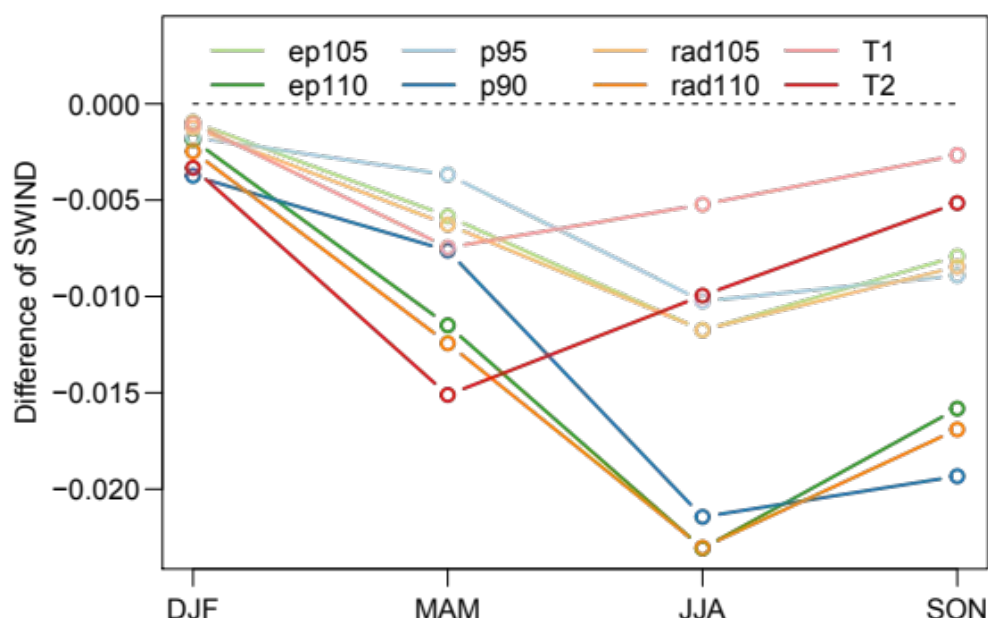


Figure 1.9: Seasonal SWIND differences between base and sensitivity runs

1.5.4 Groundwater recharge

The seasonal effects of the alterations in the sensitivity runs on groundwater recharge (GWRCH) are shown in Figure 1.10. The effects are negative in all run and season combinations except for the runs with increased temperature in winters. This is again due to changes in snowfall and snowmelt as well as soil temperature – frost is limiting percolation. The strongest effects in all seasons come with the reduction of precipitation by 10%. Other runs show still comparable effects with the least ones for temperature change. As for SWIND, the strongest negative effects under temperature increase are found in spring.

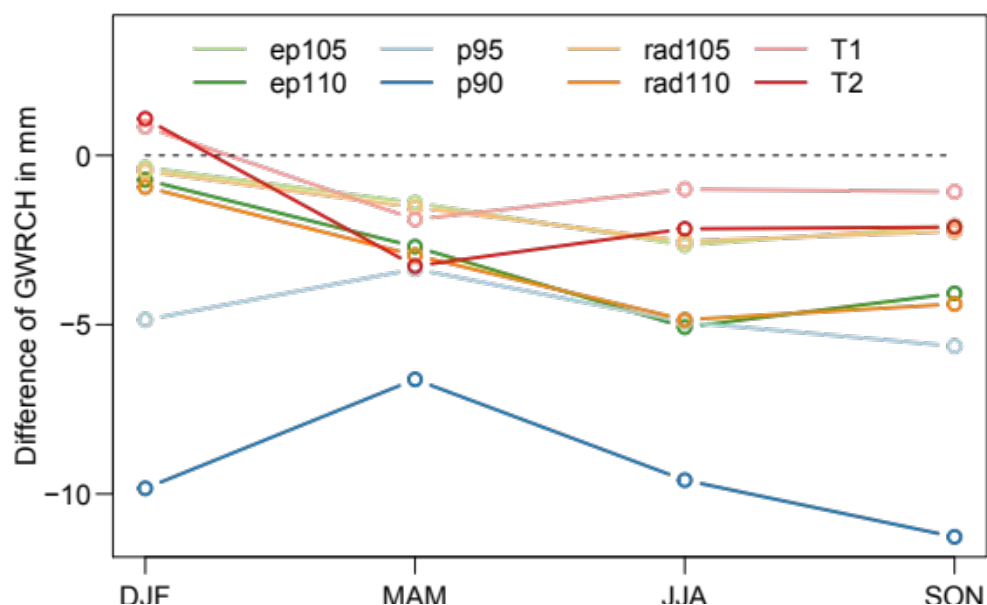


Figure 1.10: Seasonal GWRCH differences between *base* and sensitivity runs

The relative seasonal changes in the sensitivity runs shown in Figs 1.9 and 1.10 motivated the investigation of long term trends. While we could not determine statistically significant linear trends in the sensitivity runs, there are several continuous tendencies to observe (Figs 1.11 and 1.12).

Regarding the winter season, all alterations amplifying ETa (*ep105*, *ep110*, *rad105*, *rad110*, *T1* and *T2*) or decreasing the water availability (*p95*, *p90*) show a negative effect on GWRCH, already receding in *base*, increasing over time. A strong negative value in year 2019 is especially notable. During the drought year 2018 soil water declined. With an even more intensive drought modelled in the sensitivity runs, the soil water content lands far below the *base* level in the end of year 2018. Therefore, the deficit was replenished with water missing in the winter season's groundwater recharge, consequently affecting the groundwater storage in 2019. In other years (and generally in the *base* run) the water supply in autumn and early winter is sufficient to fill both, the small gap in soil water content and the groundwater to a comparable level.

Changes in winter GWRCH in the *T1* and *T2* runs are also determined by the precipitation form (see Fig. 1.12). There is a well-established correlation between the relative change of GWRCH in their winter seasons and the winter snow rates in the *base* run with $R^2 = 0.78$ in both runs.

The time series patterns of seasonal relative changes in spring and summer are similar over all runs with tendencies towards smaller alterations over time, especially in spring beginning from 2013 on. Since GWRCH is of much lower level in spring and summer than in winter, and summer groundwater recharge is predominately limited to short-term storm events, this must not be over-interpreted.

Impacts in autumn tend to increase over time in a similar way as seen in the winter season. The year 2018 is again outstanding in all runs except those with temperature alterations. However, there are comparably low relative changes in several years in the autumn season. The relative changes in autumn correlate to a high degree ($R^2 > 0.88$) with the GWRCH level in the *base* run in all runs but *T1* and *T2*. This means that in autumns with high GWRCH in the *base* run the relative decrease in the sensitivity runs is low and vice versa.

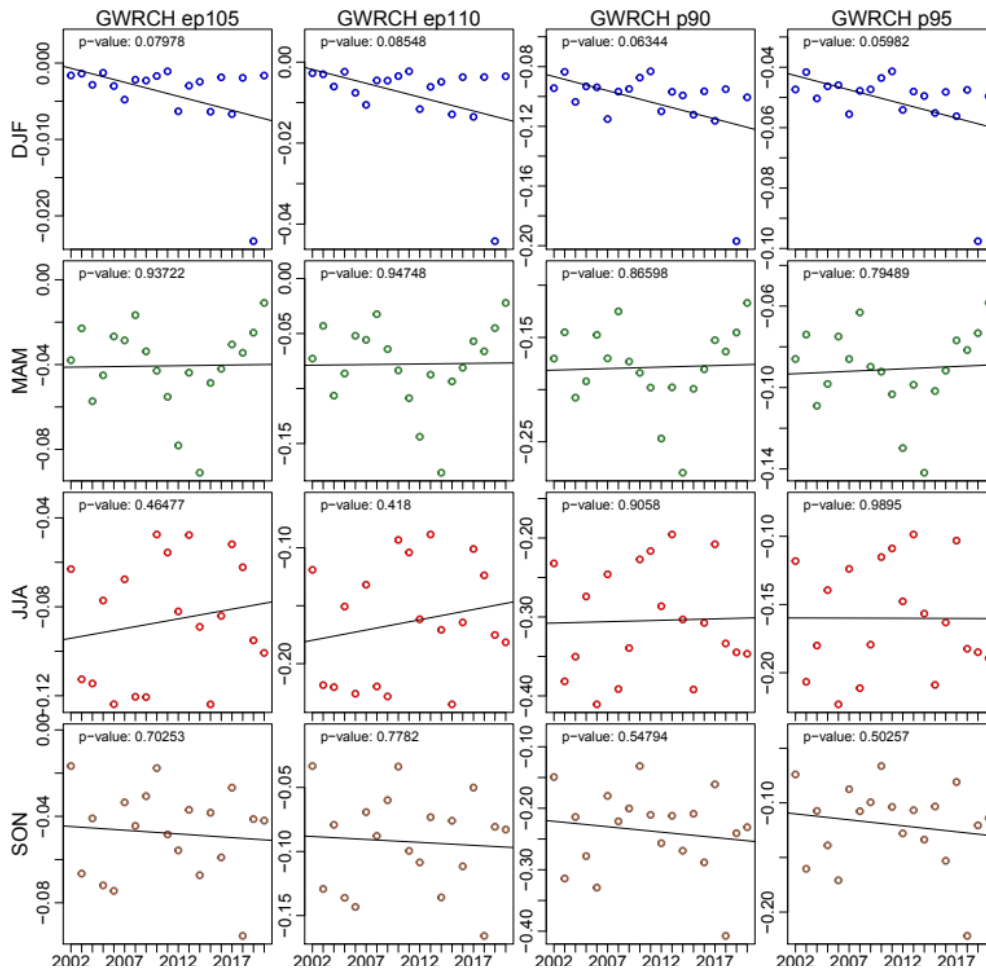


Figure 1.11: Relative seasonal change in GWRCH between the base run and four sensitivity runs. The straight black line is the linear trend line with the corresponding p-value in the upper part.

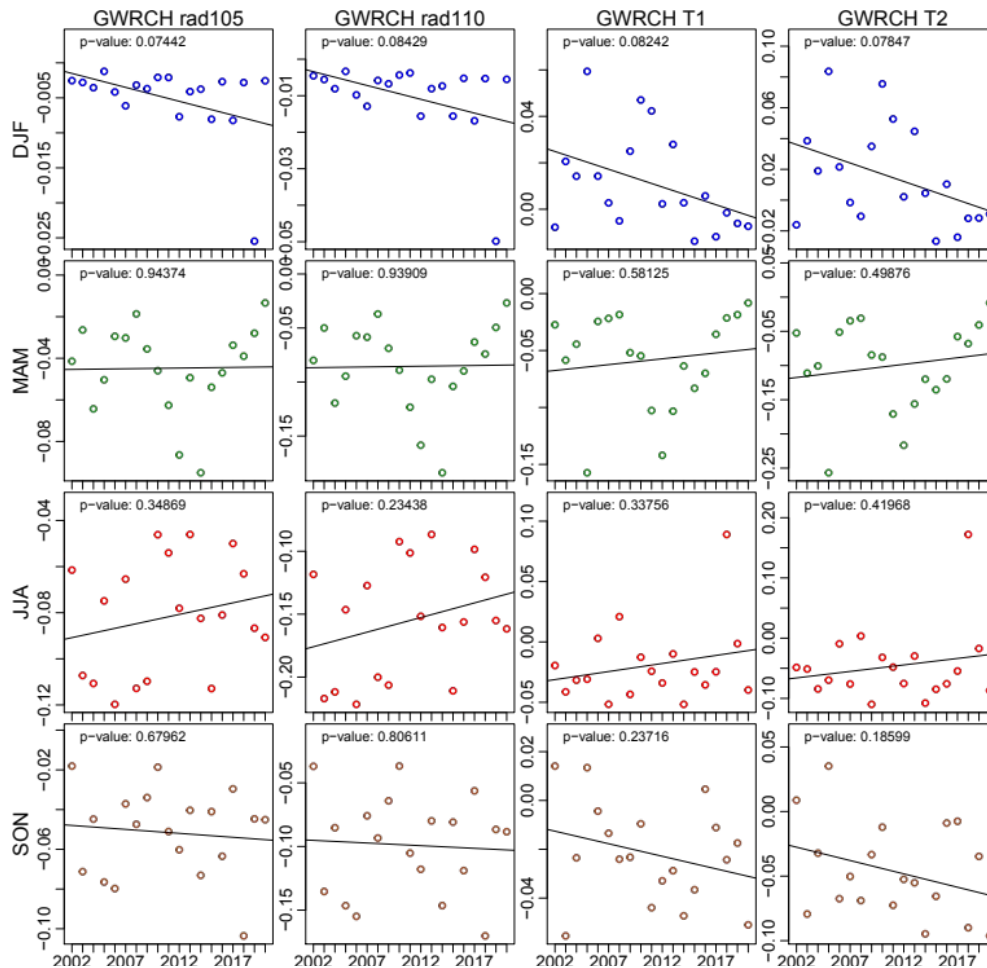


Figure 1.12: Relative seasonal change in GWRCH between the base run and four sensitivity runs. The straight black line is the linear trend line with the corresponding p-value in the upper part.

1.5.5 Crop yields

Crop yields reacted differently towards the changes implemented for the sensitivity study. Average RAPE and WWHT yields experienced minor changes for the evapotranspiration increase (*ep105*, *ep110*) and decrease in precipitation (*p95*, *p90*) but were clearly sensitive towards radiation with increases of about 8% and 6% under *rad105* and *rad110*, respectively. Strong negative impacts were registered for the *T2* run with RAPE and WWHT yields decreasing about 27% and 15%, respectively. SLMA however profited from the higher temperatures under *T2* with yield increases of 5%.

Boxplots in Fig. 1.13 show the distribution of mean annual crop yields in the sensitivity runs. It corroborates that RAPE and WWHT react similar towards the applied changes. Furthermore, the range of annual yield fluctuations for SLMA was most pronounced in the *T2* run. The interquartile range of WWHT yields in the *T1* and *T2* is smaller than in the *base* and all other sensitivity runs. In the *T1* run, the minimum yield is higher than in the *base* run, whereas the median value of the annual yields is far below the *base* mean. This is due to a better performance of WWHT yields with elevated temperature in wet and cold years. In the *T2* run,

WWHT yields minima are again lower than in the *base* run. In *T2*, temperature and water stress prevail over the positive effect of the temperature increase.

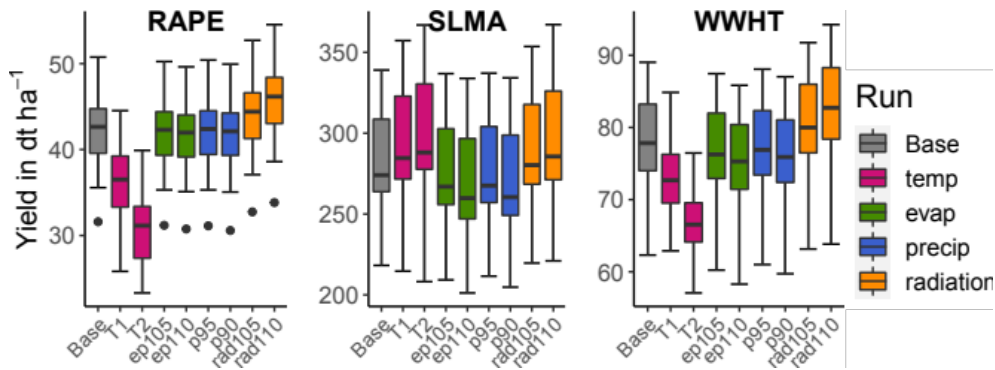


Figure 1.13: Mean annual crop yields in the Base run and in sensitivity runs between 2002 and 2020. In case of outliers, whiskers are drawn until 1.5 times interquartile range (IQR). Without outliers, whiskers reach until the minimum and maximum value.

1.6 Scenario modelling

We also ran the eco-hydrological model with the climate scenario consisting of 21 bias-adjusted EURO-CORDEX realisations (cf. Sub-section 1.3.2) Daily data for the 669 sub-basins – maximum, minimum, and average temperature, precipitation, air humidity, and solar radiation – were spatially aggregated from the overlapping grid cells by weighted averaging considering truncated cells. The first five years (2006–2010) were used for model initialization (spin-up) and are therefore missing in the examination. The realisations were subdivided in three scenario periods from 2011 to 2040, 2041 to 2070 and 2071 to 2100 (from now on *fut1*, *fut2*, and *fut3*, respectively). Before reporting any modelling results we evaluate the climate scenario data as such.

1.6.1 Precipitation

Figure 1.14 shows the distributions of annual precipitation sums in the scenario. The mean value of the *base* run is on a similar level with the first years of the realisations. However, some years are far below the 10th percentile of the realisations (2018–2020). In the years 2011–2020 which are covered by both the realisations and the *base* run, nine out of ten runs are below the realisations' median precipitation and five out of ten runs fall in the lower 25% of the realisations' annual sums.

Precipitation increases steadily throughout the scenario period. The corresponding gradient derived from linear trend estimation of the medians amounts to 8.3 mm per decade at a confidence level of $p < 10^{-5}$.

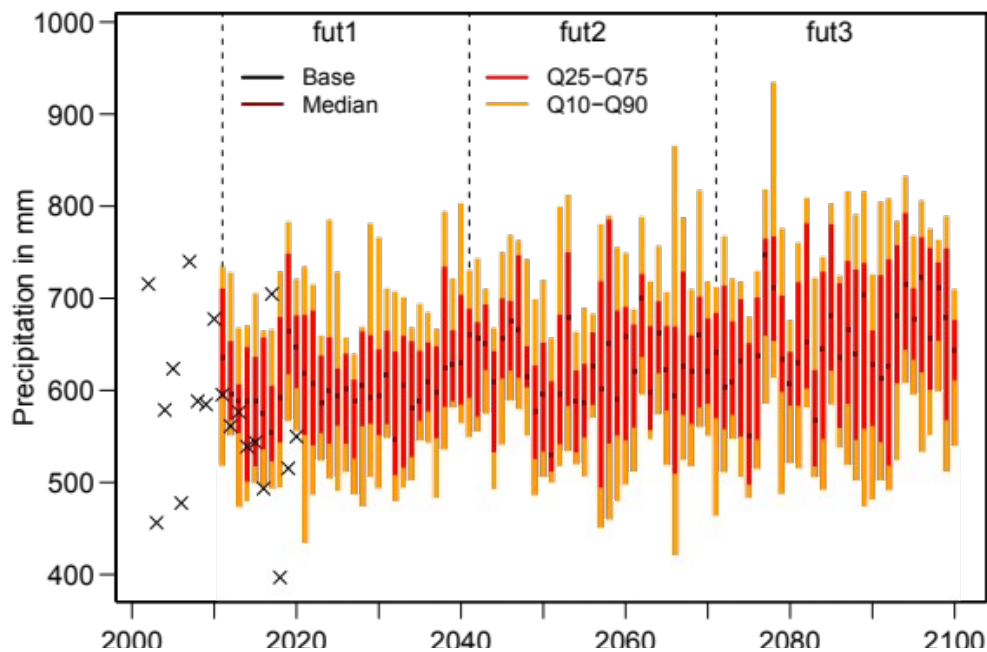


Figure 1.14: Timeseries of the annual precipitation sums (spatial averages of the Havel area). The dark red points are the realisations' median annual precipitation sums. The red bars are the interquartile range and the orange bars the inner 80% of the realisations. Black crosses mark the annual precipitation sums of the base run.

The period means of the annual precipitation medians are 602 mm in *fut1*, 627 mm in *fut2*, and 652 mm in *fut3*. The standard deviations of the actual precipitation rates are also increasing over the *fut* periods from 88.3 mm in *fut1* over 97.2 mm in *fut2* to 108.4 mm in *fut3*. This increase is also perceivable in the spread of the interquartile and Q10–Q90 ranges.

Figure 1.15 shows the monthly median precipitations in the three scenario periods. It can be seen that the monthly precipitation rates do not change consistently; the December–July median values increase compared to the *base* run. Throughout the periods, the highest increases are projected for May and December with 17.8 mm (44%) and 17.6 mm (51%), respectively. Precipitation decreases are found for late summer and autumn months. With a minimum value of –6.2 mm (–13%) in October of *fut1*, the decreases are small exceptions compared to the high relative and absolute increases. October also experiences strong increases in the following periods, so these observations should not be over-interpreted. It must be generally kept in mind that the medians of the *base* run are calculated from only 19 annual months.

Comparing only the scenario periods, the median monthly precipitation increases in all months but June, August and September from *fut1* to *fut2* and all runs in all months except April, August and September from *fut2* to *fut3*. Relative to *fut1*, the highest increase to *fut2* amounts to 4.7 mm (9%) in May and in *fut3* to 19.5% in October. The highest relative decreases between the periods are projected for August from *fut1* to *fut2* with –3.8% and for September from *fut2* to *fut3* with –7.5%.

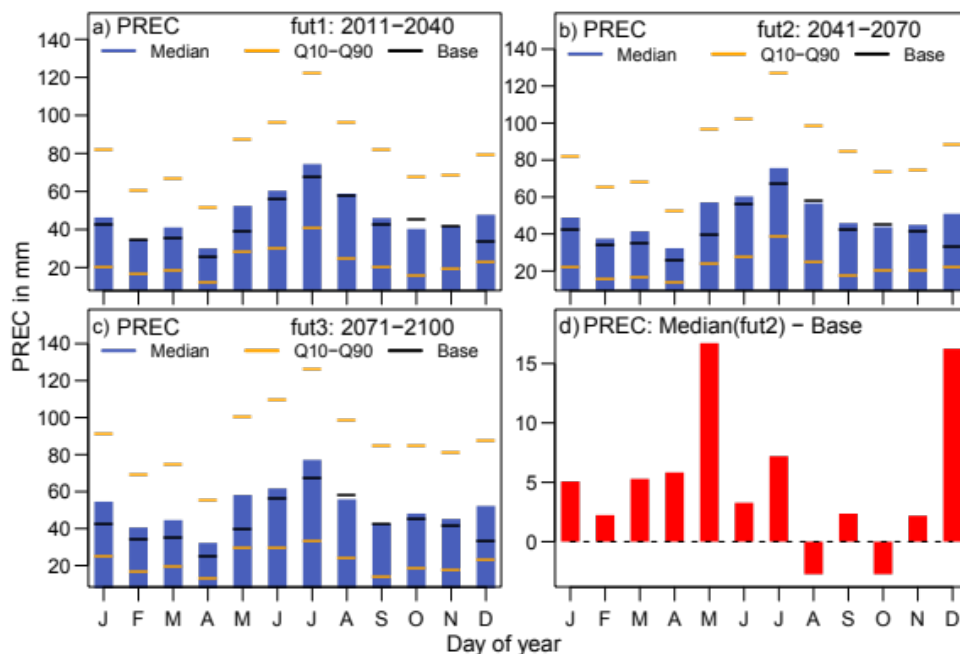


Figure 1.15: a)–c) Annual cycles of precipitation in the *fut*-periods. Blue bars are the median monthly precipitation rates. The orange lines indicate the 10th and 90th percentiles of the realisations. Black lines are the median values of the *base* run. d) Differences between *fut2* and *base*.

The spatial distribution of precipitation in the sub basins in *fut1* is shown in Figure 1.16a. As in the *base* run, topography plays the major role in precipitation rates with higher precipitation in the southern end located in the Ore Mountains, a small mid-western part located in the hills of Hohe Fläming, and in the slightly elevated northern part of the basin. The projected change towards *fut3* is shown in Figure 1.16b. The highest increases are projected for regions with high precipitation in *fut1*. Exceptions are the northwestern edge and the southernmost part of the Havel area which experience low increases.

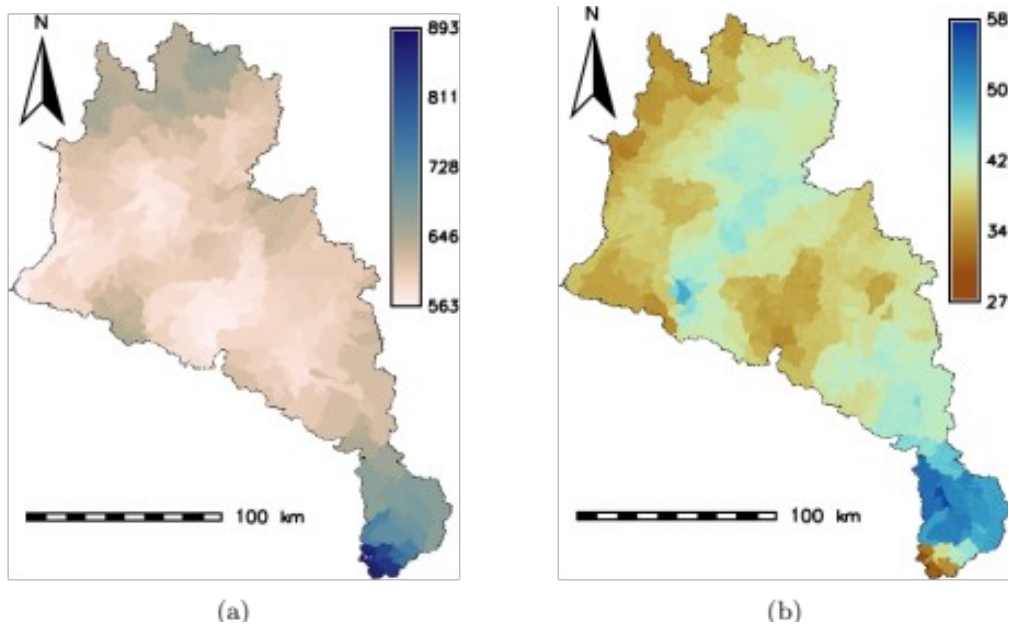


Figure 1.16: Spatial distribution of precipitation a) in *fut1* and b) as difference between *fut3* and *fut1*.

1.6.2 Temperature

Average temperature is steadily increasing in all realisations over the modelled period. The average temperatures for the scenario periods amount to 10.2°C in *fut1*, 11.2°C in *fut2* and 12.7°C in *fut3*. This warming trend is shared by all realizations. The linear regression over all annual averages results in gradients ranging from 0.34 K per decade in realisation *Nd* to 0.57 K per decade in realisation *Hc* with a median value of 0.42 K per decade. The four warmest realisations were forced by the HadGEM2 GCM with average temperatures exceeding 13°C in *fut3*.

Figure 1.17 shows the annual mean temperatures in the scenario period and in the *base* run. The temperatures in the first years of the realisations are close to those in the *base* run. The standard deviations of annual mean temperatures increase from 0.87°C in *fut1* to 0.95°C in *fut2* and slightly further to 0.97°C in *fut3*. The decadal increases in the periods derived from linear trend estimations amount to 0.32 K in *fut1*, to 0.47 K in *fut2* and to 0.55 K in *fut3*. The increase in *fut1* is comparable to the increase derived from observational data (see Subsection 1.2.2). All trends are highly significant with p-values below 10^{-5} .

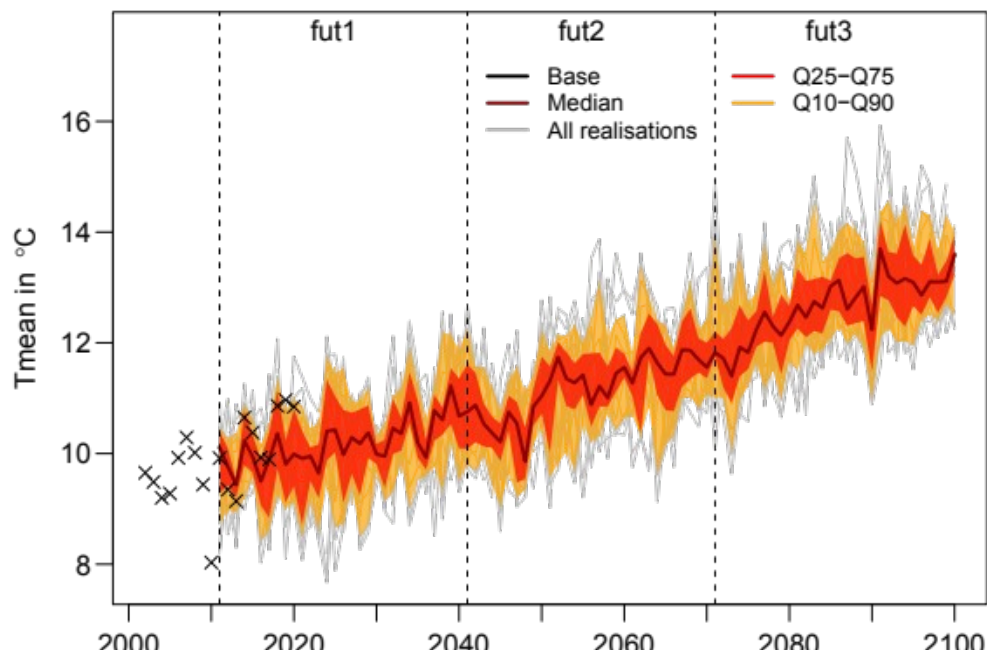


Figure 1.17: Timeseries of the mean annual temperature in the modelled realisations. The dark red line is the median annual mean temperature over the realisations. The red area is the interquartile range and the orange area the centre 80% of the annual mean temperature. Black crosses are the annual mean temperature in the base run.

Figure 1.18 shows the annual cycle of the observed data from the *base* run and the realisations in the *fut*-periods. It appears the median line of the *fut1* runs is close to the observed cycle. Especially in summer, both median lines only differ by 0.01 K. The median winter temperature is however already 0.51 K warmer in *fut1*. Towards the end of the century the scenario temperatures are increasing in all seasons. Warming is most pronounced in winter; the median differences between the observed annual cycle and *fut3* amount to 3.2 K in winter, 2.2 K in spring, 2.5 K in summer and 2.8 K in autumn. In *fut3*, the observed median falls generally below the interquartile range of the realisations.

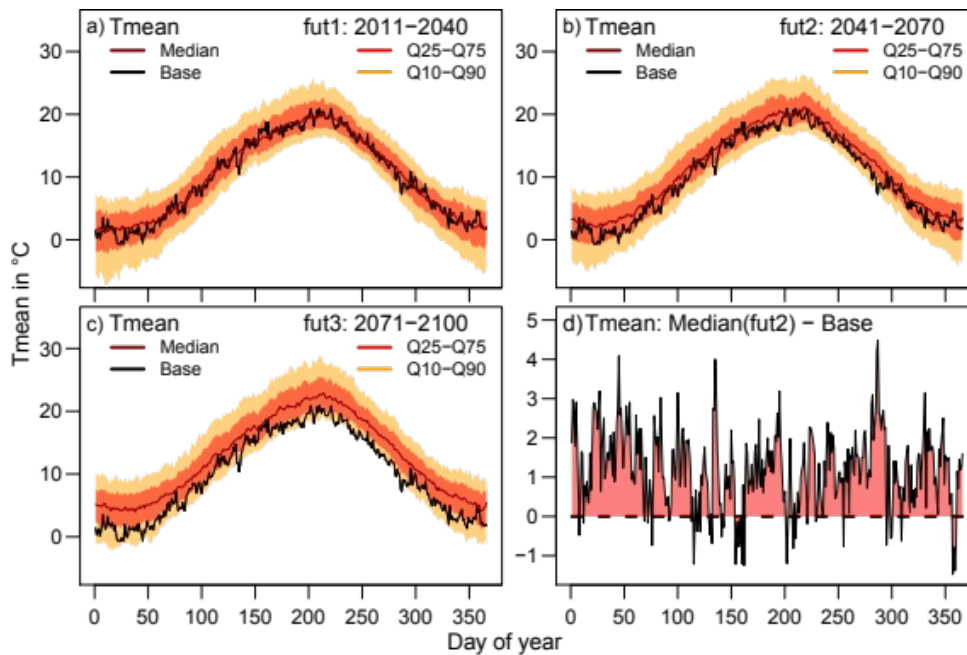


Figure 1.18: a-c) Annual cycles of mean temperature in the *fut* periods. The black line is the mean annual cycle in the *base* period. The dark red line is the median annual cycle of the realisations, and the red and orange bands show the inter-quartile and inner 80% ranges. d) Differences between the median *fut2* cycle and the median *base* run cycle.

1.6.3 Discharge

As for the *base* and the sensitivity runs, discharge was modelled for the Havelberg-Stadt gauge based on the climate scenario realisations. The annual timeseries of mean annual discharge is shown in Figure 1.19. The trend shows an increase over the scenario period. The average median in *fut1* amounts to $88.8 \text{ m}^3 \text{ s}^{-1}$ and increases to $94.9 \text{ m}^3 \text{ s}^{-1}$ in *fut2* and to $104.2 \text{ m}^3 \text{ s}^{-1}$ in *fut3*. The increase derived from the linear trend estimation amounts to about $2.5 \text{ m}^3 \text{ s}^{-1}$ per decade and is highly significant with a p-value below 10^{-5} . The standard deviation of annual median discharge is increasing from $24.7 \text{ m}^3 \text{ s}^{-1}$ to $26.5 \text{ m}^3 \text{ s}^{-1}$ between *fut1* and *fut2* and to $29.8 \text{ m}^3 \text{ s}^{-1}$ in *fut3*.

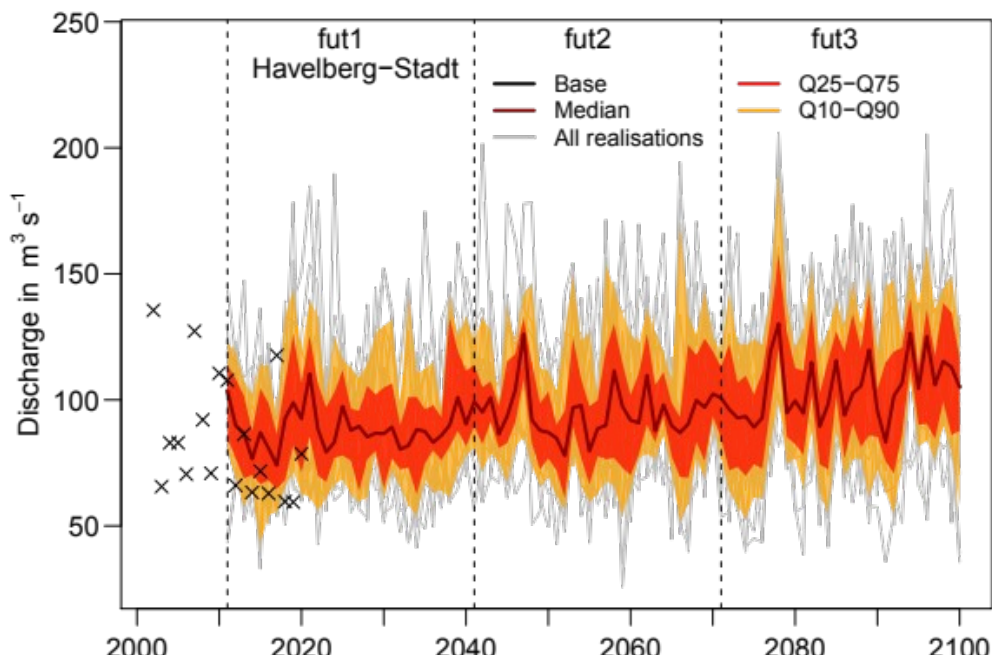


Figure 1.19: Timeseries of the annual mean discharge at Havelberg-Stadt gauge in the modelled realisations. The dark red line is the median annual mean discharge over the realisations. The red area is the interquartile range and the orange area the centre 80% of the annual mean discharge. Black crosses are the annual mean discharge in the base run.

The changes in climate input also influence the seasonality of discharges at Havelberg-Stadt. Figure 1.20a shows the seasonal distribution of the annual daily discharge in the *base* scenario; directly shown are the hydrographs of 2002 and 2019, the most extreme discharge years.

Figure 1.20b shows the same for the *Hc* realisation, selected for its median overall discharge. The period 2056–2074 was chosen by finding the least deviation in variance comparing a consecutive 19-year period to the discharges in the *base* run. Again, the 19 annual cycles are plotted in quantile ranges with the minimum and maximum annual cycles in grey found for 2058 and 2066.

Figure 1.20c considers all realisation's annual cycles between 2056 and 2074. The annual cycle with the maximum annual discharge appeared in the *Hd* realisation and the minimum in the *Ek2* realisation.

Due to the inclusion of all realisations the curves in Fig. 1.20c are smoother than in the other panels including only 19 annual cycles. Furthermore, the maximum and minimum annual discharges are more pronounced with a larger difference towards the Q10–Q90 quantile range.

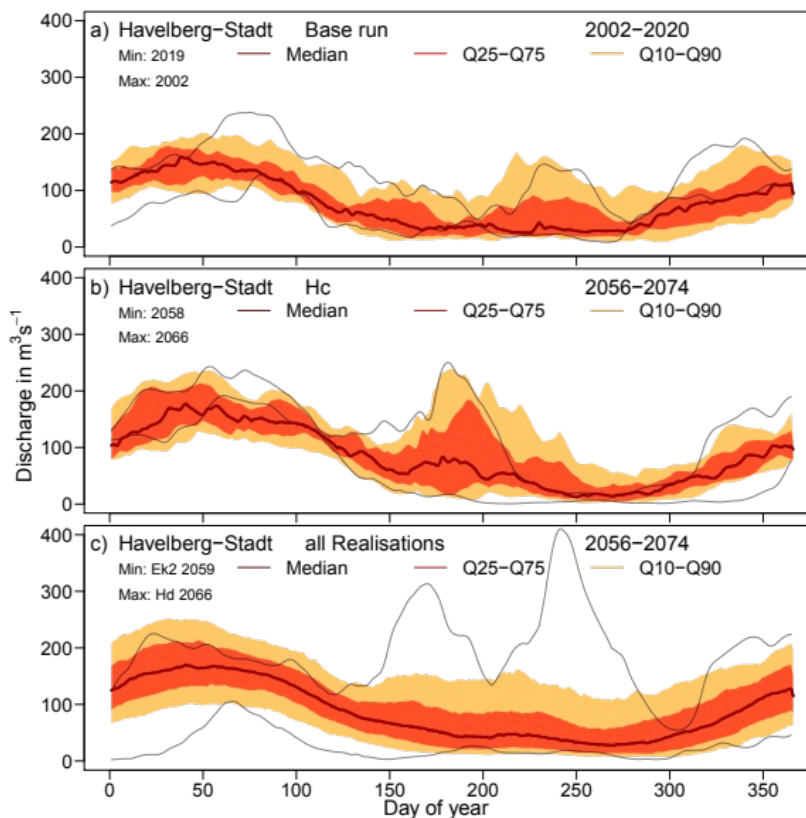


Figure 1.20: Distributions of simulated seasonal discharge cycles at Havelberg-Stadt (median and inner percentiles). Grey lines symbolize the hydrographs of the minimum and maximum discharge years. a) *base run*, b) *Hc* realisation between 2056 and 2074, and c) all realisations during the 2056–2074 period.

Using all realisations, the projected development of discharges is shown in Figure 1.21. The plot includes the daily discharges over a year in the time slices in quantile ranges. Furthermore, the median discharge hydrograph of the *base run* is included for comparison. Differences between the median daily discharge in the *base run* and in *fut2* are illustrated in the bottom-right plot (Fig. 1.21d).

Discharge increases are not equally distributed over the year. While in the first six months the mean of the median hydrographs increases by $7.7 \text{ m}^3 \text{ s}^{-1}$ and $21.1 \text{ m}^3 \text{ s}^{-1}$ from *fut1* to *fut2* and *fut3*, respectively, the respective increases are only $4.4 \text{ m}^3 \text{ s}^{-1}$ and $6.0 \text{ m}^3 \text{ s}^{-1}$ in the second half of the year. The relative increase in *fut2* is however slightly higher in the year's second half than in the first half (8.7% vs 6.9%). Comparing *fut3* and *fut1*, the relative increase in the first half of the year (18.9%) is much higher than in the second half (11.8%).

With the increase of median discharges also variability in discharges increases. The interquartile ranges between Q25 and Q75 widen from a daily average of $58.4 \text{ m}^3 \text{ s}^{-1}$ in *fut1* over $62.9 \text{ m}^3 \text{ s}^{-1}$ in *fut2* to $68.2 \text{ m}^3 \text{ s}^{-1}$ in *fut3*. The average ranges between Q10 and Q90 increases likewise from $113.4 \text{ m}^3 \text{ s}^{-1}$ in *fut1* over $124.1 \text{ m}^3 \text{ s}^{-1}$ in *fut2* to $132.3 \text{ m}^3 \text{ s}^{-1}$ in *fut3*.

Compared to the median of the daily discharges in the *base* period, the median lines of *fut2* and *fut3* are increased mostly in the first half of the year (see also Figure 1.21d regarding *fut2*).

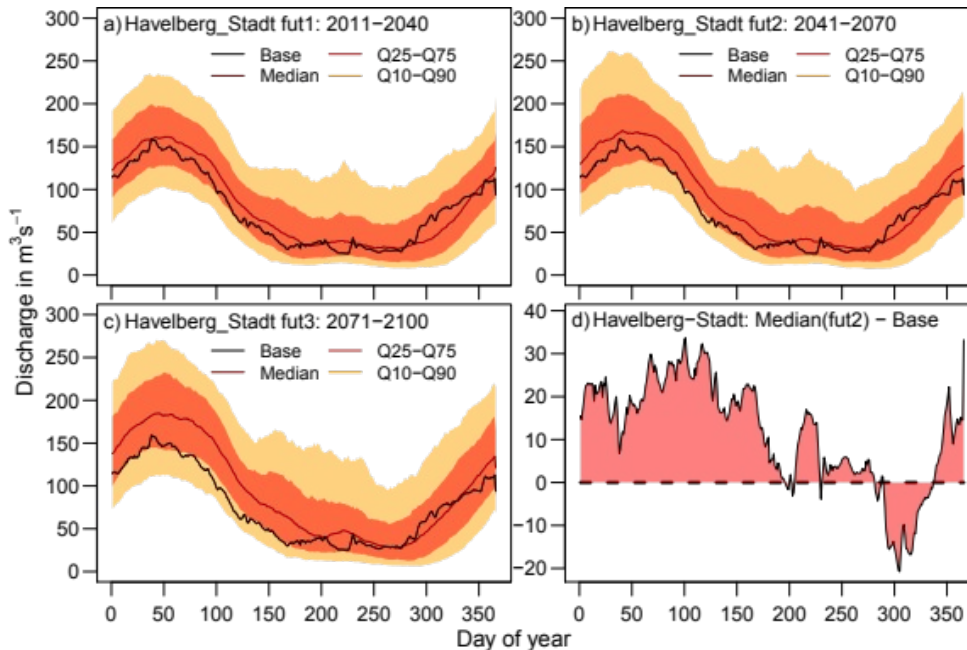


Figure 1.21: a-c) Simulated annual discharge cycles at Havelberg-Stadt. The black line is the median of the *base* period's daily discharges, the dark red line is the median of the realisations in the corresponding *fut* period and the orange and the red corridors are the bounds of the Q25–Q75 and Q10–Q90 percentile intervals. d) Difference of the median annual cycle of *fut2* and the *base* run.

Figure 1.22 shows the evolution of seasonal discharges along the time axis. The clearest upward trend is observed in spring with the highest gradient ($3.47 \text{ m}^3 \text{ s}^{-1}$) and the highest significance ($p < 10^{-5}$) in the linear regression. The winter season experiences the second highest increase, and there is no significant trend in autumn.

Regarding summer and autumn discharges, the deviations from the median line to both the upper bounds of the Q25–Q75 and the Q10–Q90 intervals are larger than to the lower bounds (Figs 1.21 and 1.22). The skewed distribution is caused by isolated flash floods from heavy precipitation events interspersing the generally drier seasonal conditions.

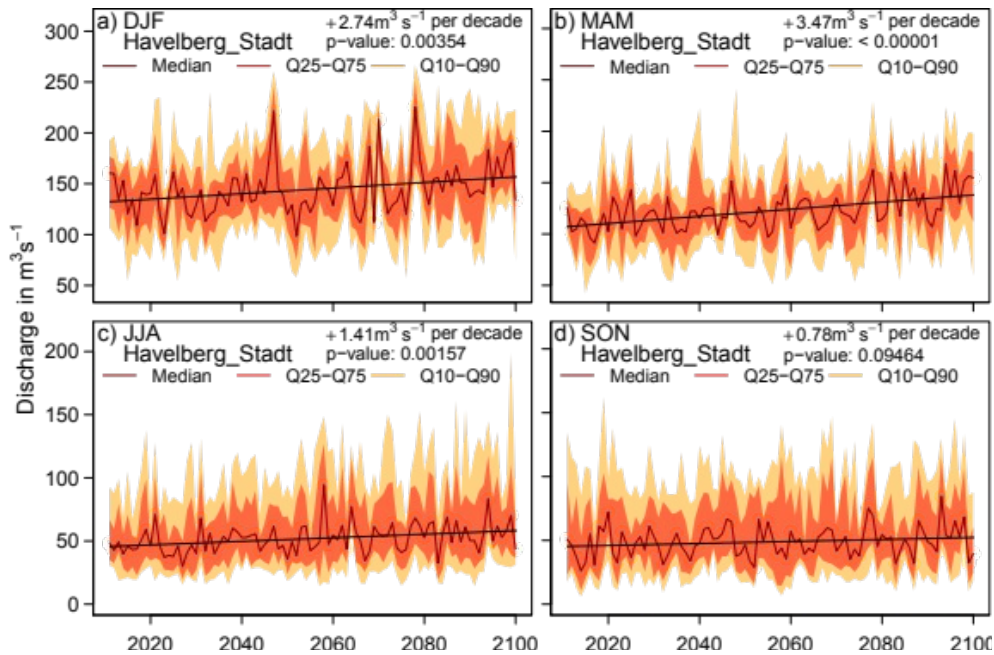


Figure 1.22: Evolution of seasonal discharges at Havelberg-Stadt. The dark red line is the annual median value of the realisations' average discharges within the season indicated in the upper left corner of the respective panel. Red and orange polygons show the extent of the interquartile and Q10–Q90 ranges. The black line is the linear trendline of the median values, the trend estimation is given in the upper right corner of the respective panel.

1.6.4 Evapotranspiration

The annual sums of ETp presented in Fig. 1.23 show an upward trend especially around the center of the scenario period. For the full period, the gradient derived from linear trend estimation amounts to 4.6 mm per decade and is highly significant ($p < 10^{-5}$). The averages of the ETp medians in the *fut* periods amount to 493.2 mm in *fut1*, 501.8 mm in *fut2* and 521.7 mm in *fut3*. The mean value in the *base* run amounts to 478.4 mm which is significantly lower than the *fut1* median value. As can be seen in the figure, also the ranges of the inter-quartile and Q10–Q90 intervals are increasing over time. The standard deviations of the annual ETp values of all realizations rise from 31.2 mm in *fut1* over 36.0 mm in *fut2* to 37.9 mm in *fut3*.

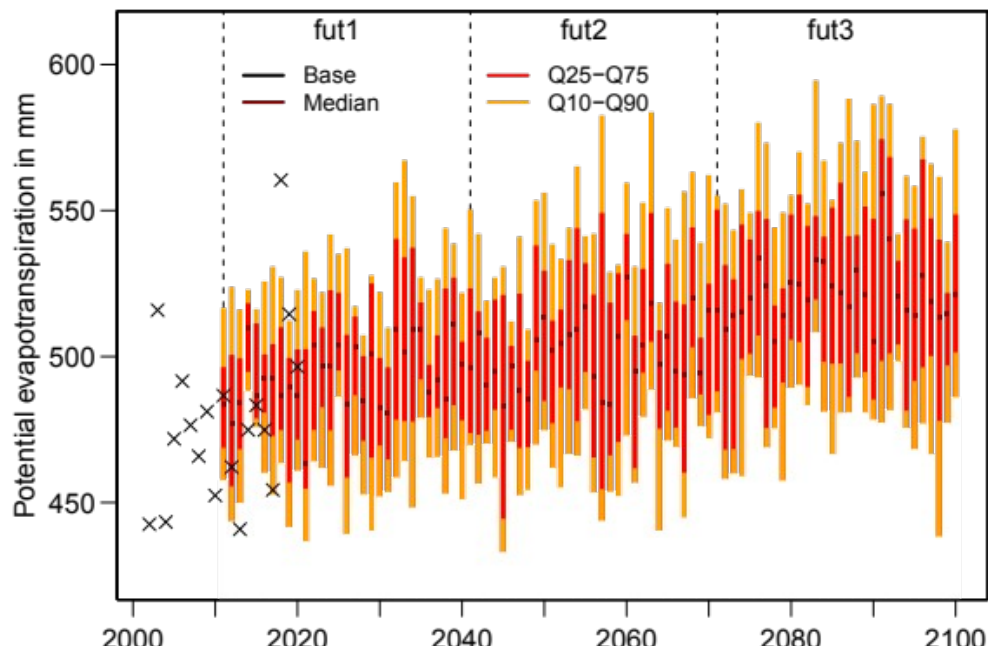


Figure 1.23: Timeseries of the annual PET sums in the realisations. The dark red points are the median annual PET sum over the realisations. The red bars are the interquartile range and the orange bars the centre 80% of the annual PET sums.

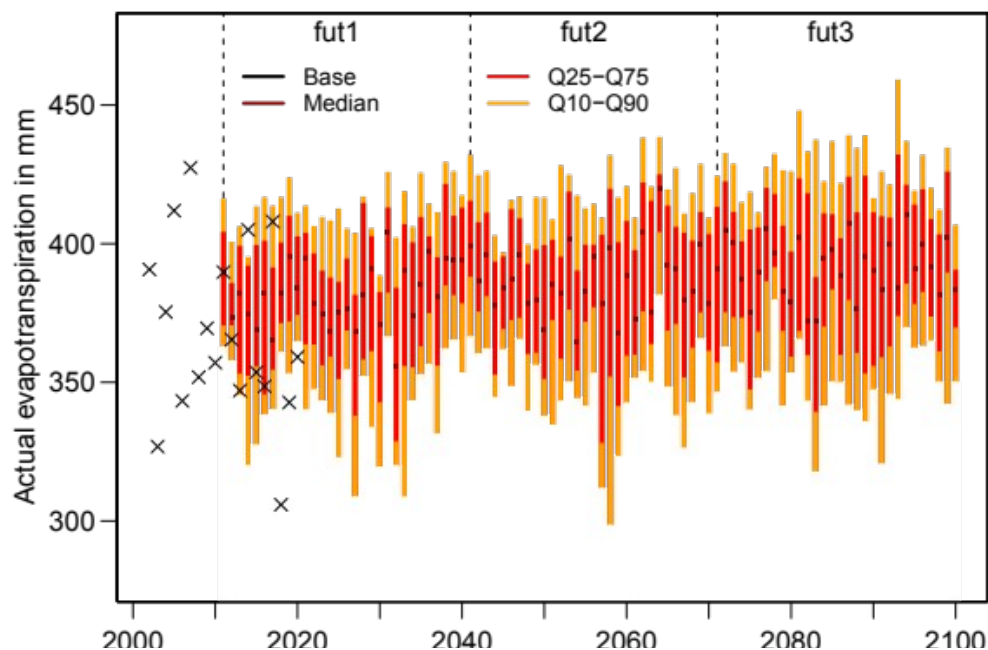


Figure 1.24 Timeseries of the annual AET sums in the realisations. The dark red points are the median annual AET sum over the realisations. The red bars are the interquartile range and the orange bars the centre 80% of the annual AET sums.

Annual ETa rates are presented in Fig. 1.24. Only a slight increase in ETa is visible over time. The average median values amount to 382.2 mm, 386.7 mm and 391.3 mm in *fut1*, *fut2* and *fut3*, respectively. The decadal increase derived from linear trend estimation amounts to 1.6 mm ($p \approx 0.0007$); approximately 3 mm per decade less than for ETp. The Q10–Q90 interval increases by 10.2 mm from *fut1* to *fut3*. In the years covered both by the scenario period and the *base run*, four out of ten annual ETa rates fall out of the inner 80% of the scenario runs.

Seasonal trends for ETa and ETp are shown in Fig. 1.25. The winter season is not considered due to the negligible evapotranspiration in this season.

The trends for ETa are positive but very weak in all seasons, in summer and autumn at the brink of statistical significance (Fig. 1.25a). The increase per decade is highest in summer (0.9 mm), followed by spring and autumn. The summer median evapotranspiration fluctuates between 160 mm and 220 mm which is of similar magnitude as in the *base run*.

For ETp the trends are much stronger, especially in summer and in autumn, whereas in spring the linear trend for ETa is weaker but somewhat more significant. Regarding the linear trends for the full scenario period, spring ETa follows the ETp increase to about two thirds, summer ETa changes only by one third of the ETp increase, and autumn ETa reacts only by about 20%.

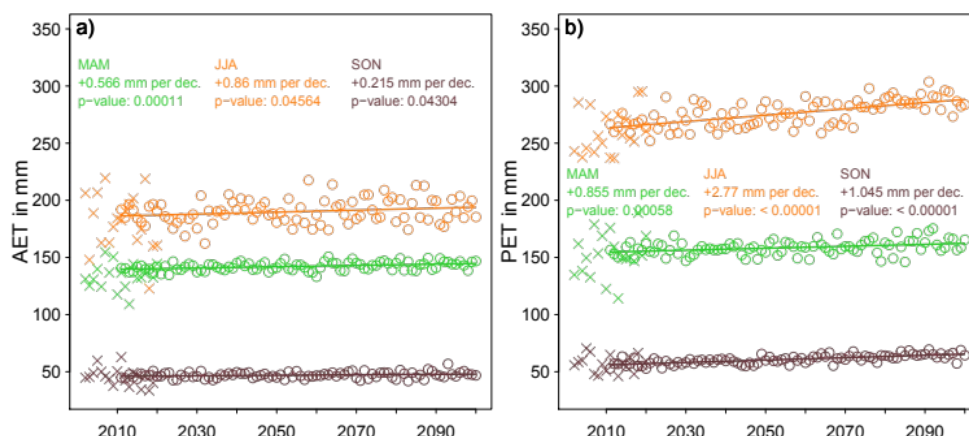


Figure 1.25: Trends of seasonal a) ETa and b) ETp in the scenario period. Each circle represents a median of the 21 annual averages of the seasonal values, crosses are the respective means of the base run. The straight lines are the linear trends, see the corresponding numerical values within the panels.

The spatial distribution of ETa is presented in Fig. 1.26. In *fut1*, AET is most pronounced in wetlands. Low values in the centre-east part correspond to the city-state Berlin with a high fraction of sealed land and accordingly low AET rates. The highest increases in *fut3* correspond with areas which already experienced high AET rates in *fut1*. Regarding only arable soils, AET decreased from a mean annual value of 302 mm in *fut1* to 296 mm in *fut3*. On forestland AET increased about 13 mm from *fut1* to *fut3*.

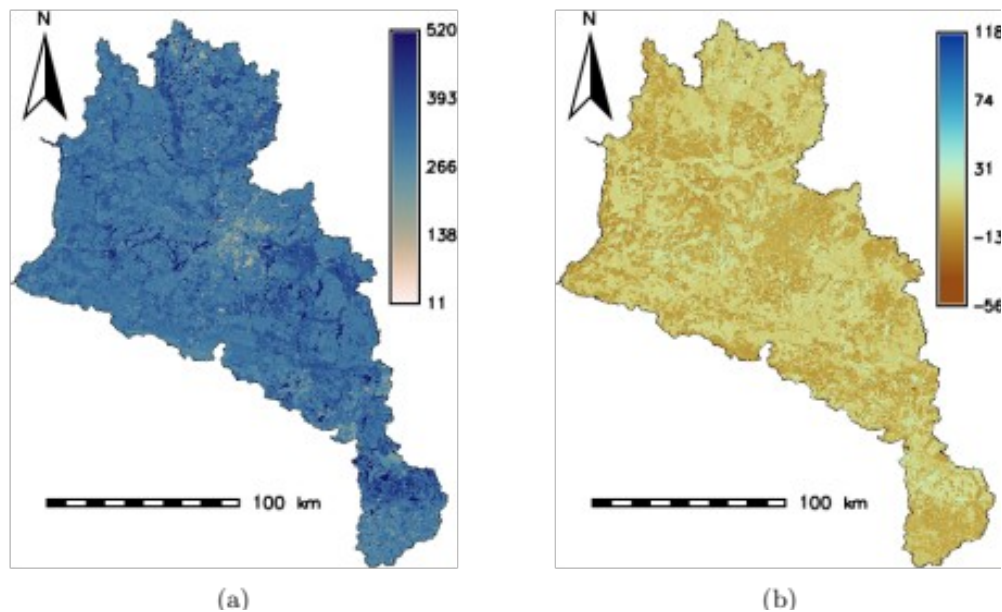


Figure 1.26: Spatial distribution of AET a) in fut1 and b) as difference of fut3 and fut1.

1.6.5 Groundwater recharge

The development of groundwater recharge (GWRCH) in the scenario period is shown in Fig. 1.27. The decadal increase in median value amounts to 5.3 mm and is highly significant ($p < 10^{-5}$). The average median annual GWRCH rates are rising from 240.6 mm over 256.2 mm to 273.2 mm in the three *fut* periods. The mean annual GWRCH sum of 225.7 mm in the *base* run is about 10% below the *fut1* value. The variability is increasing substantially between *fut1* and *fut3* (IQR: +22.5 mm; Q10–Q90: +20.8 mm); there is however not much change between *fut1* and *fut2* (IQR: +1.4 mm; Q10–Q90: +2.2 mm).

The changed climate conditions during the realisations result in different behaviour of the groundwater recharge process. The development over the scenario periods shows a split between the growing season and the dormant season (Fig. 1.28). In most of the growing season (March–October), the monthly groundwater recharge is below 10 mm. However, the tenth percentile in the plots indicates comparably high groundwater recharge rates in both summer and winter months. Overall, the increase in GWRCH is most amplified in the winter season. This is true for the differences of the median annual cycle of the realisations towards the base scenario and among the median realisations. Compared to the *base* run, winter GWRCH is increased by 10 mm, 16 mm, and 25 mm in *fut1*, *fut2*, and *fut3*, respectively. Most of the increase appears in December (Fig. 1.28d). The least increase is modelled in autums. In this season, the GWRCH is decreased by 1 mm in *fut1* and increased by 3 mm and 2 mm in *fut2* and *fut3*.

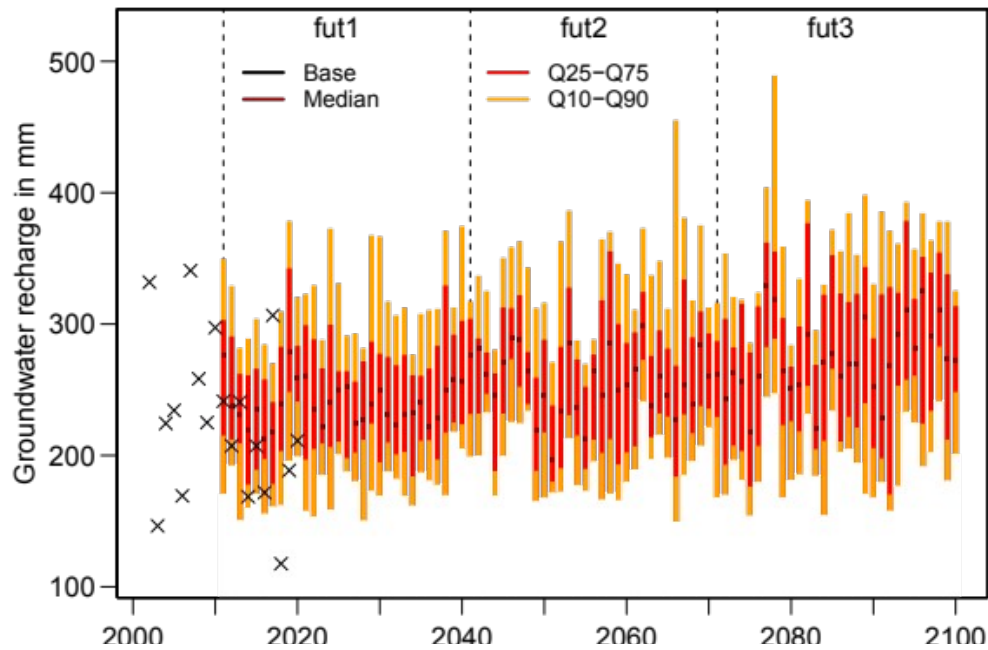


Figure 1.27: Timeseries of the annual GWRCH sums in the modelled realisations. The dark red dots are the median annual GWRCH sums over the realisations. The red bars show the interquartile ranges and the orange bars the inner 80% of the annual GWRCH sums. Black crosses are the annual GWRCH sums in the *base* run.

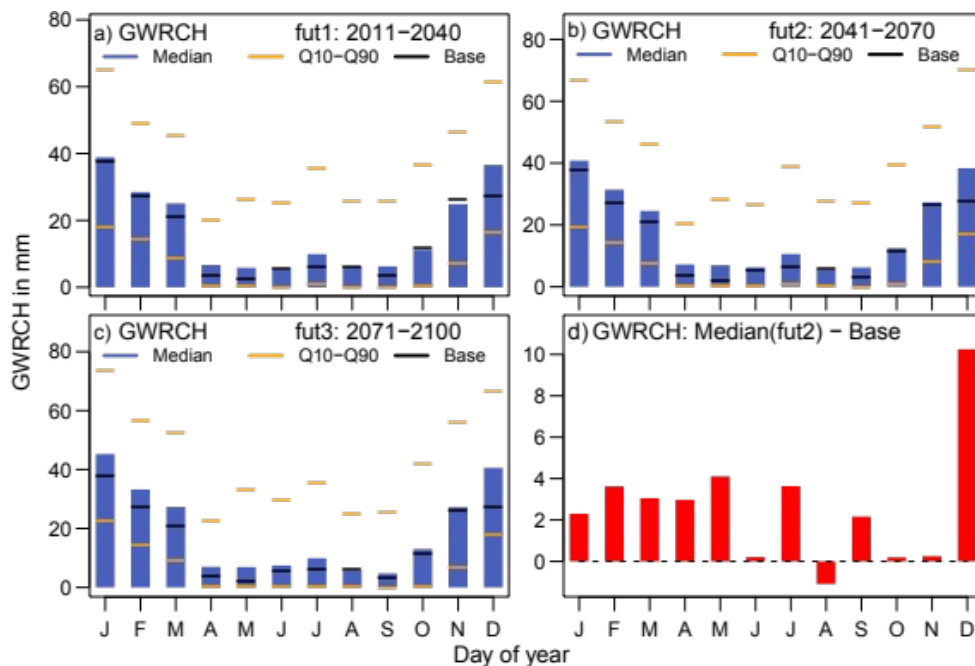


Figure 1.28: a)–c) Monthly GWRCH simulated in the *fut* periods. Blue bars are the arithmetic means of the medians of the respective monthly values. The lower orange line marks the 10th and the upper one the 90th percentile of the realisations. The black lines are the median values of the base run. d) Difference between the *fut2* medians and the monthly GWRCH medians of the *base* run.

The seasonal trends for winter and spring groundwater recharge (Fig. 1.29a) are significant and positive. The trend for winter amounts to about +3.0 mm per decade and for spring to +0.8 mm per decade, increasing the annual groundwater recharge about +26.9 mm and +7.4 mm at the end of the century. The *base run*'s means are slightly more fluctuating but fall well in the range of the medians during the first years of the scenario period.

Linear trends for summer and autumn are increasing as well, however these are non-significant tendencies with *p*-values exceeding 0.08 and 0.10, respectively. The drought years 2003 and 2018 are visible in the observed data (Fig. 1.29b). The medians of the seasonal realisations are not reaching to those values.

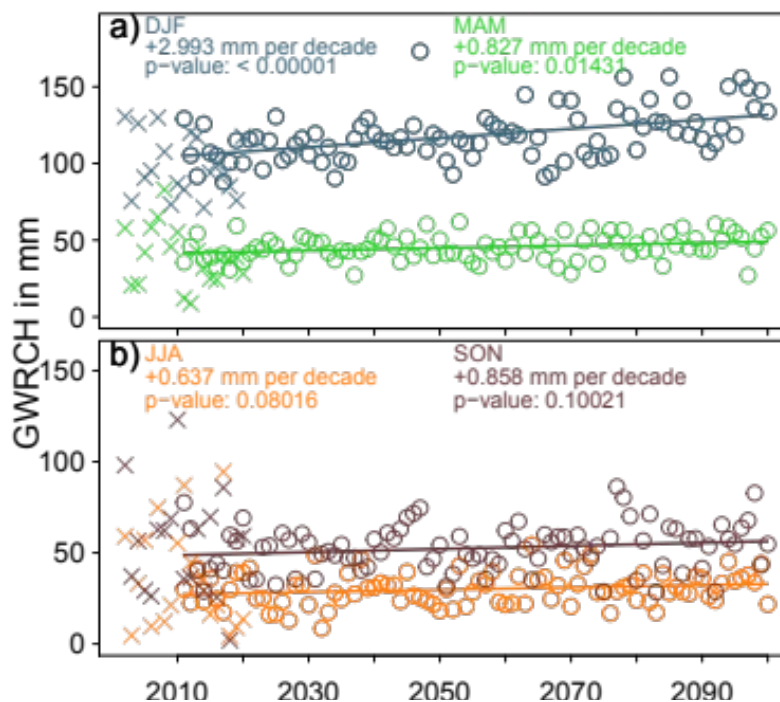


Figure 1.29: Simulated GWRCH trends for a) winter and spring and b) summer and autumn in the scenario period. Circles represent the annual median of the 21 seasonal GWRCH realizations, crosses show the arithmetic means of the base run. The straight lines are the linear trend estimations of the scenario (numerical values given above).

The spatial distribution of groundwater recharge (GWRCH) is presented in Fig. 1.30. There are distinct differences between areas contributing more than 500 mm per year and areas with almost no GWRCH at all. Among the areas without GWRCH are open water bodies by definition, they can be assumed to represent “uncovered aquifers” with high evaporation losses. Berlin is visible as low GWRCH blob near the centre of the Havel area; its many sealed surfaces hamper infiltration. On average, GWRCH is projected to increase by about 30 mm per year between *fut1* and *fut3*; on agricultural and forested land the increase is slightly higher (33 mm).

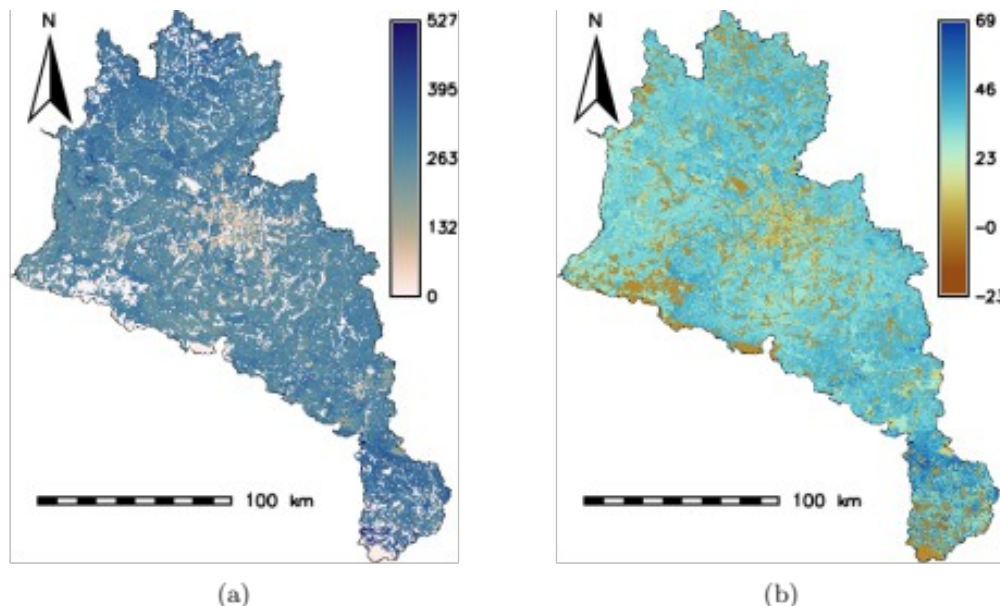


Figure 1.30: Spatial distribution of a) groundwater recharge in *fut1* and b) its projected change as difference of *fut3* and *fut1*

1.6.6 Low flows

In the following, the scenario realisations are investigated for low flow characteristics. Figure 1.31 shows the arithmetic means of the amount of days per year below the Q20 and Q5 discharges of the scenario. The overall averages are $0.20 \cdot 365.25 = 73.1$ and $0.05 \cdot 365.25 = 18.3$ days. In *fut1* there are on average 78.8 days per year below Q20. This reduces to 69.6 days per year in *fut3*, a linear decrease of 1.5 days per decade ($p = 0.013$).

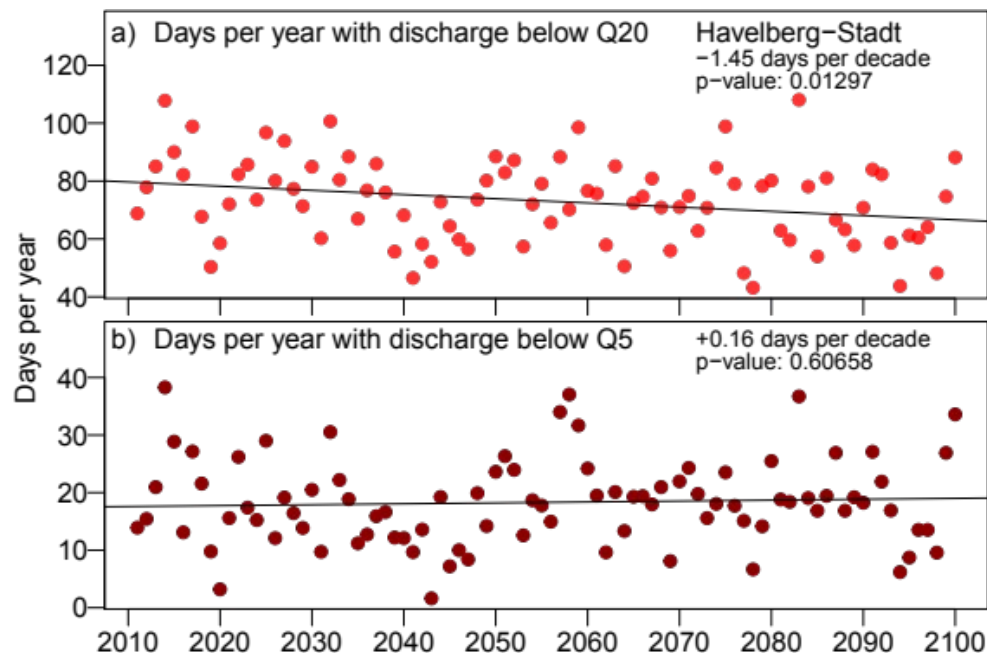


Figure 1.31: Annual average number of days with discharge simulated below Q20 and Q5 of the entire scenario discharge at Havelberg-Stadt.

The trend in simulated daily discharges falling below Q5 is not significant ($p = 0.61$). The values for *fut1* and *fut2* are about the same level with 18.0 days, and there are 19.0 days in *fut3*. However, the amount of days per year with very low flow is not decreasing as expected from the Q20 results and the projected increase in discharge.

Since there can be more than one consecutive low flow event in a year, Fig. 1.32 shows the maximum length of single events not exceeding the individual twentieth and fifth percentile in the three scenario periods (CD20Q and CD5Q). Regarding CD20Q, the realisations show a trend towards shorter lasting low flow events from the recent to the most future period. In CD5Q the trend is not so clear with the median values at levels about 75 days.

Besides the duration of low flow events, the actual amount of discharge during such events is an important characteristic. Therefore, Fig. 1.33 shows the distributions of the minimum 30 days (NM30Q) and 7 days (NM7Q) discharges. The lowest discharges in both timespans shows a decreasing trend over time. The lowest median value is found for *fut1* in both metrics with an average discharge of about $2 \text{ m}^3 \text{ s}^{-1}$ on a 30-day span and about $1 \text{ m}^3 \text{ s}^{-1}$ on a 7-day interval. The following periods experience less extreme low flow events.

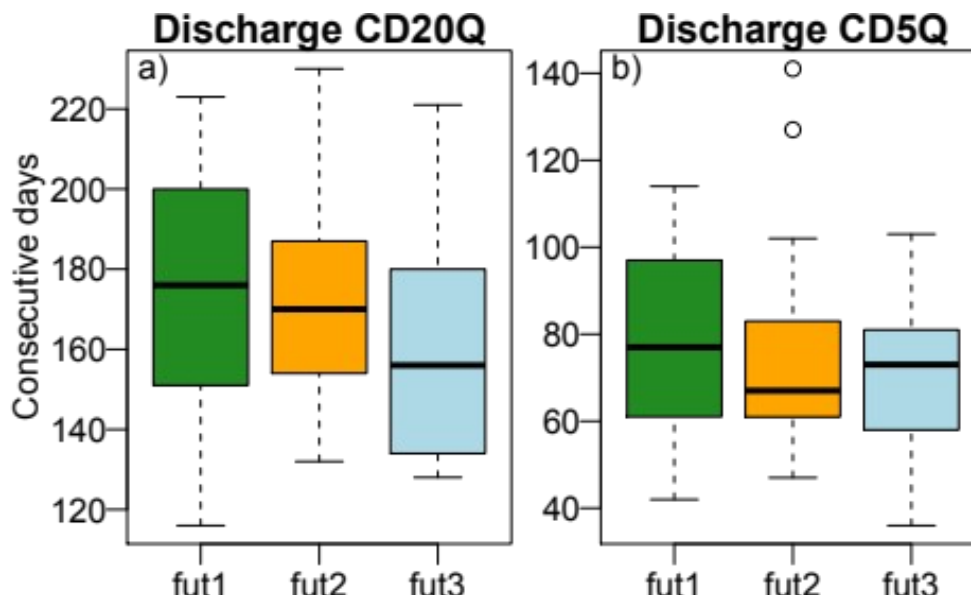


Figure 1.32: Simulated maximum consecutive days below the individual a) twentieth and b) fifth percentile of daily discharge at Havelberg-Stadt in the scenario periods. Dashed lines are the period's median values of the realisations.

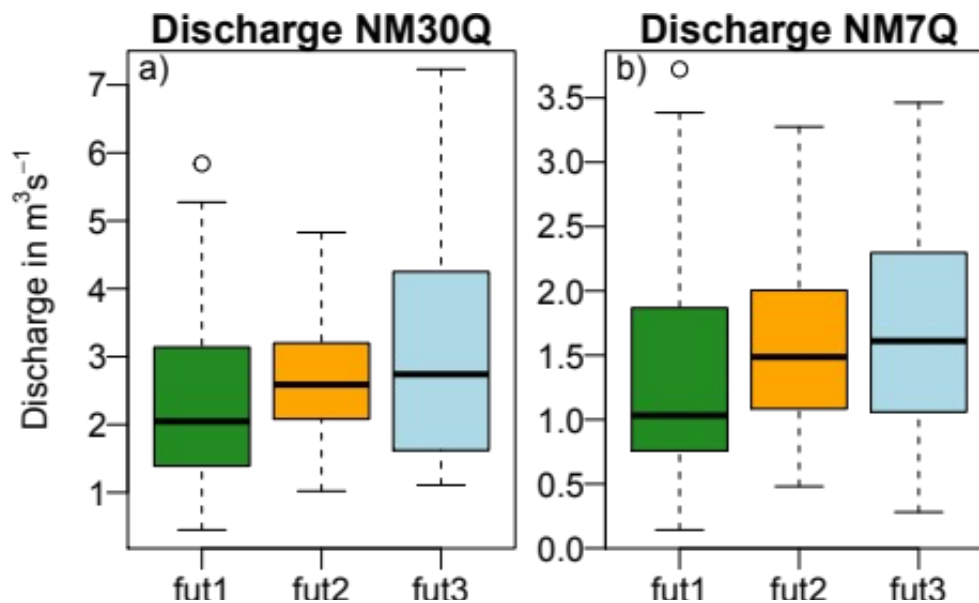


Figure 1.33: Distributions of the average discharge in the consecutive a) 30 days and b) 7 days low flow events simulated at Havelberg-Stadt.

1.6.7 Soil Drought

Figure 1.34 shows the development of the soil water index SWIND in the scenario period. Annual median SWIND values experience a tiny decrease over time. The average median SWIND in *fut1* amounts to 0.872, followed by 0.871 in *fut2*, and 0.864 in *fut3*. The decadal decrease derived from linear trend estimation amounts to -0.0012 and is nevertheless significant at $p = 0.006$. This trend is more pronounced in autumn (-0.0029 at $p = 0.002$).

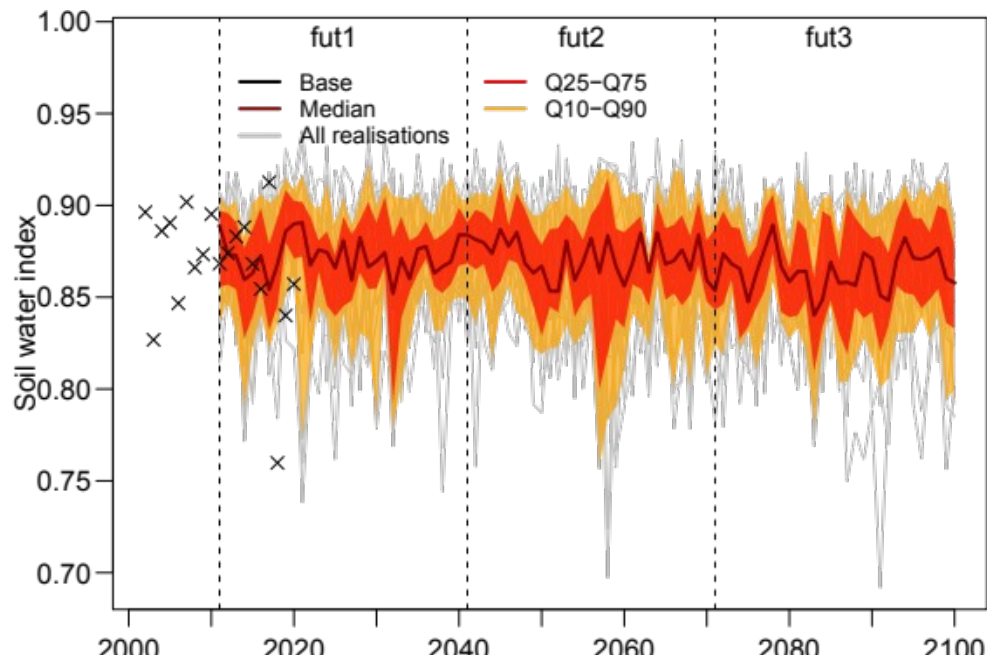


Figure 1.34: Timeseries of the annual SWIND averages in the simulated realisations. The dark red line indicates the medians of the annual averages. The red area shows the interquartile range, and the orange area the inner 80% of the annual SWIND distributions. Black crosses symbolize the annual mean SWIND in the *base* run.

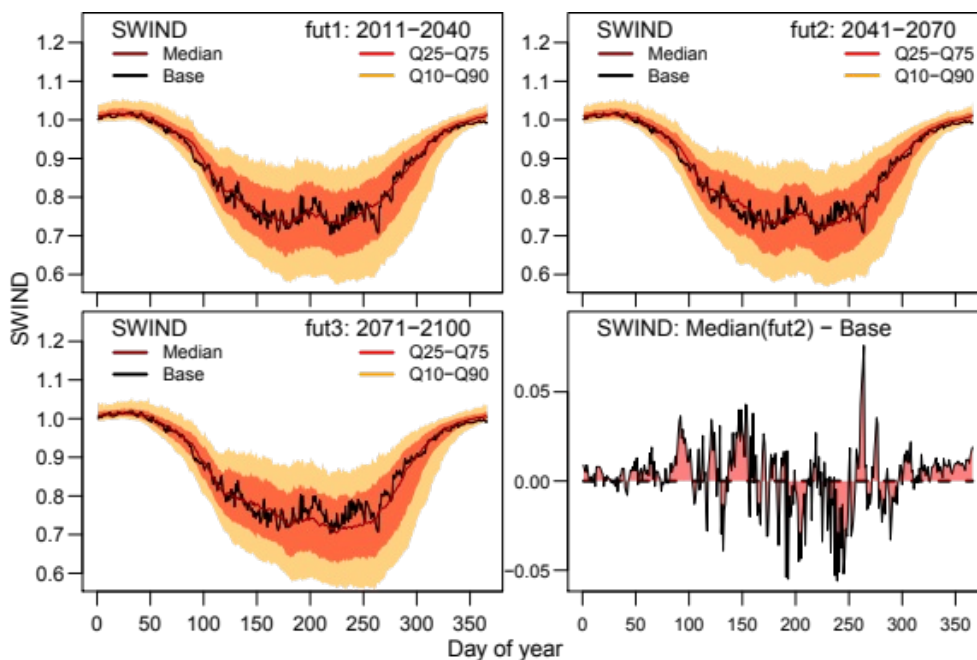


Figure 1.35: a)–c) Annual cycles of soil water index (SWIND) in the three *fut* periods. d) Daily median SWIND differences between *fut2* and *base*.

There are several scenario values comparable to drought year 2018 with the lowest annual SWIND in the *base* run (cf. Fig. 1.34). Especially the extreme low values between 2087 and 2091 are worth mentioning since they are all from the Hc realisation with an average of 0.75 in five consecutive years. The trend towards drier soils at the end of the century obviously concentrates at the beginning of autumn (*fut3* in Fig. 1.35c).

As for low flow we examine the soil drought trajectories throughout the realizations. Figure 1.36 shows the arithmetic means of the days that SWIND is falling below the run-specific twentieth and fifth percentiles of the scenario simulation. There is a significant increase in the number of days per year that SWIND falls below the twentieth percentile. The increase amounts to 1.15 days per decade. In *fut1* the average value is 39.8 days while in *fut3* it amounts to 46.6 days. The linear increase for days per year below the fifth percentile of SWIND is not significant. The time slice averages are 9.9 days in *fut1*, 10.5 days in *fut2*, and 11.4 days in *fut3*.

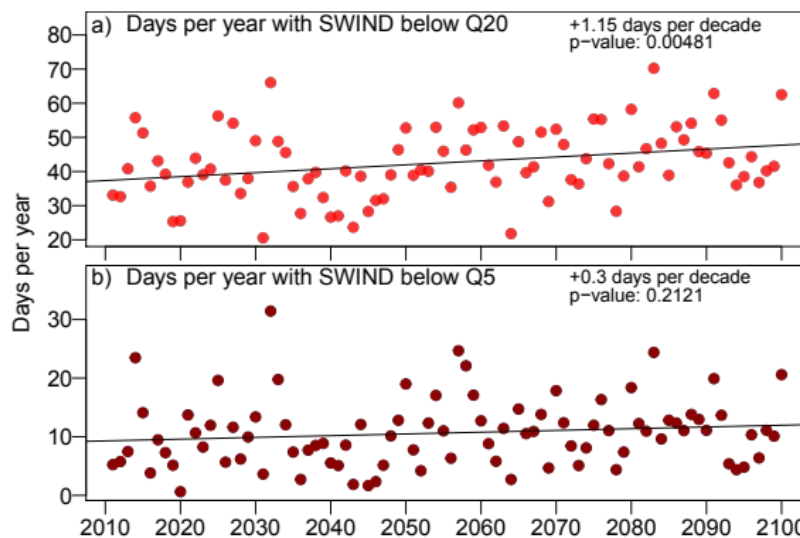


Figure 1.36: Annual arithmetic means of the durations of dry soil conditions simulated below the a) twentieth and b) fifth percentile of the SWIND distribution over all realizations.

The distributions of durations of the maximum-length consecutive states below the 20th and 5th percentile thresholds (CD20SWIND and CD5SWIND) is shown in Fig. 1.37. From the median values, there is no clear trend in this metric over the periods. Regarding the CD20SWIND metric, the distribution of the length of soil drought events is similarly distributed. The three extreme values (>125 days) in *fut2* are however not reached in the other periods. For the other realisations the maximum duration below the 20th percentile of SWIND is in a small corridor ranging between about 50 and 90 days. There tend to be longer lasting extreme soil drought events in *fut1* compared to the other periods.

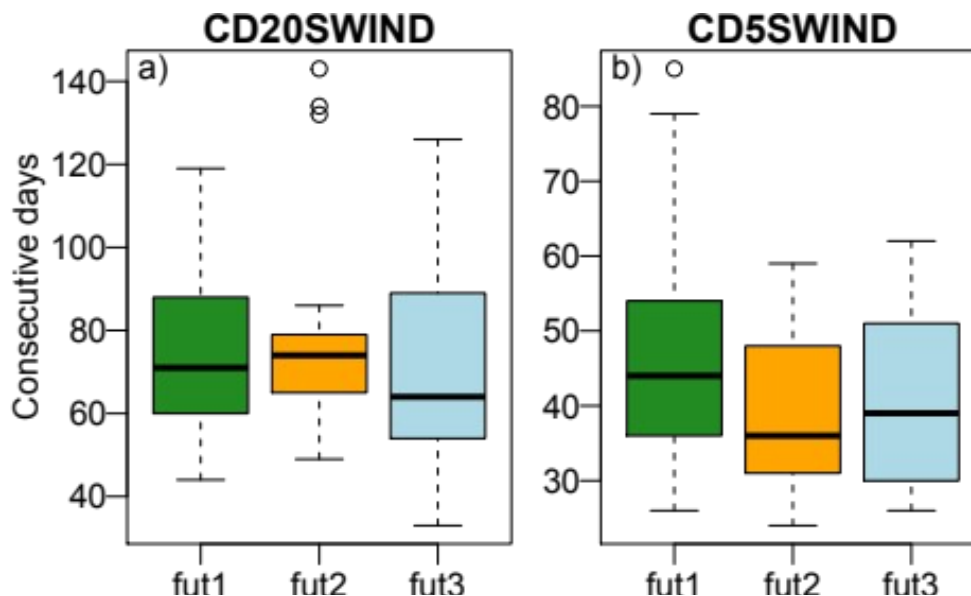


Figure 1.37: Distributions of the maximum durations of consecutive days with dry soil conditions simulated below the realisation's twentieth (a) and fifth (b) percentiles of SWIND.

1.6.8 Crop yields

As shown in the sensitivity study (Section 1.5) trends for crop yields are also differing in their reaction to changing climatic conditions during the realisations (Fig. 1.38). Silage maize (SLMA) yields are not changing much in the realisations. Median annual SLMA yields are slightly increasing from 291 dt ha⁻¹ in *fut1* over 297 dt ha⁻¹ in *fut2* to 298 dt ha⁻¹ in *fut3*. Yields of winter rape (RAPE) decrease however significantly. Linear trend estimation suggests median RAPE yields to decrease by -2.3 dt ha⁻¹ per decade. Starting with a median yield of 40 dt ha⁻¹ in *fut1*, the median yield amounts to only 26 dt ha⁻¹ in *fut3*. The trend in winter wheat (WWHT) yields is similar to the one of RAPE with the difference that high, median and low annual mean yields decrease by about the same gradient. The median annual WWHT yield is reduced by 21% from 77 dt ha⁻¹ in *fut1* to 61 dt ha⁻¹ in *fut3*. It should be noted that the *fut1* results for all crops are very close to the respective *base* yields. The latter however deviate a little from the observations (see Table 1.6 at the end of Section 1.4).

Different crops expose different reactions towards climatic influences. Correlations of the annual crop yields with the annual arithmetic means of temperature, precipitation and SWIND are presented in Table 1.8. The Pearson correlation coefficients are suggesting a negative influence of temperature increase for wheat and rape yields and a rather low influence of the soil water. This can be explained by lower optimal temperatures for RAPE and WWHT as well as with the difference in growing season compared to SLMA. Another reason might be the rather indifferent changes in soil moisture over the scenario period.

RAPE and WWHT benefit from high soil moisture in spring whereas maize strongly depends on rainfall in summer. For maize the coefficients suggest a small negative influence of temperature increase and high positive influences of precipitation and SWIND increase.

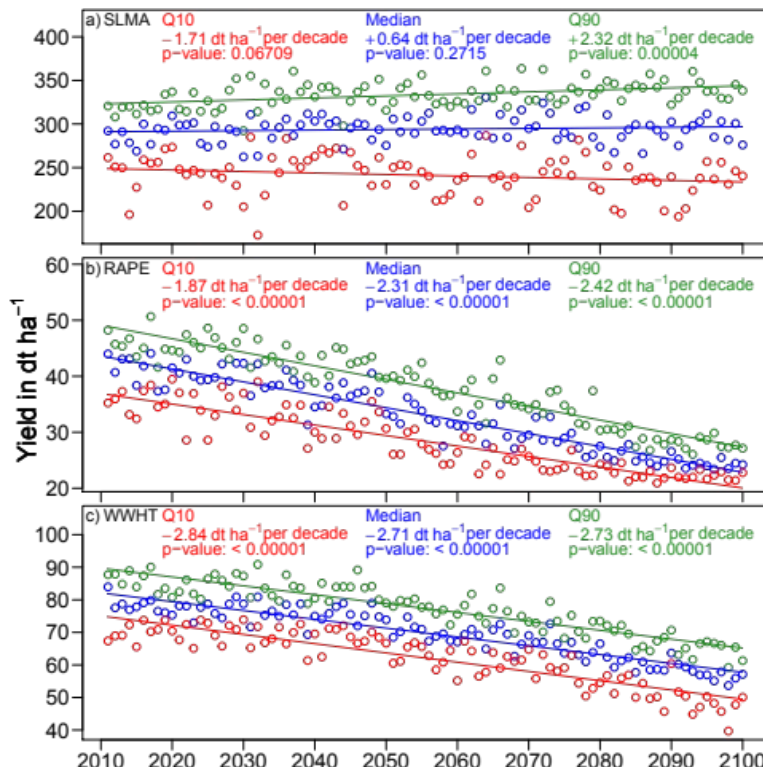


Figure 1.38: Trends for a) SLMA, b) RAPE and c) WWHT yields in the scenario period. Blue circles are the median annual average yields, red circles are the 10th percentile and green circles are the 90th percentile of annual average yields per year.

Table 1.8: Mean correlation between run specific annual means of temperature, precipitation and SWIND with yields of the three cultivated crops over the scenario period.

R-squared	WWHT	RAPE	SLMA
Temperature	-0.77	-0.80	-0.06
Precipitation	-0.15	-0.26	0.55
SWIND	0.13	0.05	0.64

1.7 Discussion and Conclusions

The results presented above include a sensitivity study and a projection based on 21 bias-adjusted RCP8.5 climate realisations. We have seen significant changes in the eco-hydrological system caused by climatic shifts, both from deliberate manipulation of the weather input and as contained in the climate scenario. As detailed in Section 1.5, small decreases in precipitation (minus 5–10%) directly caused drought states in soil and vegetation, increases in PET and radiation were also important factors. Temperature increases by 1–2 degrees had not much influence on the soil water dynamics; C3 crop yields were however reduced a lot.

Increased precipitation in the climate scenario largely reduces eventual drought conditions, as examined in Section 1.6. However, trends in the soil water index SWIND suggest a decrease in soil water, at least during summer and autumn. The increasing ET_p levels in the scenario realisations were not met by ET_a. This is due to limited water provision in the summer and autumn season; it might also be connected to the earlier summer dieoff in wheat and rape in the later (warmer) stage of the scenario period. A likewise extending gap between ET_p and ET_a under climate change had already been presented by Conradt et al. (2012) for the German Elbe river basin.

Against the trend in recent years with many low precipitation years since about 2011 (see Fig. 1.2b) and the extreme drought conditions in 2018, 2019, and 2022, the bias-adjusted CORDEX realisations used for the scenario period suggest increasing precipitation rates in the Havel area. This divergence between observations (drought intensification in recent years) and scenario studies (indifferent or even becoming slightly wetter) has been described by Piniewski et al. (2022) for Central Europe. Moreno-Chamarro et al. (2021) however do suggest an increase of winter precipitation in north-western Europe driven by a northward shift of the gulf stream resulting in enhanced cyclonic activity in the North Atlantic which should even not be considered in nowadays coarse GCMs with grid cell spacings of about 50–100 km.

The strong decreases in winter wheat and winter rape yields during the scenario period are due to their comparably low optimum temperatures (below 20°C) which in general make C3 plants more sensitive to temperature than to water stress (cf. Fig. 1.38 and Table 1.8). The strong heat effects on wheat and rapeseed in Eastern Germany have been recently investigated in an insurance context (Bucheli et al. 2022). For maize, a C4 plant, the higher temperature was beneficial and the growth was limited only slightly by water availability. In reality, water stress plays a much larger role for maize yields which should limit the growth by a larger extent. Generally, the yield effects of temperature and water stress are intertwined and not easily distinguishable (Deryng et al. 2014, Siebert and Ewert 2014, Lesk et al. 2022).

Multiple variables experience diverging trends over the scenario period. This and the differences between recent observations and actual modelling suggest that complex shifts involving droughts in the real-world eco-hydrological system are hard to predict well in advance.

2 Crop drought risk in Moldova under global warming and possible crop adaption strategies

by Sergio M. Vicente-Serrano, Carmelo Juez, Vera Potopová, Boris Boincean, Conor Murphy, Fernando Domínguez-Castro, Lars Eklundh, Dhais Peña-Angulo, Ivan Noguera, Hongxiao Jin, Tobias Conradt, Ricardo Garcia-Herrera, Jose Manuel Garrido, David Barriopedro, Jose Manuel Gutiérrez, Maialen Iturbide, Jorge Lorenzo-Lacruz, and Ahmed El Kenawy

This part of the Deliverable analyzes the relationship between drought processes and crop yields in Moldova together with the effects of possible future climate change on crops. The severity of drought is analyzed over time using the Standard Precipitation Index (SPI), the Standardized Precipitation Evapotranspiration Index (SPEI), and their relationship with crop yields. In addition, rainfall variability and its relationship with crop yields are examined using spectral analysis and squared wavelet coherence. Observed station data (1950–2020 and 1850–2020), ERA5 reanalysis data (1950–2020), and climate model simulations (period 1970–2100) are used for the climatic variables. Crop yield data (maize, sunflower, grape), data from experimental plots, and the Enhanced Vegetation Index (EVI) from MODIS (Moderate Resolution Imaging Spectroradiometer) satellites (period 2000–2020) were also used. Results show that although the severity of meteorological droughts has decreased in the last 170 years, the impact of precipitation deficits on different crop yields has increased in the last two decades, concurrent with a sharp increase in temperature, which negatively affected crop yields. Annual crops are now more vulnerable to natural rainfall variability, and in years characterized by rainfall deficits there is the possibility of reductions in crop yield increases due to sharp increases in temperature. Climate model projections reveal a pessimistic outlook in the absence of adaptation, highlighting the urgency of developing new agricultural management strategies.

2.1 Introduction

The sensitivity of food production to climate variability and change is a critical issue (Lobell and Field 2007; Peng et al. 2004; Schlenker and Roberts 2009), with several studies raising concern for crop yield failures in response to drought (Kim et al. 2019; Páscoa et al. 2020; Sah et al. 2020; Wang et al. 2016). Crop yields are commonly affected by soil water availability (Hlavinka et al. 2009; Potopová et al. 2020; Wang et al. 2016), which is ultimately determined by precipitation and evapotranspiration (Durre et al. 2000; Teuling et al. 2006), but also by the variability of other meteorological variables that affect photosynthesis (e.g. radiation, temperature) and plant physiology (vapour pressure deficit, VPD, and temperature: Fontana et al. 2015; Hernandez-Barrera et al. 2017; Lüttger and Feike 2018; Zampieri et al. 2017).

The influence of temperature on plant physiology is complex. On one hand, higher temperatures can promote more photosynthesis which may increase the biophysical capacity of crops and overall crop yields. On the other hand, temperature increase drives enhanced VPD, which regulates leaf stomatal closure and reduces photosynthesis and carbon uptake (Breshears et al. 2013; Grossiord et al. 2020). Moreover, higher temperature is also a driver of atmospheric evaporative demand, which increases plant water stress under low soil moisture, potentially triggering plant mortality under hydraulic failure (Anderegg et al. 2012; McDowell et al. 2013). Finally, under situations of extreme heat, leaf tissues are damaged with associated hydraulic consequences (Brodribb et al. 2020).

There is general consensus that, as consequence of these different mechanisms, temperature rise is accelerating damages associated with low water availability (Asseng et al. 2015; Lobell et al. 2015) and that projected future temperature increases will enhance negative impacts on crop yields (Lobell et al. 2006; Olesen et al. 2011; Tebaldi and Lobell 2008). Although fertilizing CO₂ effects could counteract negative effects of climate change of crops (Conley et al. 2001; De Kauwe et al. 2021; Peters et al. 2018), this is still a subject of an ongoing scientific debate with literature supporting a secondary role of this factor in comparison to the primary importance of soil moisture deficits, increased VPD and heat (Menezes-Silva et al. 2019; Morgan et al. 2004; Xu et al. 2016).

The identification of climate change impacts on crop yields is not an easy task as there are several technological and socioeconomic aspects that play a fundamental role in mitigating or amplifying the effects. Nevertheless, efficient management and identification of successful adaptation options require guidance on possible crop yield decreases or failures with climate change. This is particularly critical in world areas where agriculture plays an important role in the economy and society, especially in large regions of central and South America, Africa and Asia where agriculture is the main economic activity. There are also regions of Europe that are predominantly

agrarian and highly vulnerable to a decline in crop potential as a consequence of climate change.

In the Republic of Moldova, located in Eastern Europe, more than 80% of land is covered by non-irrigated crops (Figure 2.1) and agriculture employs more than 30% of the population. This region has been frequently affected by droughts (Potop 2011), with large negative consequences on crop yields (Potop 2011; Potopová et al. 2016). The 2020 drought was particularly serious with crop yields decreasing by 30% on average, causing a reduction of 20% in employment in the sector and a decline of 8% in Gross Domestic Product (World Bank 2021).

Given such vulnerability to droughts in Moldova, it is necessary to investigate the climate mechanisms that have caused this strong decline in crop yields in recent years. It is also necessary to assess possible future climate scenarios that may drive changes in crop yields to identify potential crop management strategies that might limit future declines in crop yields. In this study we analyse the evolution of crop yields in Moldova over the last 70 years and assess climate drivers and possible future drought scenarios.

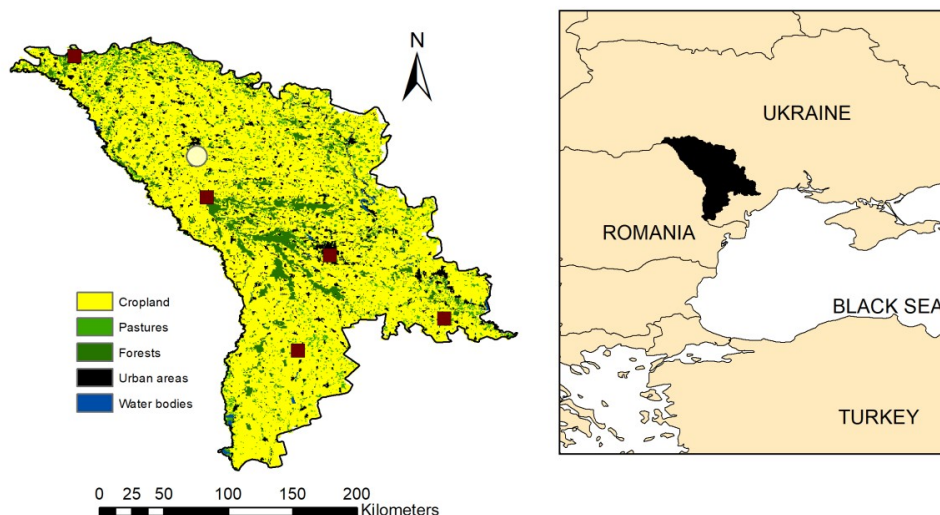


Figure 2.1: Land cover characteristics of Moldova. The locations of the meteorological stations used in this study are shown by squares. The white circle shows the location of the experimental fields of the Selectia crop field research institution.

2.2 Data and Methods

2.2.1 Data

We use data from five meteorological stations in Moldova (Figure 2.1) provided by the Moldovan meteorological service. The data contain monthly precipitation and maximum and minimum temperature with no gaps. Four station records contain data from 1950 to 2020 with the Chisinau station data containing precipitation data since 1850. The data were quality controlled and homogeneity tested using meteorological stations available from Ukraine and Romania through the Global Historical Climatology Network (Chen et al. 2002; Menne et al. 2012). Homogeneity testing was based on HOMER (Homogenization in R: Mestre et al. 2013), and no temporal inhomogeneities were found, so corrections to the raw data were not needed. Regional series were calculated for precipitation and temperature for the whole Republic of Moldova by averaging the station data. Data for solar radiation and relative humidity were also used to calculate atmospheric evaporative demand according to the FAO-56 Penman-Monteith equation (Allen et al. 1998). Data for these variables were obtained from the ERA5 Reanalysis (Hersbach et al. 2020).

National annual crop yield data for maize, sunflower and grapes from 1950 to 2020 were obtained from the Ministry of Agriculture of the Republic of Moldova. They reflect important long-term fluctuations that may be related to socioeconomic issues (Figure 2.2). For example, crop yields increased from the 1950s to 1990 but the creation of the Republic of Moldova as an independent country was followed by an economic collapse with a decrease in yields of the three crops. Since 2000 crop yields have increased again. In addition to these long-term trends, there are important interannual variations, which can be mostly related to climate, particularly drought variability (Potopová et al., 2020, 2016).

We removed the long-term trends associated with external non-climate factors. Given the temporal complexity of the fluctuations, it was not possible to apply a linear model for this purpose. Instead, we used a simple approach to obtain anomalies by calculating the difference between annual yields and the average yields of the current year and the previous five years. This approach removes the long-term trend and allows a homogeneous series of interannual yield anomalies to be obtained that may be related to climate variability.

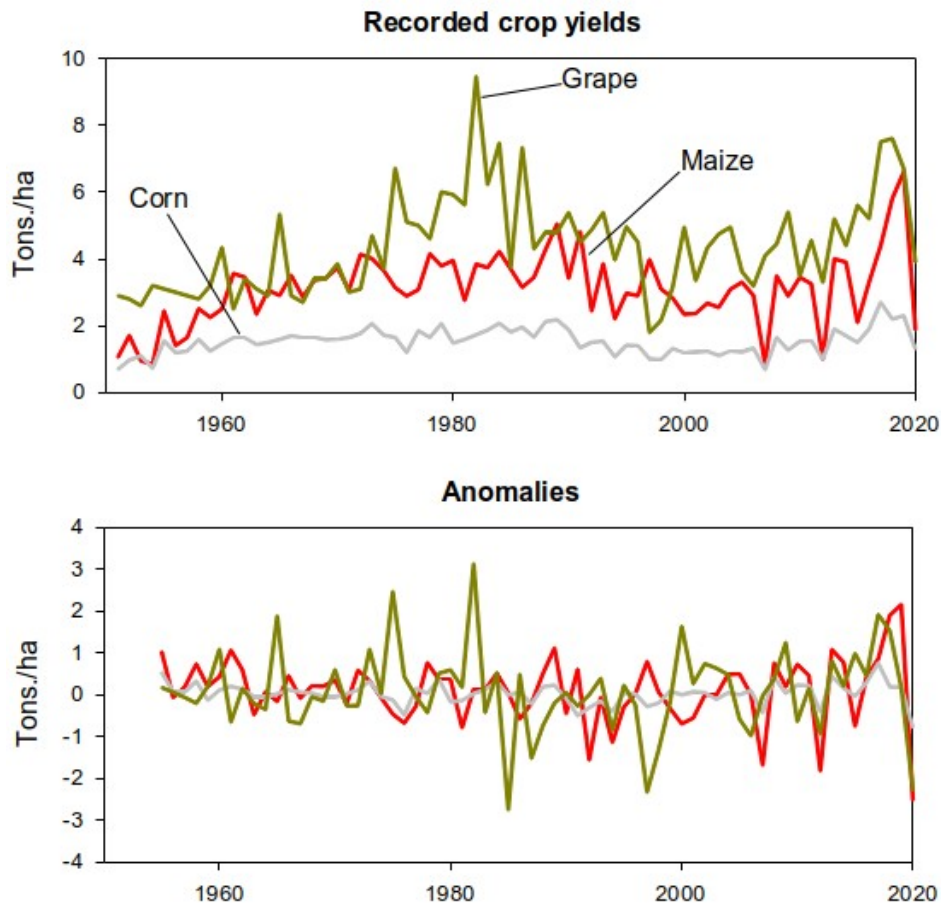


Figure 2.2: Evolution of the recorded crop yields of corn, maize and grape in Moldova (upper panel) and the annual average anomalies for the current and previous five years (lower panel).

Time series of vegetation indices from the Moderate Resolution Imaging Spectroradiometer (MODIS) satellites were used as complementary metrics of crop yields. Vegetation activity was quantified by means of the two-band Enhanced Vegetation Index (EVI2) from the MODIS satellite sensor for the period 2000–2020. EVI2 is more robust than the three-band EVI, which is sensitive to atmospheric disturbances in the blue band. While EVI2 is primarily an indicator of photosynthetic activity, it can also be seen as a proxy of other vegetation parameters (e.g. leaf foliage variations, vegetation coverage, vegetation primary productivity and carbon uptake) (Huete et al., 2002). The MODIS reflectance data used for calculating EVI2 were derived from the MCD43A4 product, retrieved from the NASA repository (<https://modis.gsfc.nasa.gov/data/dataproduct/mod13.php>) at a grid interval of 500 m and averaged to a temporal frequency of 16-days. Curve fitting was applied to the 16-day composite data to extract comparable monthly values using the TIMESAT software package (Jönsson and Eklundh, 2004).

Table 2.1: List of GCM-RCM model chains used in this study

GCM	Run	RCM	Version
CNRM-CERFACS-CNRM-CM5	r1i1p1	CLMcom-CCLM4-8-17	v1
CNRM-CERFACS-CNRM-CM5	r1i1p1	DMI-HIRHAM5	v2
CNRM-CERFACS-CNRM-CM5	r1i1p1	GERICS-REMO2015	v2
CNRM-CERFACS-CNRM-CM5	r1i1p1	IPSL-WRF381P	v2
CNRM-CERFACS-CNRM-CM5	r1i1p1	KNMI-RACMO22E	v2
CNRM-CERFACS-CNRM-CM5	r1i1p1	SMHI-RCA4	v1
ICHEC-EC-EARTH	r12i1p1	CLMcom-CCLM4-8-17	v1
ICHEC-EC-EARTH	r12i1p1	CLMcom-ETH-COSMO-crCLIM-v1-1	v1
ICHEC-EC-EARTH	r12i1p1	DMI-HIRHAM5	v1
ICHEC-EC-EARTH	r12i1p1	IPSL-WRF381P	v1
ICHEC-EC-EARTH	r12i1p1	KNMI-RACMO22E	v1
ICHEC-EC-EARTH	r12i1p1	MOHC-HadREM3-GA7-05	v1
ICHEC-EC-EARTH	r12i1p1	SMHI-RCA4	v1
ICHEC-EC-EARTH	r3i1p1	DMI-HIRHAM5	v2
IPSL-IPSL-CM5A-MR	r1i1p1	DMI-HIRHAM5	v1
IPSL-IPSL-CM5A-MR	r1i1p1	GERICS-REMO2015	v1
IPSL-IPSL-CM5A-MR	r1i1p1	IPSL-WRF381P	v1
IPSL-IPSL-CM5A-MR	r1i1p1	KNMI-RACMO22E	v1
IPSL-IPSL-CM5A-MR	r1i1p1	SMHI-RCA4	v1
MOHC-HadGEM2-ES	r1i1p1	CLMcom-CCLM4-8-17	v1
MOHC-HadGEM2-ES	r1i1p1	CLMcom-ETH-COSMO-crCLIM-v1-1	v1
MOHC-HadGEM2-ES	r1i1p1	DMI-HIRHAM5	v2
MOHC-HadGEM2-ES	r1i1p1	IPSL-WRF381P	v1
MOHC-HadGEM2-ES	r1i1p1	KNMI-RACMO22E	v2
MOHC-HadGEM2-ES	r1i1p1	MOHC-HadREM3-GA7-05	v1
MOHC-HadGEM2-ES	r1i1p1	SMHI-RCA4	v1
MPI-M-MPI-ESM-LR	r1i1p1	CLMcom-CCLM4-8-17	v1
MPI-M-MPI-ESM-LR	r1i1p1	CLMcom-ETH-COSMO-crCLIM-v1-1	v1
MPI-M-MPI-ESM-LR	r1i1p1	DMI-HIRHAM5	v1
MPI-M-MPI-ESM-LR	r1i1p1	KNMI-RACMO22E	v1
MPI-M-MPI-ESM-LR	r1i1p1	MOHC-HadREM3-GA7-05	v1
MPI-M-MPI-ESM-LR	r1i1p1	MPI-CSC-REMO2009	v1
MPI-M-MPI-ESM-LR	r1i1p1	SMHI-RCA4	v1a
MPI-M-MPI-ESM-LR	r1i1p1	UHOH-WRF361H	v1
MPI-M-MPI-ESM-LR	r2i1p1	SMHI-RCA4	v1
MPI-M-MPI-ESM-LR	r3i1p1	GERICS-REMO2015	v1
NCC-NorESM1-M	r1i1p1	CLMcom-ETH-COSMO-crCLIM-v1-1	v1
NCC-NorESM1-M	r1i1p1	DMI-HIRHAM5	v3
NCC-NorESM1-M	r1i1p1	GERICS-REMO2015	v1
NCC-NorESM1-M	r1i1p1	IPSL-WRF381P	v1
NCC-NorESM1-M	r1i1p1	KNMI-RACMO22E	v1
NCC-NorESM1-M	r1i1p1	MOHC-HadREM3-GA7-05	v1
NCC-NorESM1-M	r1i1p1	SMHI-RCA4	v1

We also used daily 500 hPa Geopotential heights (Z500) to identify the atmospheric patterns that cause dry and warm conditions in Moldova, with a particular focus on the 13 months between July 2019 and August 2020. For this purpose, we used the ERA5 reanalysis of the 1950–2020 period.

Climate model simulations for the RCP8.5 scenario were obtained from the Euro-CORDEX project (Gutowski et al. 2016; Jacob et al. 2014; Kotlarski et al. 2014) for the whole of Moldova. We retrieved the series of monthly precipitation and maximum and minimum temperature from 43 regional climate model simulations (see Table 2.1) from 1970 to 2100. Given the relatively small size of the Republic of Moldova (33,844 km²) and the homogeneity of landscape and climate in the country, average series over the whole country were used to assess drought projections in the region.

Finally, wheat crop yields from the experimental plots of the Selectia Research Institute for Crop Research located in Bălți were available for the period 1980–2020. The experiments include one crop rotation where winter wheat is sown after two different predecessors, harvested early and late. As early harvested predecessors the mixture of winter rye and winter vetch for green mass (for feeding cattle) was used and corn for grain as late harvested predecessor (Boincean and Dent 2019).

2.2.2 Methods

We quantified drought severity by means of two drought indices, the Standardized Precipitation Index (SPI: McKee et al. 1993) which is based on monthly precipitation anomalies and the Standardized Precipitation Evapotranspiration Index (SPEI: Beguería et al 2014; Vicente-Serrano et al. 2010), which is based on the difference of precipitation and the atmospheric evaporative demand. The SPI was calculated for the entire 1851–2020 period for the meteorological station at Chisinau, but also for the period 1950–2020 for the other meteorological stations and also for the regionally averaged precipitation series. SPEI was also calculated from the averaged precipitation series and atmospheric evaporative demand for the period 1950–2020.

We used two methods to calculate the atmospheric evaporative demand, the FAO-56 Penman-Monteith mentioned above and the Hargreaves–Samani equation (Hargreaves and Samani 1985) which is based only on maximum and minimum temperature. As observed in other regions of Europe (Vicente-Serrano et al. 2014), both methods provide similar temporal variability and trends. Considering that the main driver of global trends in atmospheric evaporative demand is the temperature increase (Vicente-Serrano et al. 2020), we decided to calculate the atmospheric evaporative demand using the Hargreaves and Samani method for the period of observations and for the future projections. SPI and SPEI were also calculated for regional series of precipitation and atmospheric evaporative demand for each climate model projection for the period 1970–2100. We calculated the evolution of SPI and SPEI over the period of

the year showing the highest correlation with the crop yields over the period of observations. We also calculated the duration of drought events considering a threshold of 1 in 20 years ($Z \leq 1.65$) according to the normal distribution that characterizes SPI and SPEI in each model and calculated the annual average of the drought duration from the different models.

Changes in precipitation were analysed by means of a temporal spectral analysis to determine possible cycles and short and long-term periodicities. For this purpose, we focused on the long-term series for Chisinau that can be considered as representative of the general precipitation variability over the whole country. We use the Continuous Wavelet Transform (Torrence and Compo 1998) to localize in both time and periodicity the transient patterns embedded in the precipitation time series. Thereby, we obtain information about the dominant timescales of underlying processes and hence sources of variability across timescales. In this research, we make use of the Morlet wavelet, which has been successfully used to analyze hydrological time-series (Juez et al. 2021; Labat et al. 2005). Time series were standardized (zero mean, unit standard deviation) before applying the Continuous Wavelet Transform.

The relationship between the climate variability and the interannual variability of different crop yields was assessed by means of correlation analysis. For this purpose, we used the complete period of record, and correlations were calculated considering different periods of accumulation of the precipitation, temperature and the atmospheric evaporative demand. This allowed us to determine the periods of the year that most affect the interannual variability of crop yields. The same approach was followed to analyse the relationship between vegetation activity by means of the EVI2 and the climate variables for the period 2000–2020. For comparison, correlations between the annual crop yields and climate variables were also analysed for the period 2000–2020. To identify possible temporal changes and correlations in the relationship between precipitation and crop yields we used the squared wavelet coherence following the approach of Grinsted et al. (2004), i.e. a direct correlation between the wavelets of both precipitation and crop yields, and moving window correlations between precipitation and crop yields considering intervals of 15 years.

To characterize the atmospheric circulation over Eastern Europe, we define six weather regimes (WRs) based on daily anomalies of Z500 (defined as departures of the daily fields from the 1981–2010 daily climatology computed using a 15-day centered running mean) over the domain 0°E–55°E, 30°N–65°N during the period 1950–2020. Following Ayarzagüena et al. (2018) and Garrido-Perez et al. (2020), WRs were computed by applying a k-means clustering algorithm to area-weighted Z500 anomalies after their reconstruction by means of an empirical orthogonal function (EOF) analysis. The choice of the final number of clusters has been made as a reasonable compromise between the anomaly correlation coefficient and the sum of squares.

2.3 Results

2.3.1 Evolution of drought severity

The long-term evolution of meteorological droughts in Moldova does not show a declining trend over the last decades (Figure 2.3). Thus, considering the long-term period 1850–2020 in Chisinau (Figure 2.4), the evolution of SPI shows a positive long-term trend, indicative of a decrease in the severity of drought events, which were particularly strong in the 1890s and 1900s, in agreement with the pattern observed in neighboring areas of Ukraine (Kleschenko and Zoidze, 2005). Precipitation in Moldova does not show clear cycles over the long term (Figure 2.5) with no relevant temporal differences in periodicities over the last 170 years (Figures 2.6 and 2.7 and Table 2.2). This stresses the random character of drought events in the region and the difficulties of establishing long-term drought forecasting approaches.

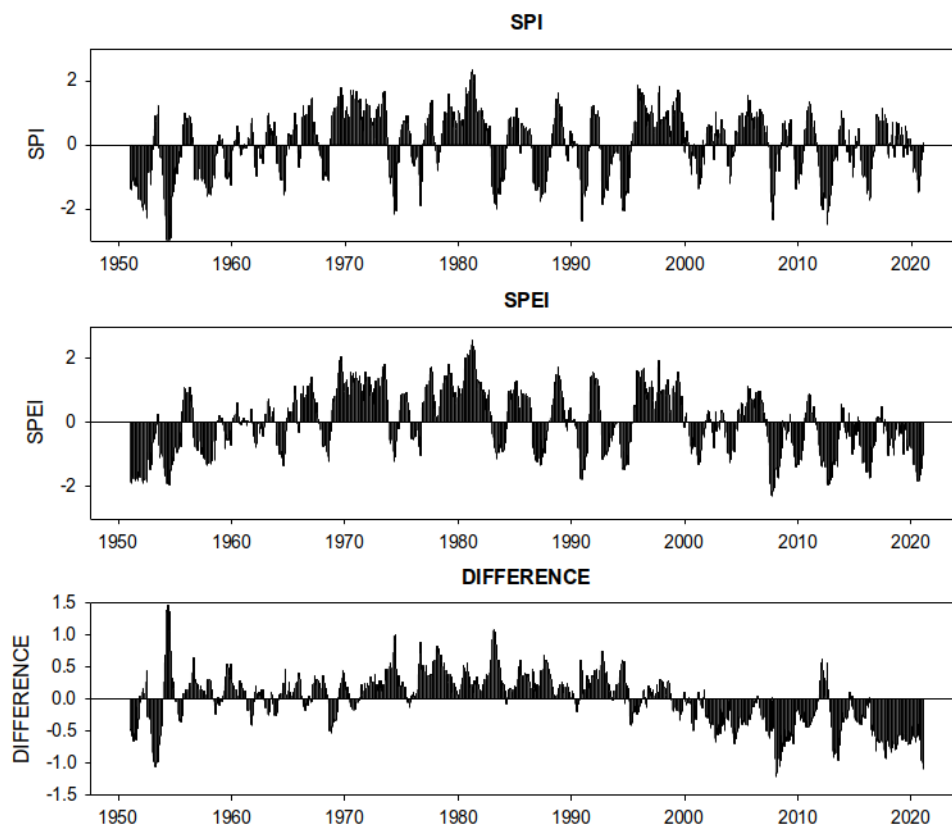


Figure 2.3: Evolution of the SPI and SPEI from the national average series for Moldova and the difference between them.

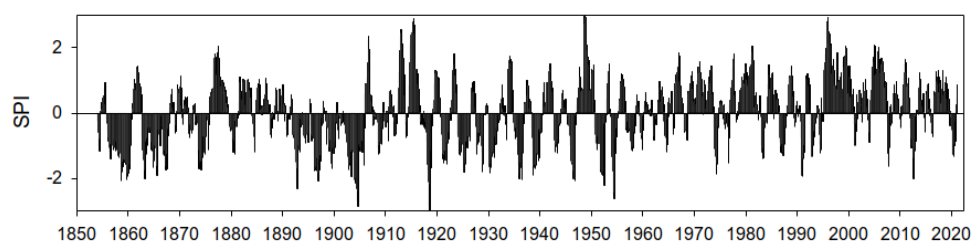


Figure 2.4: Evolution of the 12-month SPI for Chisinau from 1850 to 2020

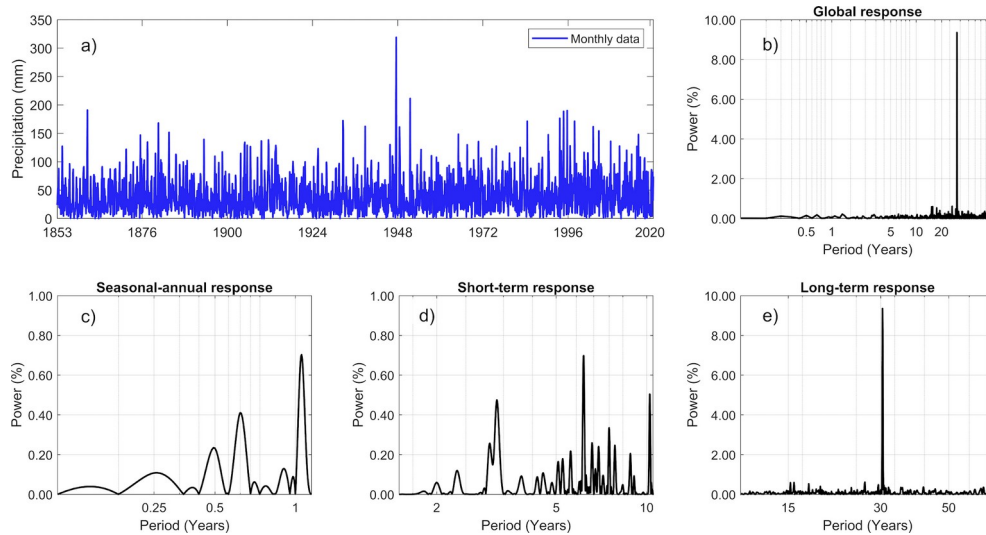


Figure 2.5: Spectral characteristics of precipitation time-series recorded during the period 1853–2020 at Chisinau station. (a) Time-series of monthly precipitation records; (b) Global wavelet periodogram expressed as percentage of total global power summed over all periods. Time-scales beyond the dominant annual time-scale are identified and magnified in the bottom figures; (c) Seasonal-annual response; (d) Short-term annual response; and (e) Long-term-annual response.

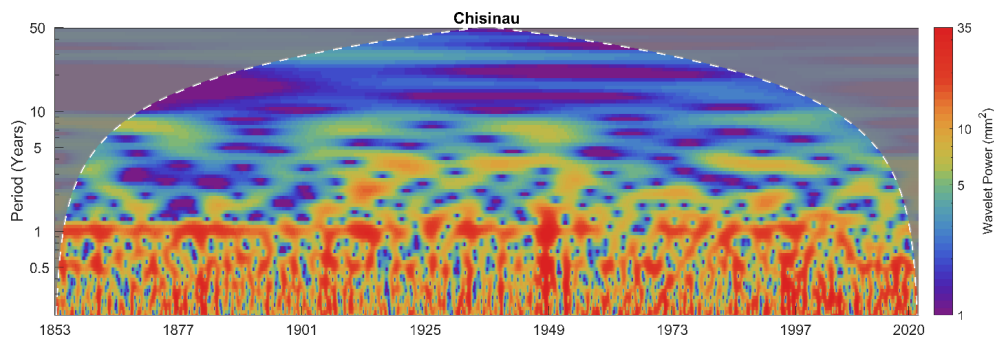


Figure 2.6: Local wavelet power spectrum of the monthly precipitation time-series. The vertical axis is the wavelet time-scale and the horizontal axis is the time position during the period 1853–2020 at Chisinau station. The thick white dashed curve depicts the cone of influence below which the edge effects on the amplitude of the local power spectrum are negligible (Torrence and Compo, 1998).

Table 2.2: Summary of the temporal variance fraction accounted by each dominant time-scale determined based on the local and global power spectra displayed in Figures 2.6 and 2.7. The variance fractions were obtained by applying the standard statistical variance formula to each wavelet time-series. Percentages in parentheses give incremental percentage of such temporal variance as the sum of the time-scales.

Time scale	Temporal fraction – Precipitation
Seasonal–annual (< 1.5 years)	0.88 (88%)
Short-term annual response (1.5–10.5 years)	0.10 (98%)
Long-term annual response (10.5–50.0 years)	0.02 (100%)

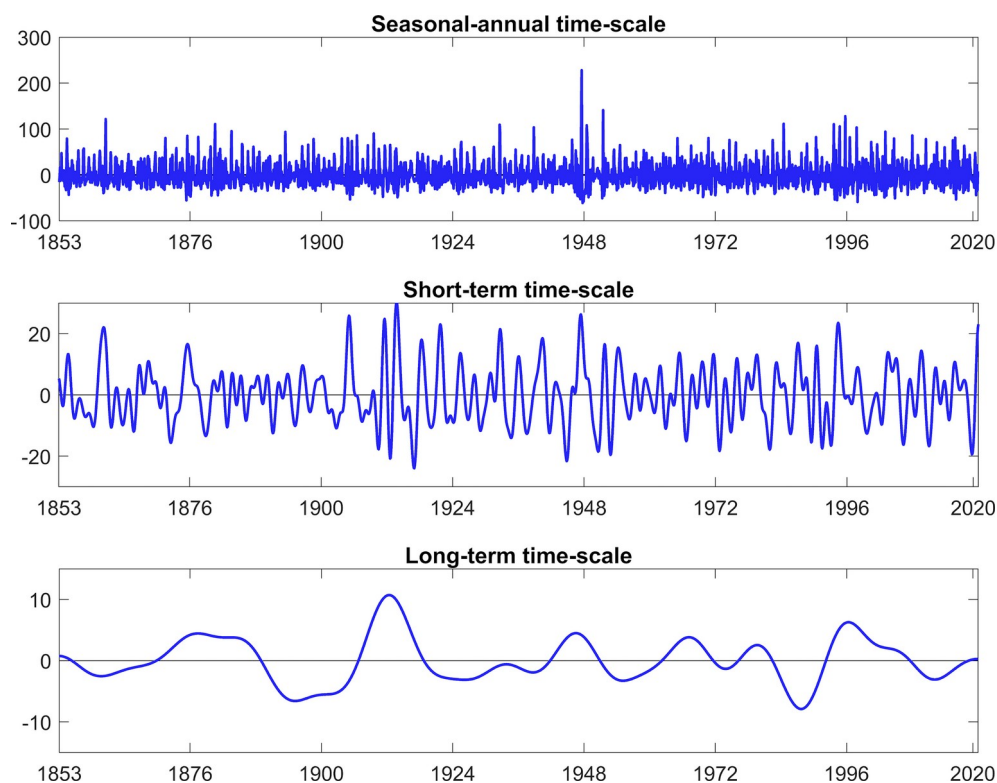


Figure 2.7: Temporal scale-by-scale decomposition of monthly precipitation time-series anomalies (mm/month). Positive and negative anomalies were calculated with respect to the mean values. The three non-overlapping time-scales bands contain the major power peaks and were determined based on the global power spectra displayed in Figure S1. Seasonal-to-annual time-scales represent a time band of 0.083 to 1.5 years; short-term-annual time-scale depicts a time band of 1.5 to 10.5 years; and long-term-annual time-scale is related with a time band of 10.5 to 50.0 years.

2.3.2 Relationship between the drought indices and crop yields

The evolution of SPI from 1950 to 2020 for the different meteorological stations available in Moldova shows strong correlation ($r > 0.8$) with similar duration and severity of meteorological droughts. The average SPI obtained for the whole country shows the most severe drought events in the decade of the 1950s. The 1980s, 1990s and 2010s were also characterized by some severe meteorological droughts, particularly in 2012 (Figure 2.8). The drought that affected Moldova in 2020 and caused a strong decline in crop yields was not as severe as previous droughts from a meteorological point of view.

Maize and sunflower annual yields show significant correlations with the precipitation recorded between November–December of the previous year and July of the current year. Correlations are stronger for maize yields than for sunflower (Figure 2.9). On the contrary, there is a weak correlation between precipitation and grape yields, indicating the insensitivity of this crop to precipitation variability. Maize and sunflower annual yields also show a negative relationship with temperature and the atmospheric evaporative demand for the majority of months of the year (Figures 2.10

and 2.11). Thus, high temperatures and atmospheric evaporative demand during the entire growing season show a negative correlation with annual yields, suggesting that the hydraulic stress caused by temperature is more relevant than its role in promoting photosynthesis. Again grape yields show a low sensitivity to the interannual variability of these climate variables.

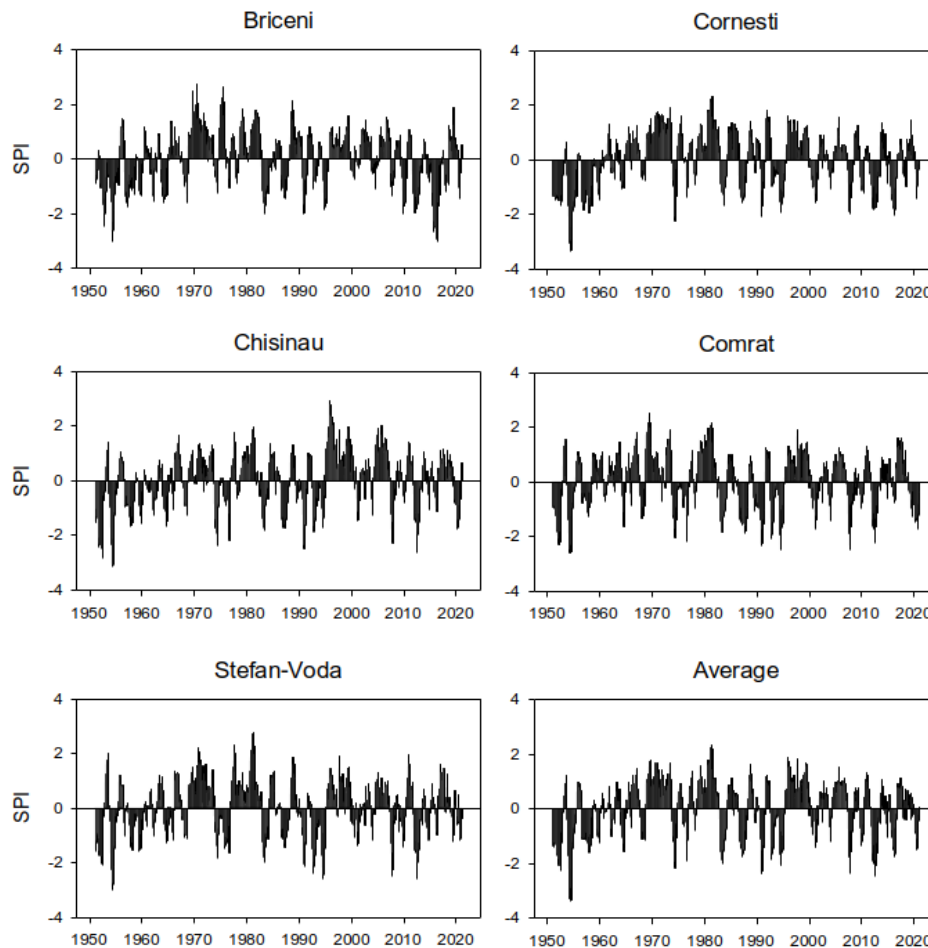


Figure 2.8: Evolution of the SPI in the five meteorological stations used in this study and from the average precipitation series.

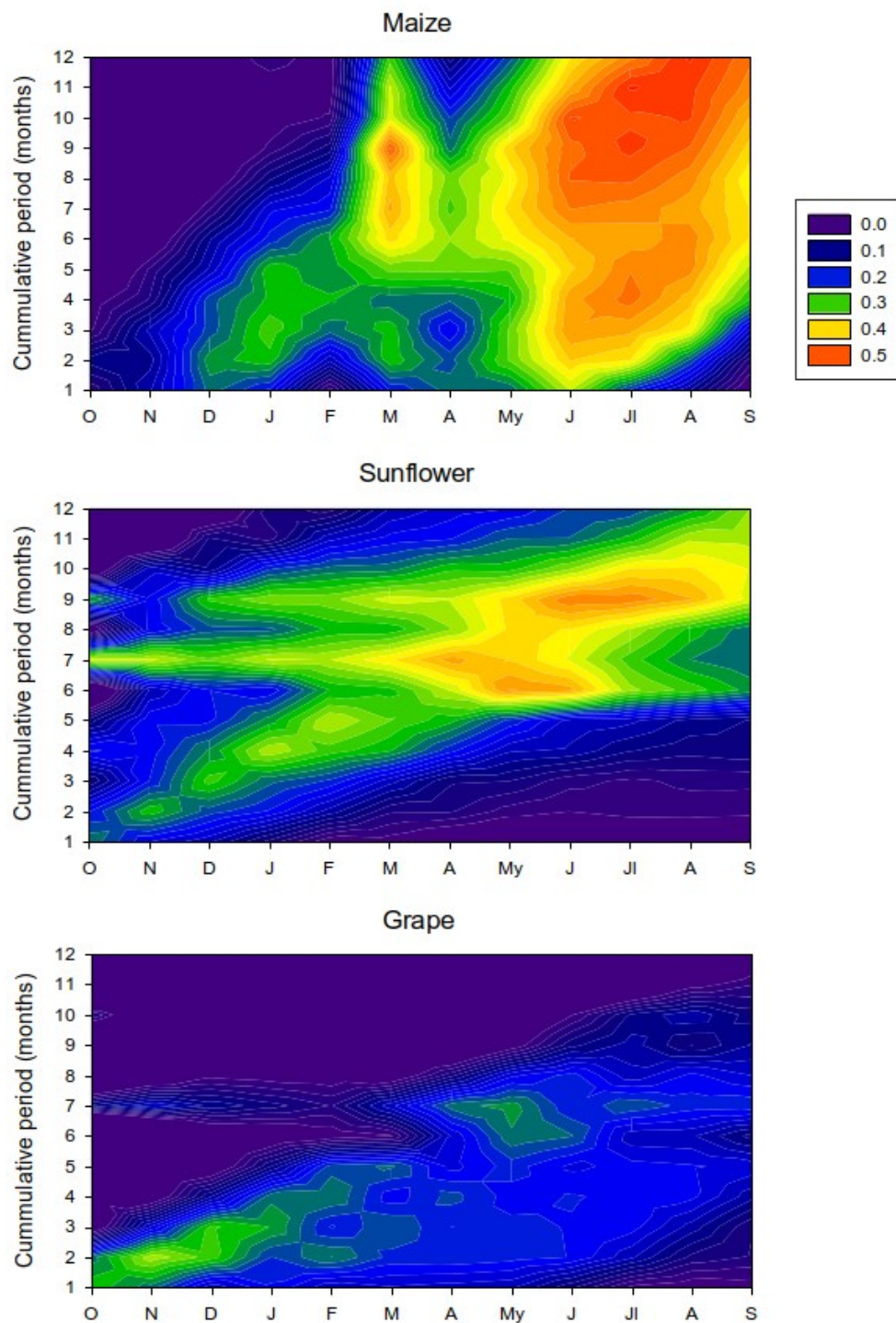


Figure 2.9: Monthly correlations between precipitation accumulated over different temporal scales and the crop yields of maize, sunflower and grape in Moldova. Significant correlations ($p > 0.05$) correspond to Pearson's $r > 0.23$.

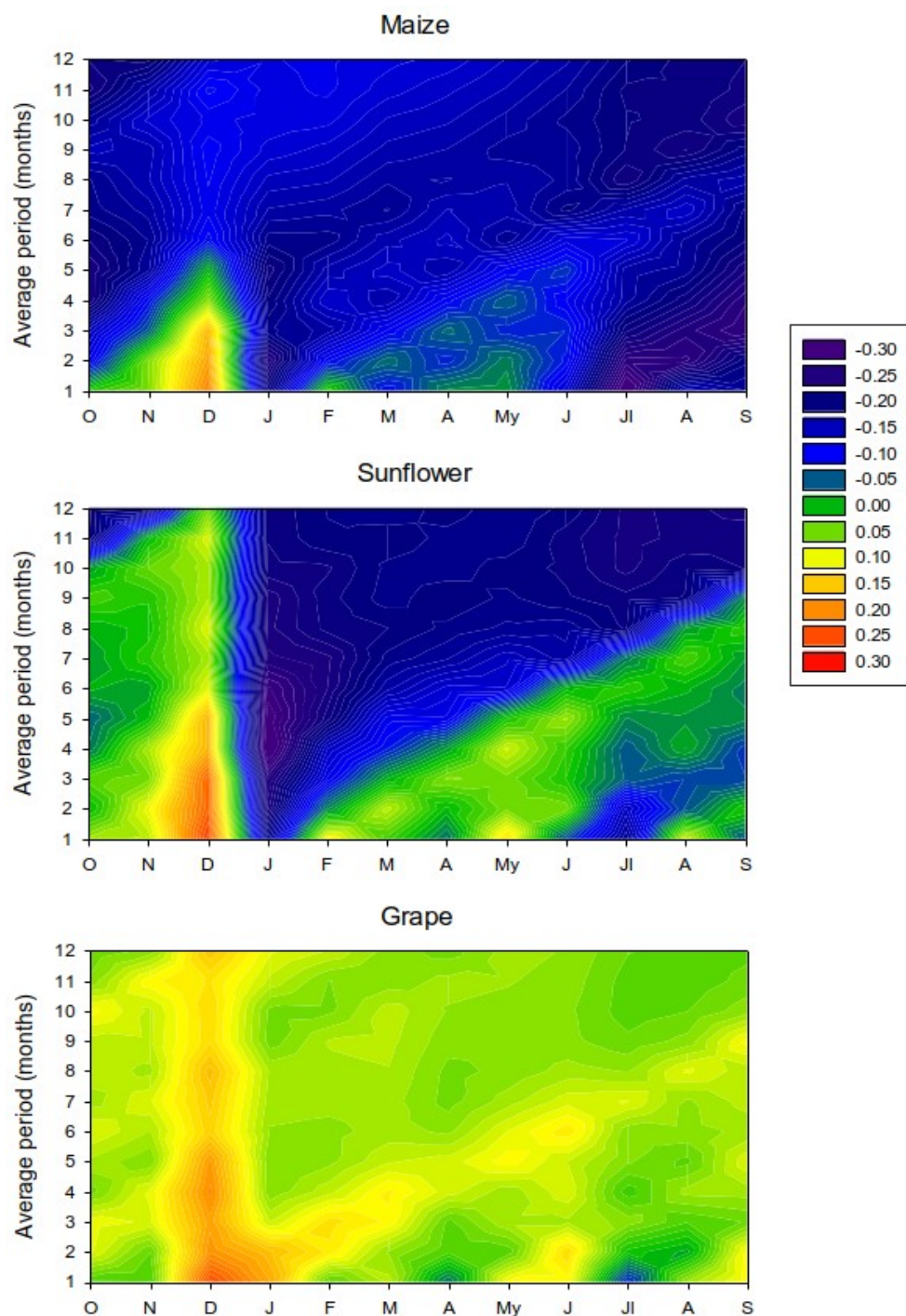


Figure 2.10: Monthly correlations between maximum temperature accumulated over different temporal scales and the crop yields of maize, sunflower and grape in Moldova.

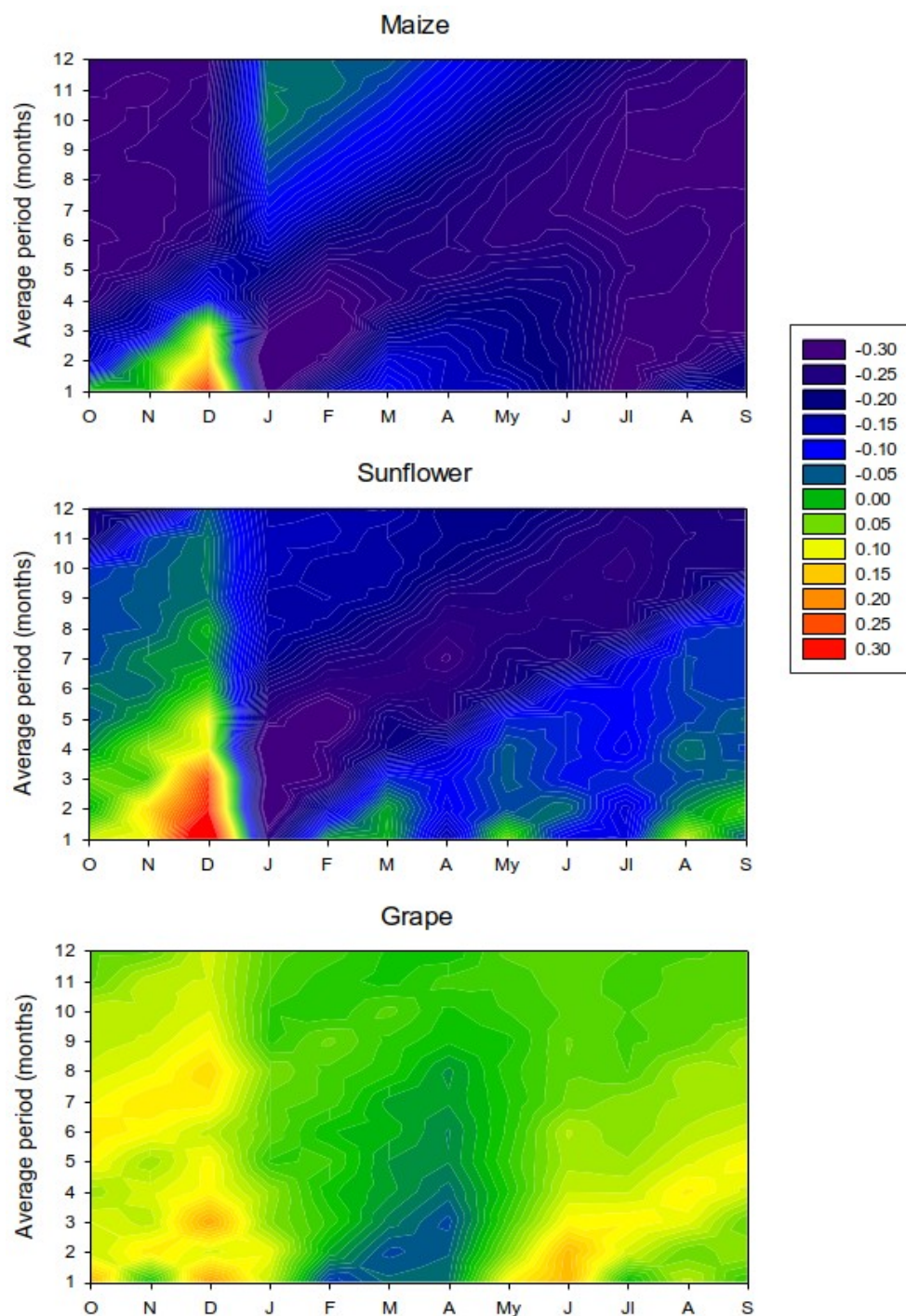


Figure 2.11: Monthly correlations between Penman-Monteith reference evapotranspiration accumulated over different temporal scales and the crop yields of maize, sunflower and grape in Moldova.

3.3 Correlations between MODIS vegetation indices and crop yields

For the period 2000–2020 there is a strong correlation between the maize and sunflower crop yields and the MODIS vegetation indices, particularly during summer months (Figure 2.12). Thus, the correlation between the different climate variables and the monthly EVI2 series shows patterns coherent with the relationship found between the maize and sunflower yields and climate.

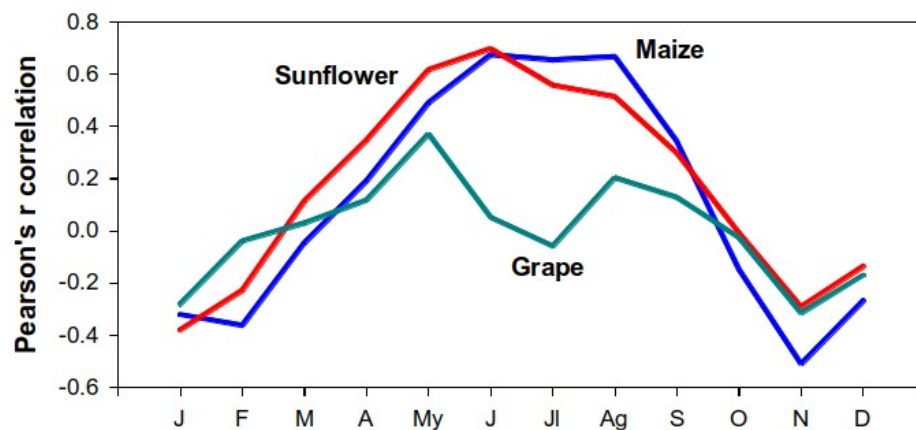


Figure 2.12: Correlation between the monthly EVI in crop lands and the annual yields of maize, sunflower and grape within the years 2000–2020.

There is a positive correlation between EVI2 and summer precipitation, with maximum correlation for the period between November and July (Figure 2.13). In addition, there are negative correlations with summer temperature and atmospheric evaporative demand, strongest for the latter. Moreover, the magnitude of these correlations is stronger than that recorded between crop yields and climate variables for the study period 1950–2000. Nevertheless, these results do not mean that vegetation activity shows stronger response than crop yields to the climate variability.

Analyzing the correlations between crop yields and climate variables for the same period of the EVI2 data (2000–2020), we also find stronger correlations than those found for the whole period of analysis (Figures 2.14–2.16). Moreover, the patterns of correlation with the different precipitation accumulations are equivalent to those obtained with the EVI2 data for this period. This suggests a reinforcement of the relationship between climate variability and crop yields during the last two decades in relation to what was observed in previous decades.

The evolution of crop yields clearly shows a stronger relationship with precipitation for maize and sunflower from the 2000s onwards (Figure 2.17). Nevertheless, the crop yield decrease of 2020 was stronger than expected from the observed reduction of precipitation. The years 2007 and 2012 showed lower precipitation but these years were not affected by such a large crop yield decrease.

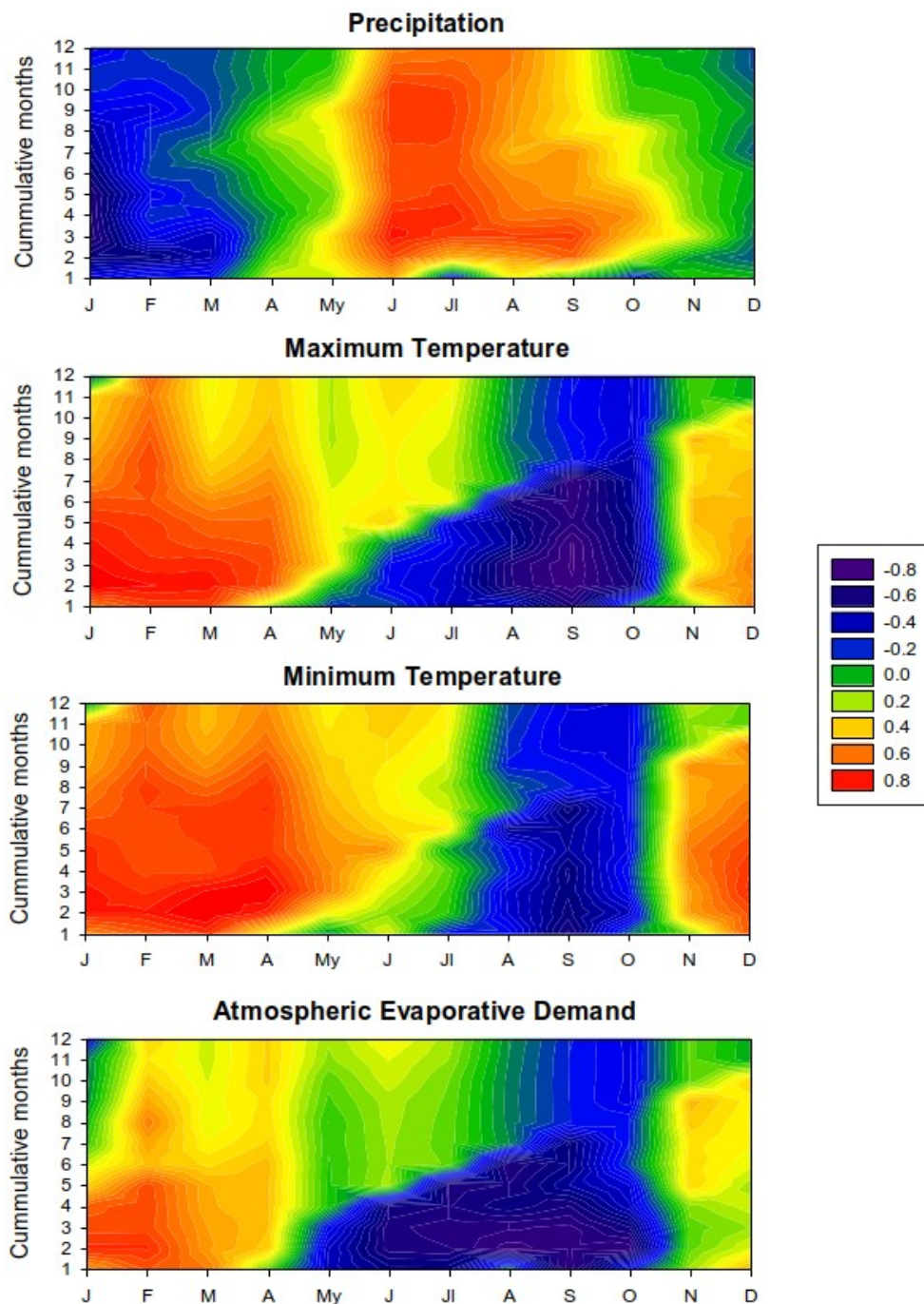


Figure 2.13: Pearson's r correlations between the monthly EVI2 and the monthly meteorological variables accumulated over different temporal scales for the period 2000–2020

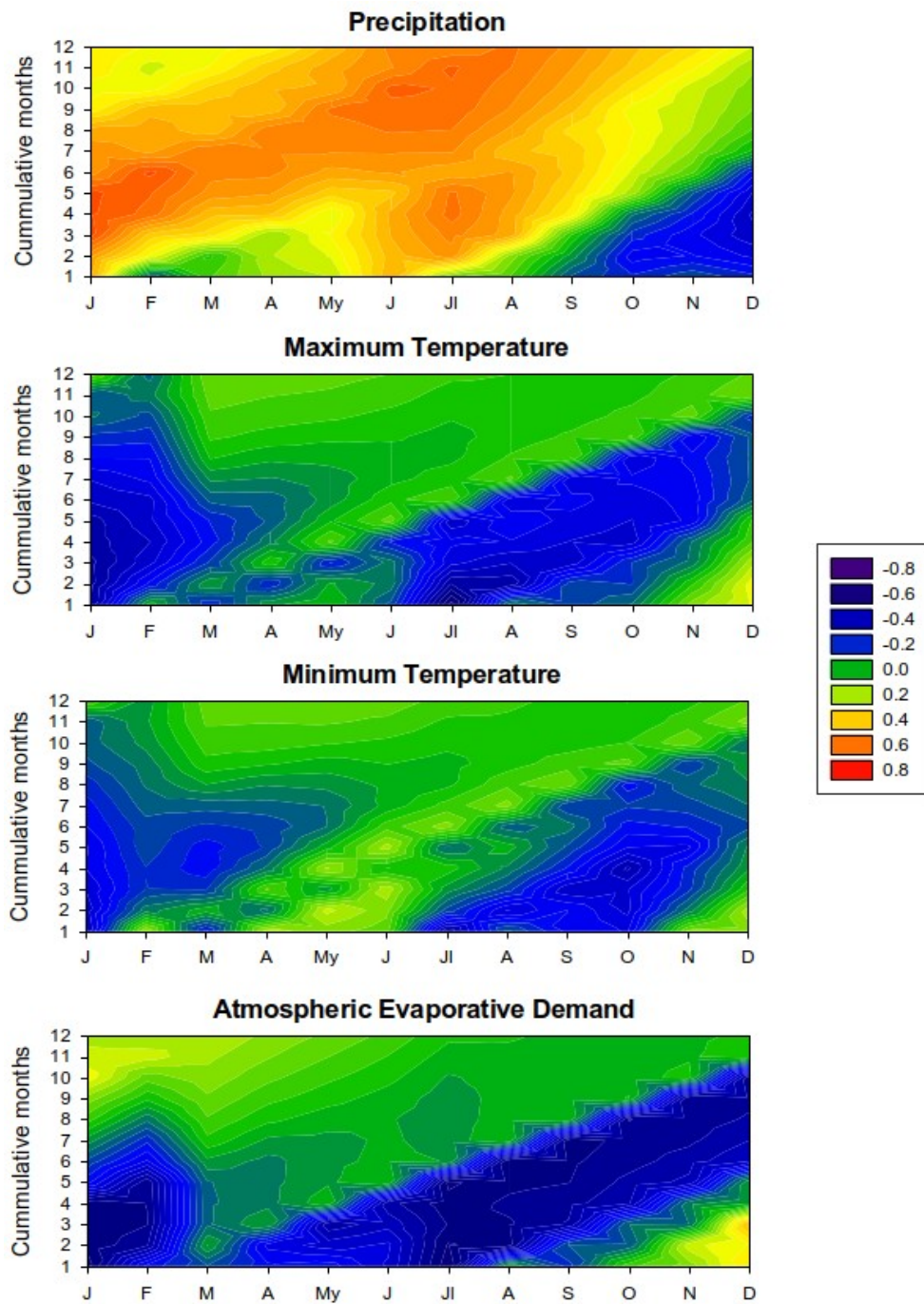


Figure 2.14: Pearson's r correlations between the maize yield and the monthly meteorological variables accumulated over different temporal scales for the period 2000–2020.

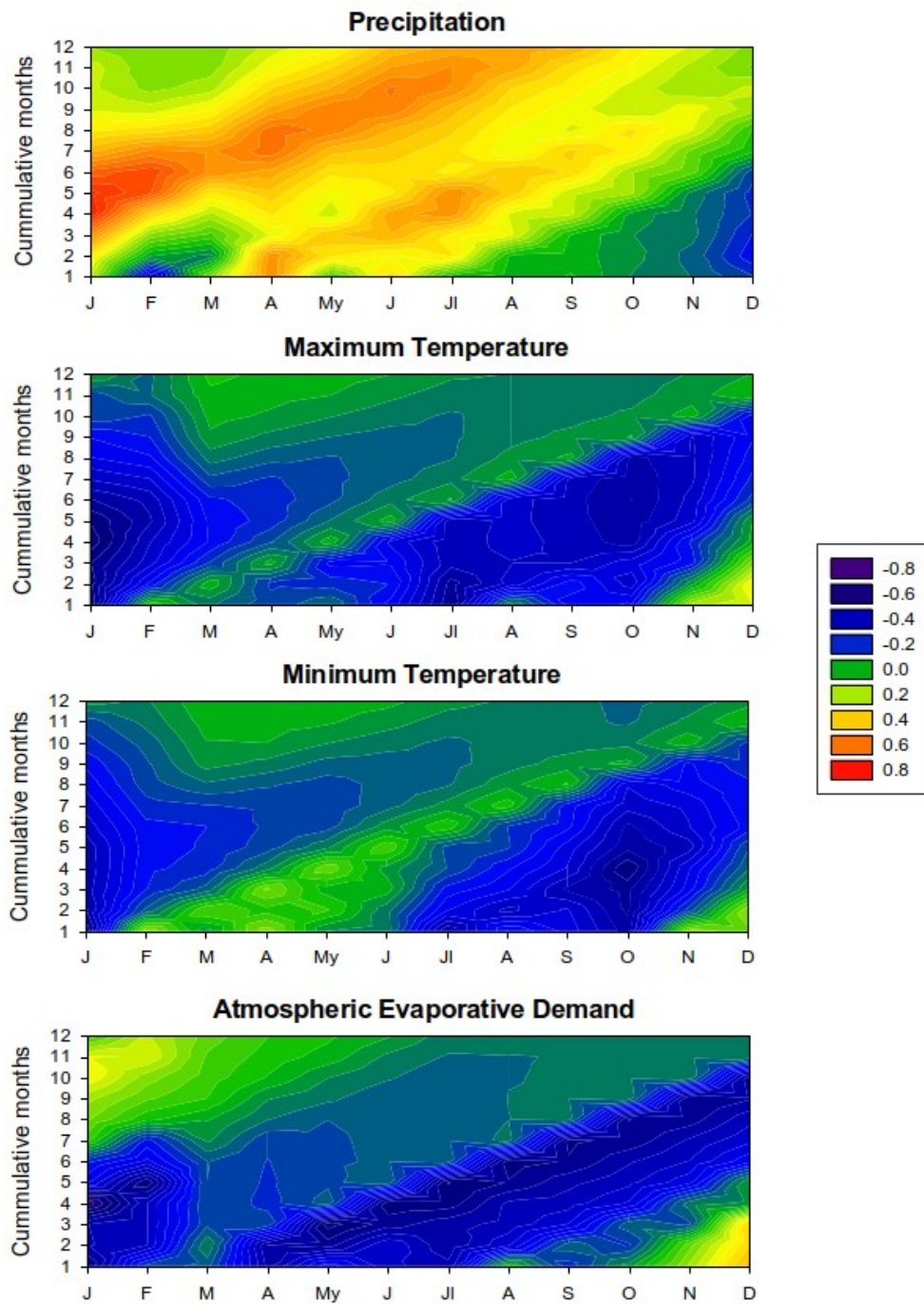


Figure 2.15: Pearson's r correlations between the sunflower yield and the monthly meteorological variables accumulated over different temporal scales for the period 2000–2020.

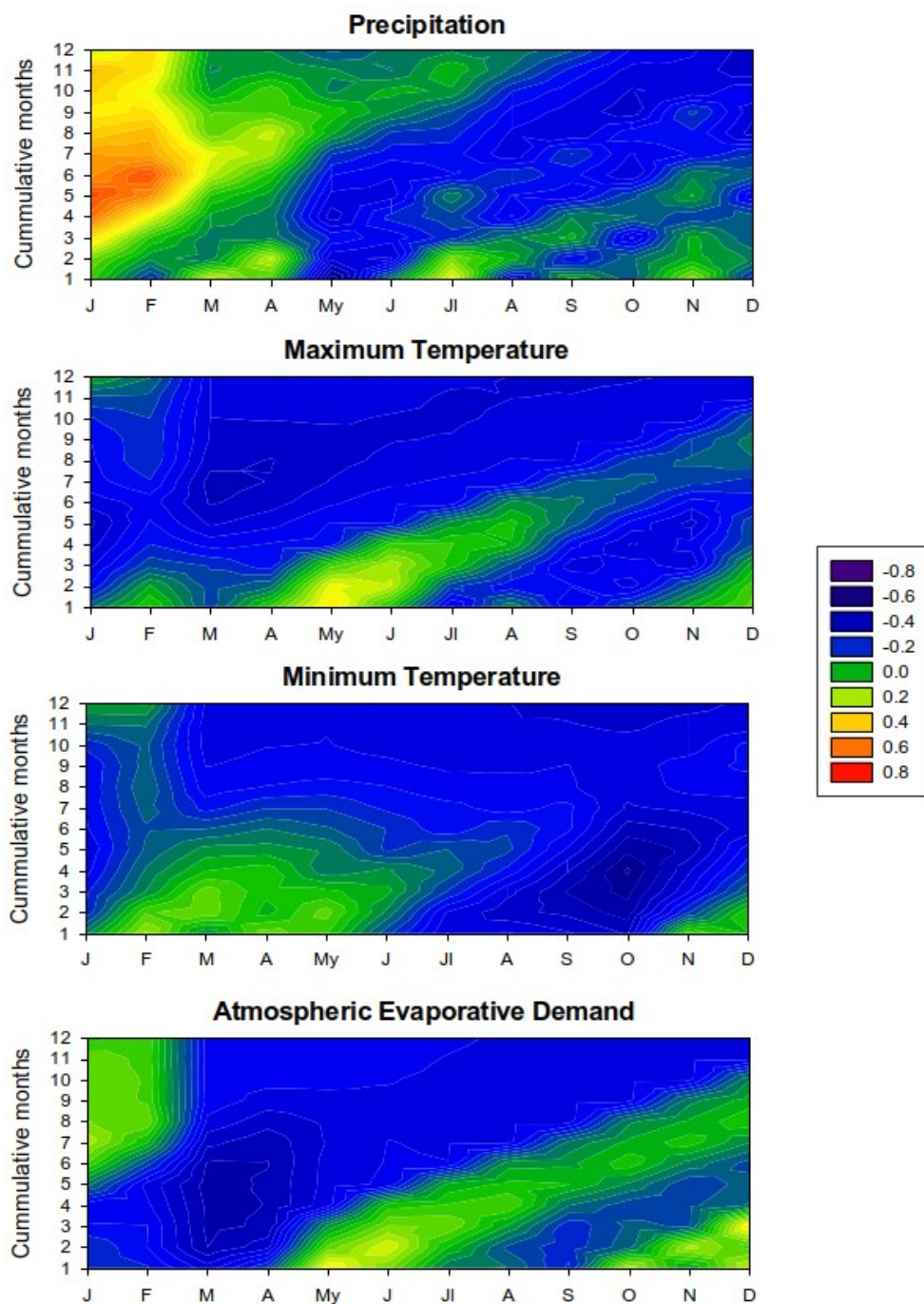


Figure 2.16: Pearson's r correlations between the grape yield and the monthly meteorological variables accumulated over different temporal scales for the period 2000–2020.

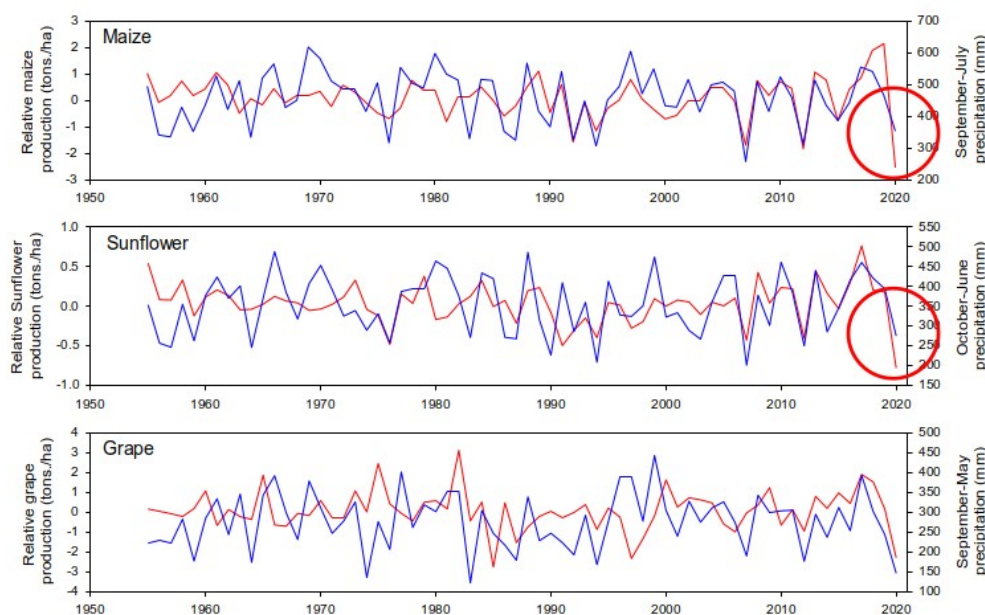


Figure 2.17: Evolution of the temporal variability of precipitation during the period of higher correlation with the anomalies in crop yield and the annual yields of the three crops. Yields for 2020 are marked for maize and sunflower.

2.3.4 Changes in the relationship between crop yields and precipitation

There is a clear change in the relationship between precipitation variability and maize and sunflower yields in the last two decades (Figure 2.18a). This is clearly observed with the wavelet coherence between precipitation and maize and sunflower yields showing dominance of a relationship between both variables at long periods (8 years) between 1950 and 2000, only after 2000 the relationship is recorded at higher frequencies, with a maximum considering one year. In addition, analysis of moving window correlations between precipitation and crop yields with periods of 15 years show a clear positive trend toward higher correlations in the three crops (Figure 2.18b), indicating that crop yields became more sensitive to the precipitation variability in the last two decades.

We further explore the factors that may drive the reinforcement of the role of precipitation variability in explaining annual crop yields. We observe a strong increase in temperature that starts in 2000 (Figure 2.19). From 2000 to 2020 the average annual temperature has increased by 2 K, which is a very strong trend for such a short period. Warming is mostly concentrated in summer. This strong temperature increase has caused a noticeable increase in the atmospheric evaporative demand, which has reinforced the severity of drought events.

Analyzing the difference between the evolution of SPI and SPEI, it is observed that the drought events that affected Moldova from 2000 onwards were clearly reinforced by the drying effect of enhanced atmospheric evaporative demand, which was particularly acute during the

2020 drought (Figure 2.03). The evolution of the negative departure of SPEI from SPI shows a clear negative trend and strong reinforcement of the severity of drought events from 2000 driven by evaporative demands from rising temperature.

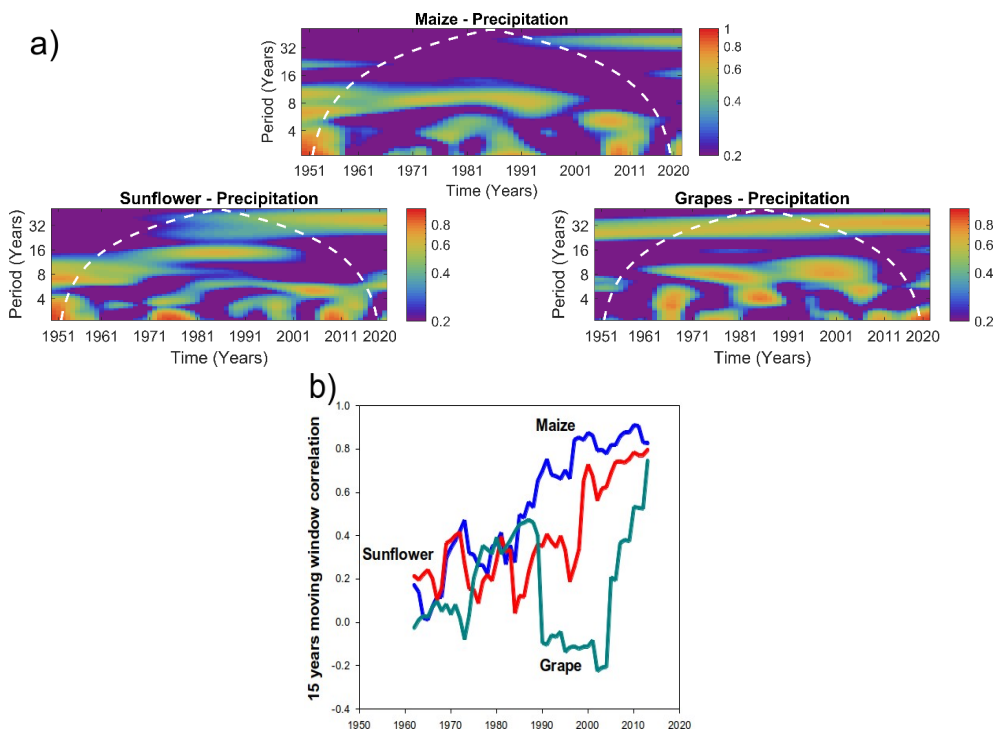


Figure 2.18: a) Squared wavelet coherence between the three selected agricultural yields and precipitation time-series during the period 1951-2020. The vertical axis is the time-scale and the horizontal line is the time position. The dashed curve depicts the cone of influence within which the edge effects are negligible (Torrence and Compo, 1998). The shaded contours indicate the strength of the coherence. Regions where coherence is significant above the 60% level are plotted with warm colors. b) Moving window correlations between annual crop yield in maize, sunflower and grape and the precipitation for the period with stronger correlation.

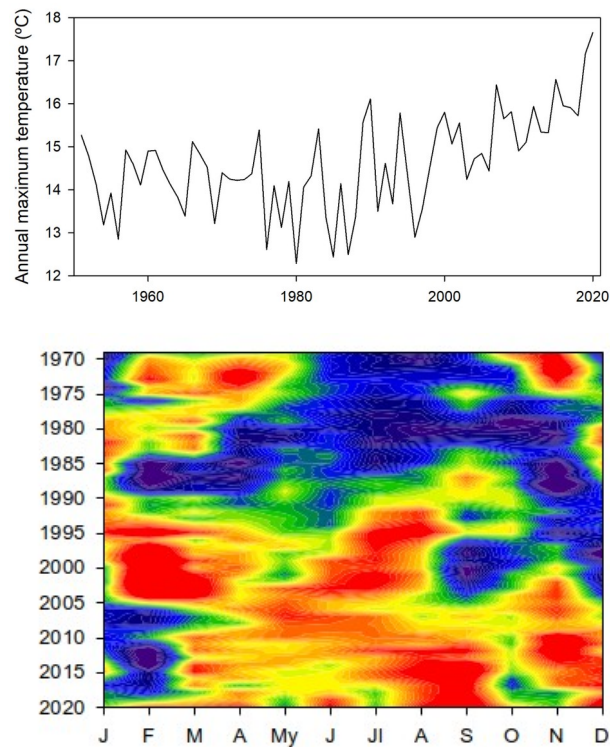


Figure 2.19: Upper panel: Evolution of annual maximum temperature in Moldova. Lower panel: Magnitude of the linear trend of monthly temperature in periods of 30 years. The end year of the period is recorded in the y-axis.

3.5 Frequency of different atmospheric circulation patterns in 2020

The period from July 2019 to August 2020 was particularly dry as a consequence of anomalous atmospheric conditions that favored both low precipitation and high temperature. Figure 2.20a shows the dominant atmospheric configurations in Eastern Europe, which were selected according to a WR cluster analysis (see Methods).

The fact that none of the six WRs shows a frequency of occurrence within the climatological interquartile range proves that the atmospheric circulation was especially uncommon during this period (Figure 2.20b). In particular, WR1 leads to lower precipitation (Figure 2.20c) and higher temperature (Figure 2.20d) than the other WRs due to the associated anticyclonic anomaly over central and eastern Europe. Therefore, the high occurrence of WR1 (above the 90th percentile) explains the low precipitation (below the 5th percentile) and the very extreme temperatures (above the 99th percentile) that characterized the 2020 drought.

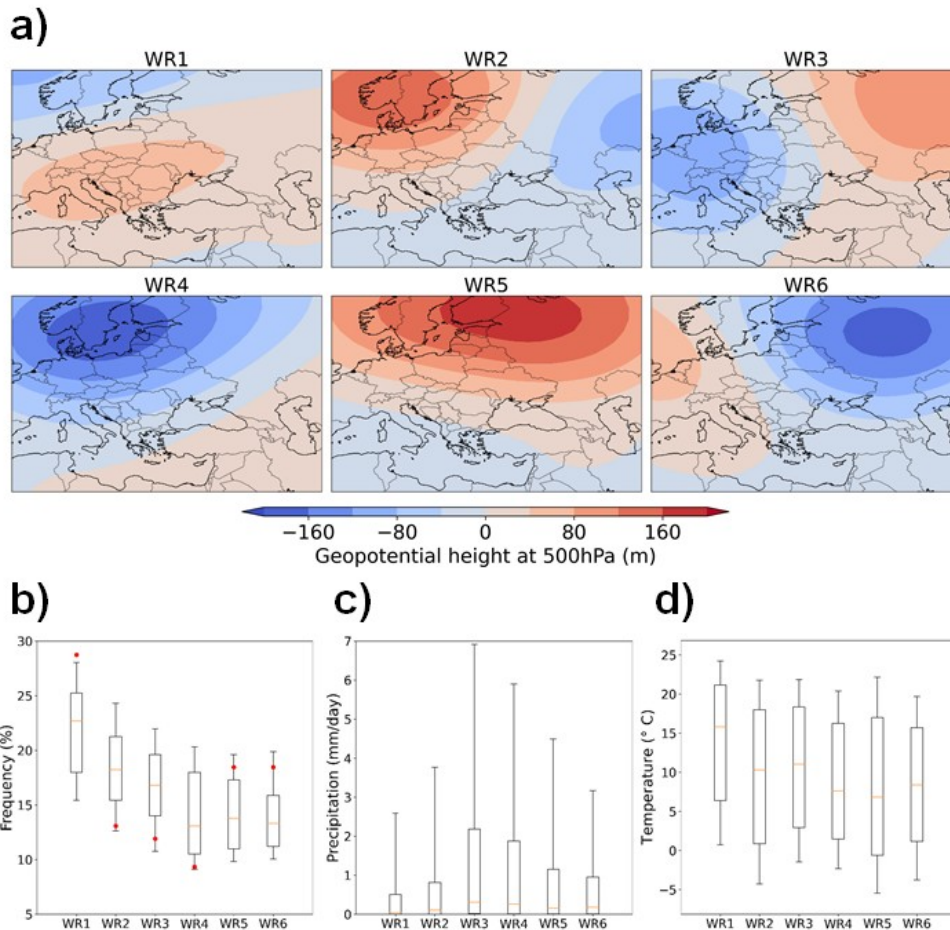


Figure 2.20: a) Main patterns of atmospheric circulation in Eastern Europe derived from the ERA5 reanalysis for the period 1950–2020. Colors show the 500 hPa geopotential height anomalies in metres. b) Frequency distributions of days in each pattern of atmospheric circulation for the 13-month July–August 1950–2020 climatology (boxplots). Red circles correspond to the July 2019–August 2020 period. The boxes extend from the lower (Q1) to the upper (Q3) quartile values of the data, with a horizontal line indicating the position of the median (Q2). The whiskers extend from the boxes to show the range of the data between the 10th and 90th percentiles. c) Distributions of daily precipitation in Moldova (considering the grid cell closest to Chisinau) corresponding to the different atmospheric circulation patterns. d) Distributions of temperature in Moldova corresponding to the different atmospheric circulation patterns.

3.6 Projected changes in the drought patterns

Observations show that increasing temperatures are negatively affecting crop yields in Moldova. Future projections based on climate change scenarios show that this situation will continue to worsen crop yields in the region, in the absence of adaptation. Figure 2.21 shows the simulations of temperature and precipitation for Moldova from 43 CORDEX models for the period 1970–2100, according to the emission scenario RCP8.5.

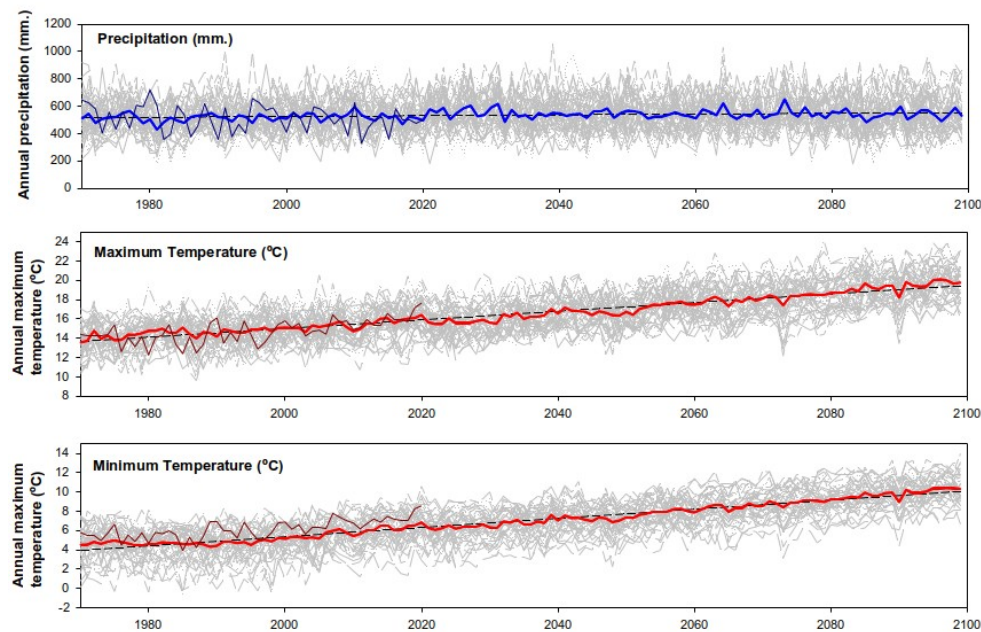


Figure 2.21: Evolution of annual precipitation, maximum and minimum temperature from 43 climate models considering the historical period (1970–2005) and the RCP8.5 scenario (2006–2100). Grey lines represent the individual models and colour lines the average of the different models. Black line represents the regression line and dark colours the evolution of observations for Moldova.

During the historical period between 1970 and 2005 there is high agreement between the long-term average of observations and the ensemble mean simulations. While the observed values of minimum temperature tend to be higher than those simulated by the models, both series reproduce very well the strong temperature increase observed in the last two decades. Precipitation shows stationary behaviour between 1970 and 2005, while the future evolution from the models does not show notable precipitation changes during the twenty-first century. On the contrary, temperature is projected to increase substantially with maximum temperature projected to increase more than 4 K in the period 2070–2100 relative to 1970–2020.

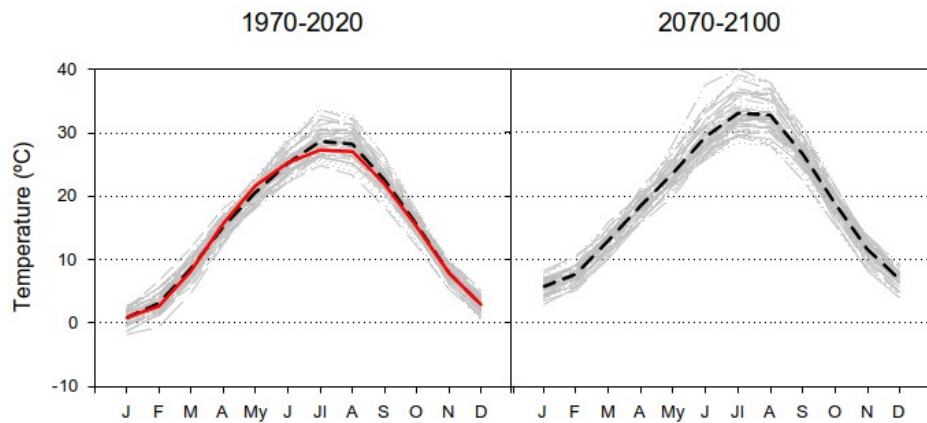


Figure 2.22: Distribution of monthly maximum temperature from the different climate models (grey lines) for the periods 1970–2020 and 2070–2100. Dashed black lines represent the average of the models and red line the observed temperature for the period 1970–2020.

Summer would be the most affected season (Figure 2.22). The climate projections of drought severity do not show changes in the duration of the extreme drought events (1 in 20 years) based on the SPI (Figure 2.23), but do show strong increases in the duration of droughts based on SPEI, particularly from 2070 to 2100. These longer droughts are also characterized by more negative SPEI values during summer, which is presently the period most strongly correlated with annual crop yields.

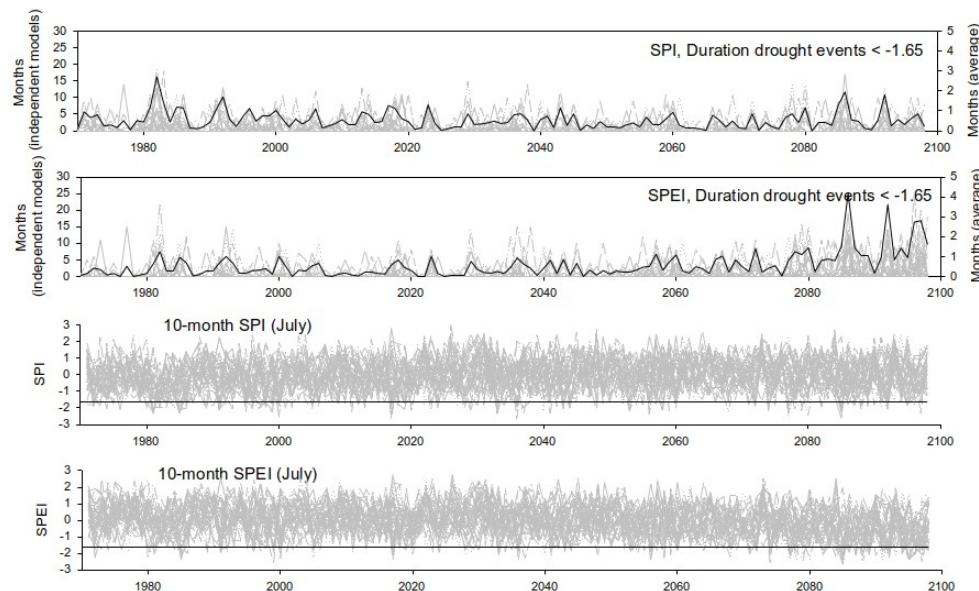


Figure 2.23: Evolution of drought duration from 43 climate change models in Moldova using the SPI and the SPEI. Gray lines show the evolution for each model and black lines represent the average. The two bottom plots show the evolution of the SPI and SPEI at the time scale of 10 months in July. Horizontal black line represent SPI and SPEI values equal to -1.65 .

3.7 Strategies for adaptation under a warmer climate

Given the increasing role of temperature on crop yields in Moldova and its projected future increase, it is necessary to consider possible strategies of crop management in the region to deal with new climate conditions. Here we focus on wheat production. Crop rotation experiments managed by the Selectia Crop Research Institute from the 1980s allow evaluation of two different strategies to improve crop yields in response to droughts. The results show that wheat yields in rotation after rye and vetch are statistically significantly different to the wheat yields after corn rotation (Figure 2.24).

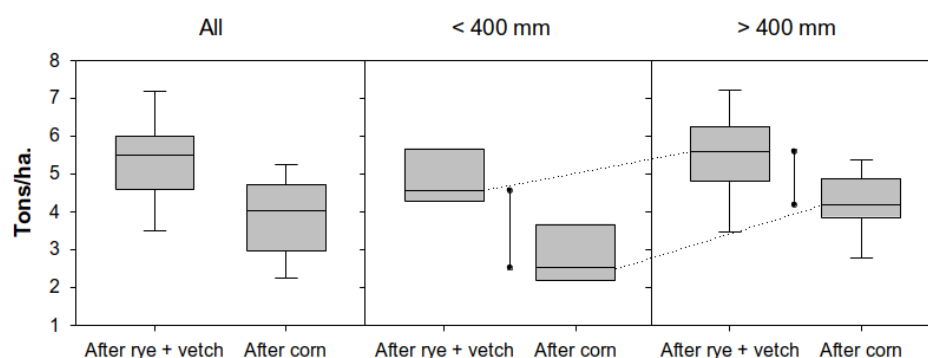


Figure 2.24: Distribution of wheat yields from the Selectia crop research site in Balti for two types of crop rotations: wheat after rye and vetch, and wheat after corn. The box plots cover the full period 1980–2020 (left panel) and subsets of the dry (≤ 400 mm) and humid (> 400 mm) years.

Yield differences between both crop management practices are higher in dry years, in which the wheat yields after corn rotation strongly decrease in comparison to normal and humid years. This is contrasted by wheat yields after rye vetch rotation showing a smaller decrease. This response during extreme dry conditions seems to be related to the availability of soil moisture and is clearly observed in the dry years of 2007, 2012 and 2020. Average crop yield in these three years was 76.8% for the wheat after rye and vetch in relation to the long-term mean, but only 59.1% for the average of wheat after corn.

The mixture of rye and vetch for green mass is harvested in June, but corn in September. Consequently, the consumption of soil moisture in the corn rotation is significantly higher which could explain the subsequent reduction of wheat yields. This is particularly critical during years characterized by low precipitation. Also water availability in the soil after harvesting is maintained better during dry years by wheat after rye and vetch since in the three extreme drought years the water storage in the soil was 40.0% relative to the soil moisture at the date of planting, but only 22.3% in the case of the wheat and corn rotation. This suggests that the rotation of wheat after rye and vetch optimises soil water saving and improves crop yields particularly in dry years.

2.4 Discussion and Conclusions

This study analysed observed long-term drought evolution and future drought projections for the Republic of Moldova with specific focus on crop yield impacts. Previous studies have shown the strong influence of climate variability and drought on crop yields in Moldova (Potop 2011; Potopová et al. 2020, 2016). Here we have found similar results which are strongly dependent on the crop type. While the severity of pluvial droughts (SPI) has decreased over the last 170 years, the impact of precipitation deficits on yields has increased in the last two decades. We associate this behavior with the strong warming trend observed in recent decades.

Precipitation trends in Moldova are coherent with other studies analyzing trends in precipitation deficits and pluvial droughts in the Mediterranean area and southeastern Europe that do not show trends associated with anthropogenic forcing but rather are dominated by natural variability (Jaagus et al. 2021; Vicente-Serrano et al. 2021b). Given this temporal pattern, it is not possible to associate stronger drought severity and impacts on crop yields to larger precipitation deficits. Thus, it could be considered that given the bioclimatic conditions of the Republic of Moldova, with annual average precipitation close to 600 mm, a strong reduction of precipitation as recorded in 2012 or 2019 (430 and 450 mm, respectively) would not cause a strong decrease of crop yields given current crop water requirements (Critchley et al. 1991).

However, the current climate in Moldova is not stationary. Air temperature shows a very strong increase, particularly for the last two decades and more intense than the pattern observed worldwide as a consequence of anthropogenic forcing (Gulev et al. 2021). According to our results, this strong and rapid increase in maximum temperature during summer has endangered the capacity of crops to cope with years characterized by extreme water deficits. This is supported by the fact that precipitation deficits recorded in some years in the last two decades, particularly in 2020, have not been sufficiently severe to explain the large decrease of crop yields. More severe pluvial drought events have been recorded since the 1950s but have not caused such a dramatic decline in crop yields as those recorded in the last two decades.

The first evident effect of temperature increases that we found is a reinforcement of the sensitivity of crop yields to precipitation variability. In the period between 1950 and 2000 the yield of annual crops (sunflower and maize) showed in general low sensitivity to interannual variations in annual precipitation. Nevertheless, the increase of temperature recorded in the last decades has caused a strong increase in atmospheric evaporative demand in Moldova (Potop et al. 2014), which is consistent with observations in other regions of Europe (Jaagus et al. 2021; Maček et al. 2018; Vicente-Serrano et al. 2014). This increase has two main effects; the first is related to the reinforcement of plant transpiration and direct soil evaporation. If precipitation is high and sufficient moisture is available

in the soil, it is not expected that plants are affected negatively over the short term (Vicente-Serrano et al. 2020). Thus, during periods of high evaporative demand, temperature and radiation are usually high, and if moisture is available in the soil, this usually reinforces photosynthesis and plant growth. However, during periods of precipitation deficits when leaf stomatal conductance is determined by soil water availability, and also during periods of very high temperatures, an increase in atmospheric demand reduces photosynthesis in response to higher VPD (Breshears et al. 2013; Grossiord et al. 2020; Sulman et al. 2016) and in addition, increases the risk of plant hydraulic failure as a consequence of xylem embolism (Anderegg et al. 2012; McDowell et al. 2019).

Moreover, even if precipitation deficits are modest, enhanced plant transpiration and soil evaporation in response to higher atmospheric evaporative demand reinforces soil moisture deficits (Teuling et al. 2013) and may also cause land atmospheric feedbacks that contribute to additional atmospheric drying by altering the partitioning between sensible and latent heat fluxes from the surface to the atmosphere (Seneviratne et al. 2010).

Plant physiology is also strongly affected by the increasing frequency and magnitude of extreme temperatures, particularly during summer, since they may contribute to the additional loss of water from leaves and damage the leaf tissues (Brodrribb et al. 2020). All these mechanisms caused by temperature rise that negatively affect plant development are consistent with the observations of crop yield and vegetation activity in Moldova, since temperature and atmospheric demand show strong negative correlations with these crop variables. It is therefore reasonable to consider that enhanced temperature has negatively affected crop yields in the region, which is also consistent with assessments by several studies that have observed a decline in the crop yield potential in response to global warming in other regions or at the global scale (Asseng et al. 2015; Lobell et al. 2011; Moore and Lobell 2015).

Projections by climate change models for the region are alarming for the agricultural sector. Precipitation projections do not suggest substantial changes at the end of the century, even for scenarios of high greenhouse gas concentrations, although all models show that precipitation will have an important interannual variability consistent with the behavior observed from historical observations. This is consistent with recent studies that show that this region of eastern Europe is not a hot-spot in relation to precipitation changes (Spinoni et al. 2020). Nevertheless, it is expected that the atmospheric conditions favorable to generate precipitation deficits, characterized by dominant atmospheric stability in eastern Europe, as observed in 2020, will be also recorded in the future as consequence of the natural climate variability (Enke et al. 2005; Terray et al. 2004; Zappa and Shepherd 2017).

The real problem is that climate change projections show with high confidence a strong temperature increase of more than 4 K in the Republic of Moldova at the end of the century. This increase is very consistent among the different models and particularly severe during the summer (Coppola et al. 2021a). Studies focusing on the projections of extreme temperature have also shown that the frequency and severity of heatwaves will increase in the future in this region of Europe (Coppola et al. 2021b). These projections suggest that during periods of precipitation deficits that are expected to be recorded in the future as a consequence of natural climate variability, the limitations for crop growth will increase even more.

Moreover, the stronger evaporation that is expected during normal or wet periods may reinforce soil moisture depletion not exclusively determined by precipitation deficits (Lansu et al. 2020; Liu et al. 2015; Teuling et al. 2013). Thus, the inclusion of atmospheric evaporative demand in the assessment of drought conditions for future scenarios shows a clear increase in the severity of droughts at the end of the twenty-first century in the Republic of Moldova, which is consistent with assessments in other regions of Europe based on metrics that consider atmospheric evaporative demand (Dai and Zhao 2017; Li et al. 2021; Naumann et al. 2018; Spinoni et al. 2018) or directly the land evapotranspiration (Samaniego et al. 2018).

Given the importance of the agricultural sector to the economy of Moldova and the serious constraints that global warming is causing on crop yields, it is urgent to advance development of adaptive agricultural management strategies. One possibility is to increase the importance of grapes in the crop sector. The quality of wines produced in Moldova is renowned (De Salvo et al. 2017; Geana et al. 2013; Pomerleau et al. 2008) and this could be a relevant sector to strengthen agricultural activity and eco-tourism.

In this study we have observed that annual grape production in the last seven decades was insensitive to precipitation variability. Grapes are cultivated in other regions of the world characterized by much more limiting climate conditions than those recorded in Moldova, e.g., different Mediterranean climate regions (Ramos 2006; Ramos et al. 2008; Ramos and Martínez-Casasnovas 2010). Vineyards show high adaptability to summer dryness as developed root systems allow water to be obtained from deeper layers (Smart et al. 2006). This means that although climate may evolve to more arid conditions in Moldova, vineyards may adapt well to less available water and warmer conditions. Although increased temperatures may enhance the sugar concentration of the fruits and the resulting wine, e.g. increasing the degree of alcohol or sweetness, this would not affect the production very much as the wine produced in much more arid regions usually shows very high quality (Abril et al. 2005; Fragoso et al. 2011).

There are other possibilities for crop adaptation in the region. The development of more sustainable agricultural management practices based

on crop rotation to maintain the quality and carbon content of the soil is one of the main strategies to promote adaptation to climate change (Boincean and Lal 2014; Lal 2004). In this study we used crop yield data from a long-term experiment developed in the Selectia crop research institute in Bălți in which rotation management practices were compared. We have shown that management characterized by intensive crop cultivations with rotations of summer maize and winter wheat generates lower wheat yields on average, accentuated during years of precipitation deficits. On the contrary, including early harvested predecessors in the rotation reduces vulnerability of the wheat crop yields to drought.

This can be explained by two factors; first is that maize is harvested later than the mixture of spring vetch and spring oats for green mass, which means more consumption of water from deeper soil layers. In the rich soils of the Moldovan steppe, under drought conditions, the water stored in deeper layers (1–2 metres) plays a more important role than in normal and humid years (Boincean 2012; Boincean and Lal 2014), and the depletion of this layer by the intensive summer maize crops reduces the availability of water for the subsequent winter cereals. Second, winter rye in crop rotations increases carbon accumulation and the capacity of soils to store water (Lal 2008, 2004), which is crucial under drought conditions. Unfortunately in Moldova, winter wheat is sown mainly after late harvested predecessors as maize for grain and sunflower, which could be unsustainable under conditions of more severe droughts.

In summary, we have shown that the vulnerability of crop yields to precipitation variability has noticeably increased during the last twenty years due to the large temperature increase recorded in the region. Climate change projections show a reinforcement of limiting climate conditions for adequate crop yield. For this reason, it is necessary to promote moisture-preserving land management practices, characterized by perennial spring crops and winter cereals to increase the stock of soil moisture and also consider extending the area covered by vineyards that may adapt to more arid and warmer climate conditions, maintaining productivity and grape quality.

3 Data and studies of the Boyne (IE) and Upper Aragón (ES) river basins relevant for future research

by Tobias Conradt

Due to the higher-than-expected workload caused by the preparation of the scenario studies in Germany and the Republic of Moldova presented above and hampering difficulties in alternative regional set-ups of the eco-hydrological model SWIM, no original CROSSDRO scenario modelling can be presented for the other case study basins, namely the Boyne River catchment in Ireland and the Upper Aragón basin in North-Eastern Spain.

We therefore account for these regions by pointing out data sources of interest for scenario modelling and mini-reviews of the recent literature to provide at least the starting basis for future regional scenario studies. Internet links to data sources are not cited in the References but given in footnotes; this might be more convenient when pulling together the actual data to be used in a scenario modelling project. All of these Internet links have been checked for functionality in February 2023.

3.1 Boyne River catchment, Ireland

3.1.1 Location and data resources

The Boyne River discharges towards Ireland's east coast reaching the Irish Sea at 53°43'18"N, 6°14'20"W, just downstream the town of Drogheda, approximately 55 km north of Dublin. The catchment extends over an area of 2694 km² and its highest point near Bailieborough in the north has an elevation of 339 m amsl. Viable bounding boxes for geographical data collection and basin mapping are 7°35'W–6°10'W, 53°10'N–54°10'N, or, in the Irish National Grid, eastings of 230,000–330,000 m and northings of 220,000–320,000 m.

Catchment and subcatchment boundaries officially delineated for the reporting framework of the Water Framework Directive can be obtained through the geoportal of the Irish Environmental Protection Agency¹. This link also provides access to electronic land use and soil maps regularly needed for hydrological modelling. There is also a map viewer for these and further thematic maps, e.g. showing the locations, IDs, and names of hydrometric gauging stations².

Vector maps of numerous general topographic features are available via the open data portal of the Ordnance Survey of Ireland³. Unfortunately, there is no authoritative DEM freely available. However, as long as horizontal resolutions of 1 arc second or 30 m are sufficient, the best

1 <https://gis.epa.ie/GetData/Download>

2 <https://gis.epa.ie/EPAMaps>

3 <https://data-osi.opendata.arcgis.com>

alternative may currently be TessaDEM⁴ whose v1.1 release from February 2023 is based on MERIT and the Japanese AW3D30 elevation data set.

Weather data is published by Met Éireann, the Irish weather service. Station measurements can be searched and displayed through an interactive website⁵, but for systematic data processing bulk downloads may be more practical. There is a CSV file from which the relevant stations may be selected⁶, and a link for station file download⁷; with these the download process can be semi-automatized by a bash loop using wget. Alternatively, Met Éireann provides a reanalysis product covering the years 1981–2018 with 2.5 km horizontal resolution (MÉRA)⁸.

In case the original observations are preferred the user should be aware of Dublin Airport and Casement being the only stations in some proximity to the basin (to the south-east) with a long history of multi-variable recordings. More closely located are Mullingar in the west, Ballyhaise in the north-west, and Dunsany in the east; they went into operation however not before 2002, 2003, and 2006, respectively. There are at least several stations with long records of daily maximum and minimum temperatures in addition to precipitation. Candidates for backward-extensions of meteorological time series by proxy-relations (e.g. daily temperature ranges for radiation) are Cavan (Drumconnick, closed in 2019) approximately 10 km south-west of Ballyhaise, Warrenstown near Dunsany (operation ceased in 2015), and Derrygreenagh roughly 20 km south of Mullingar. If reliable proxy-relationships can be found, better coverage can be obtained using also the temperature and precipitation records of Carrickmacross^{82–99} (Dunoge), Ardee (Boharnamoe, closed in 2020), Navan (Tara Mines, closed in 2014), and Edenderry (Ballinla). In addition to these, there may be another dozen precipitation-only stations still active or with long records not to be neglected when interpolating the historical meteorological canvas.

Runoff data can be obtained from the Office of Public Works' website⁹; note that the Boyne River catchment belongs to the Eastern River Basin District. Slane Castle (07012) is the quasi-outlet gauge station (catchment area 2408 km², representing 89.4 % of the Boyne area) with nearly 70 years of runoff measurements. Other stations with long time series suitable for model calibration are Liscarton (07010) at the Kells Blackwater, the biggest tributary to the Boyne River, and Navan Weir (07009) at the Boyne River, both stations positioned just upstream the river junction in Navan. The Moynalty branch of the Kells Blackwater system is gauged at Fyanstown (07006), and there are two gauges for upper tributaries to the Boyne River, Tremblestown (07001) at the Athboy River and Killyon (07002) at the Deel

⁴ <https://tessadem.com>

⁵ <https://www.met.ie/climate/available-data/historical-data>

⁶ https://cli.fusio.net/cli/climate_data/webdataac/StationDetails.csv

⁷ http://cli.fusio.net/cli/climate_data/webdata/dly375.csv

– The 375 in the link must be replaced by the station number.

⁸ <https://www.met.ie/climate/available-data/mera>

⁹ <https://waterlevel.ie/hydro-data/>

River. Finally, Trim (07005) gauges the Boyne River runoff upstream the Navan Weir station, but already including the upper tributaries.

Grass production is the most interesting variable for validating simulated plant growth in Ireland. The probably most informative data base is PastureBase Ireland driven by Teagasc¹⁰. It is meant as decision support tool for farmers and collects their field observations. Access is provided on request only, but as yield curves of former years with daily resolution¹¹ and mapped observations have been published (O’Leary et al. 2017), it may be worthwhile to ask for sign-up. Crop yields are reported by the Central Statistics Office of Ireland, but only as national aggregates. Annual values for NUTS-2 regions, including IE06 “Eastern and Midland” surrounding the Boyne River basin, can be obtained from Eurostat’s data base table “Crop production in EU standard humidity by NUTS 2 regions” (apro_cpshr)¹².

Climate scenario data downscaled specifically for Ireland is produced at the Irish Centre for High-End Computing (ICHEC) under the auspices of the Environmental Protection Agency. Currently there are products at 3.8 and 4.0 km resolution (Nolan and Flanagan 2020), and new versions can be expected in the CMIP6 framework (for the global modelling, see Nolan and McKinstry 2020). The data can be accessed via the ICHEC ESGF node¹³ after registration. The United Kingdom Climate Projections (UKCP) of the British Met Office¹⁴ are a further regional source to be considered despite their high-resolution products (2.2 km grid spacing) seem to be restricted to the UK. There are also medium-resolution (12 km) realisations for all of Europe. A convenient access point is the CEDA Archive¹⁵.

3.1.2 Existing eco-hydrological scenario studies

O’Driscoll et al. (2018) seems to be the only scenario study explicitly for the Boyne catchment in which a hydrological model (PERSiST) was driven by regional climate scenario data. These consisted of three realizations each from RCP 4.5 and 8.5 scenarios generated by two model chains, i.e. 12 future realizations in total. The study aimed at projections of dissolved organic matter in surface waters whose concentrations are likely to increase while runoff, according to this study, will decrease by up to 30% in all months of the year. There are scenario studies of other regions of Ireland, namely for the city of Dublin (Willuweit et al. 2016) and for a karst area in Western Ireland (Morrissey et al. 2021), which projected increasing runoff in winter or even higher flood risks, results which question the findings of O’Driscoll et al. Also a recent study utilizing CMIP6 outputs for 37 catchments across Ireland (Meresa et al. 2022) found no dominant trend, albeit tendencies towards drier summers and wetter winters. This calls for further eco-hydrological scenario studies in the region.

10 <https://www.teagasc.ie/crops/grassland/pasturebase-ireland/>

11 <https://www.teagasc.ie/crops/grassland/pasturebase-ireland/grass-curve/>

12 https://ec.europa.eu/eurostat/databrowser/view/apro_cpshr/default/table?lang=en

13 <https://esgf.ichec.ie/projects/esgf-ichec/>

14 <https://www.metoffice.gov.uk/research/approach/collaboration/ukcp>

15 <https://catalogue.ceda.ac.uk/?q=ukcp>

3.2 Upper Aragón River basin, Spain

3.2.1 Location and data resources

The Aragón River originates at the crest of the Pyrenees at the Spanish–French border. Its upper section ends by passing a little mountain range at 42°36'37"N, 1°13'08"W; this is about 2 km south-west of the town of Yesa as the crow flies and about 4.5 km downstream the Yesa Reservoir dam as the water flows. Halfway between this point and the dam there is a gauging station named P.P. Yesa with a catchment area of 2191 km². Surface elevations range from 420 m amsl to 2883 m amsl marked by the top of the Peña Collarada located 11 km south of the river origin. The catchment can be mapped and modelled in bounding boxes of 1°20'W–0°15'W, 42°20'N–43°05'N or, in UTM coordinates in zone 30T of E 640,000–720,000, N 4,700,000–4,770,000.

Lots of authoritative geodata can be browsed through a map viewer of the Spanish Government¹⁶. The catchment boundary can be aggregated from vector polygons of the authoritative subcatchment map produced for the EU Water Framework Directive named "*Subcuencas de las masas de agua superficiales de la DMA (artículo 5)*" available from the Ministry for Ecological Transition and the Demographic Challenge (MITECO)¹⁷. While this map also contains the small parts of the basin on French territory (the national boundary follows the watershed not always exactly), it has to be kept in mind that other thematic maps have to be extended by transnational resources, e.g. Copernicus products¹⁸ like the Corine land cover maps.

A central download platform for Spanish geodata is the *Centro de Descargas*¹⁹, and an alternative is offered by the Inspire geoportal of the European Union²⁰. From the *Centro*'s start page high-resolution elevation data can be found below "*Modelos Digitales de Elevaciones*", and thematic maps reside under "*Información geográfica temática*". Among the latter, SIOSE (*Sistema de Información de Ocupación del Suelo en España*), the most recent version being SIOSE AR, provide high-resolution land use maps. There are also the thematic maps of the National Atlas of Spain (*Mapas temáticos del ANE*) among which soil maps can be found (*España. Suelos*. 2006). Inspire also gives acces to a forest map "*Mapa Forestal de España de máxima actualidad*", and a hydrogeological map "*Mapa Hidrogeológico a escala 1:200.000 digital continuo de España*". Locations of meteorological stations are captured in "*Estaciones Climatológicas de la Agencia Estatal de Meteorología*". For visualization purposes, the base map products of the *Instituto Geográfico Nacional* may be of interest, these are

16 <https://sig.mapama.gob.es/geoportal/>

17 <https://www.miteco.gob.es/es/cartografia-y-sig/ide/descargas/agua/cuencas-y-subcuencas.aspx>

18 <https://land.copernicus.eu/>

19 <https://centrodedescargas.cnig.es/CentroDescargas/index.jsp>

20 <https://inspire-geoportal.ec.europa.eu/results.html?country=es>

distributed via the *Centro de Descargas*, see under “*Mapas vectoriales y Bases Cartográficas y Topográficas*”.

Weather data of the *Agencia Estatal de Meteorología* (AEM) can be accessed in their entirety after registration, by which the user is provided an API key.²¹ For identifying the relevant stations a shapefile is provided also here, and for selecting the stations from a list it might be useful to know that the Upper Aragón basin is split between the provinces of Navarra, Zaragoza, and Huesca. Unfortunately, there are no readily interpolated grid products.

River runoff data and storage volumes in reservoirs are collected and published in form of annual bulletins by the *Confederación Hidrográfica del Ebro*²²; nowadays the measurements are collected by the *Sistema Automático de Información Hidrológica* (SAIH)²³, individual downloads from SAIH however require registration²⁴. Shapefiles of gauge locations can be downloaded from a MITECO website²⁵. Finally, the ministry maintains a general website about Spanish water governance²⁶.

The Spanish Ministry for Agriculture, Fisheries and Food pursues an annual assessment of crop areas and yields, *Encuesta sobre Superficies y Rendimientos Cultivos* (ESYRCE)²⁷, whose final results on province level are published in yearbooks called *Anuario Estadística*²⁸. Issues since 1904 are online available – a long and detailed record of regional plant growth. The history of irrigation has probably also to be considered in this context, and there is at least some recent years of regional data available the national statistics institute, Instituto Nacional de Estadística. These can be accessed via *Estadísticas territoriales, Agricultura y medio ambiente*²⁹ by clicking on “*Uso del agua en la agricultura*”.

AEM offers two kinds of daily climate scenario data for Spain³⁰: station data statistically downscaled from global dynamical models, and the output of global–regional dynamical climate model chains generated in the ENSEMBLES project. The former have the advantage that the systematical error of the user’s interpolation of past station observations (which is required as there are no gridded observational products, see above) can be consistently reproduced, but the local errors of the underlying global models are probably large. Furthermore, both AEM scenario packages are

21 <https://opendata.aemet.es/centrodedescargas/inicio>

22 <https://www.chebro.es/web/guest/datos-historicos>

23 <http://www.saihebro.com/saihebro/index.php>

24 <http://www.saihebro.com/saihebro/index.php?url=/autoservicio/inicio>

25 <https://www.miteco.gob.es/es/cartografia-y-sig/ide/descargas/agua/saih.aspx>

26 <https://www.miteco.gob.es/es/agua/temas/default.aspx>

27 <https://www.mapa.gob.es/es/estadistica/temas/estadisticas-agrarias/agricultura/esyrce/>

28 <https://www.mapa.gob.es/es/estadistica/temas/publicaciones/anuario-de-estadistica/default.aspx>

29 <https://www.ine.es/dynInfo/Infografia/Territoriales/galeriaCapitulo.html?capitulo=4332>

30 https://www.aemet.es/en/serviciosclimaticos/cambio_climat/datos_diarios

lagging behind the present state of climate modelling; the most recent data considered in the statistical downscaling have been generated before 2014 and are CMIP5-based, while ENSEMBLES, finalized already in 2009, still relied on CMIP3 results. This leaves the statistically downscaled station data as the only AEM product to be potentially considered in eco-hydrological scenario modelling. It is however advisable to watch out for present-state data downscaled from CMIP6 models, e.g. within the EURO-CORDEX framework³¹.

3.2.2 Existing eco-hydrological scenario studies

Probably the first hydrological scenario study for the complete Upper Aragón basin was presented by López-Moreno et al. (2014) and projected decreases in streamflow caused not only by climate change but also by the already initiated forest regeneration. The climate scenario used in this study was still from CMIP3 generation models. Following a preparative study on water demand scenarios under climate change (Grouillet et al. 2015), Fabre et al. (2016) delivered a scenario assessment for the complete Ebro river basin comparing it to the Herault basin in Southern France. Jorda-Capdevila et al. (2019) and Sordo-Ward (2019) followed their footsteps, also comparing the Ebro scenarios to those of other mediterranean basins. The common outcome of all these studies are expectations of more water scarcity and increasing drought stress, but there is also hope that intelligent water management can largely protect societal development in the Ebro region (Sordo-Ward 2019).

Three recent scenario studies focusing on other subcatchments of the Ebro basin should also be mentioned: Herrero et al. (2017; Noguera Pallaresa basin, located also at the Pyrenees but close to the Mediterranean), Haro-Monteagudo (2020; Gállego–Cinca river system, the eastward neighbour of the Aragón catchment), and Lastrada et al. (2020; Híjar river system, the north-western corner of the Ebro basin in the Cantabrian Mountains). While Herrero et al. (2017) were interested in sediment yields and found increases, probably caused by more concentrated rainfall events, Haro-Monteagudo (2020) observed the pattern of drier summer and wetter winter seasons, and the results of Lastrada et al. (2020) depended strongly on the choice of the climate scenario. Thus, a reassessment of López-Moreno et al. (2014) using the most recent available data would definitely be advisable for obtaining more clarity about the future challenges in the Upper Aragón basin, and we deeply regret that it was not possible to achieve this already within the CROSSDRO project.

31 https://wcrp-cordex.github.io/simulation-status/CORDEX_CMIP6_status.html#EUR-11

References

- Abril M, Negueruela AI, Pérez C, Juan T, Estopañán G (2005) Preliminary study of resveratrol content in Aragón red and rosé wines. *Food Chem* 92: 729–736. <https://doi.org/10.1016/j.foodchem.2004.08.034>
- Allen R, Pereira L, Raes D, Smith M (1998) Crop evapotranspiration: Guidelines for computing crop water requirements. FAO Irrigation and drainage paper 56. Food and Agriculture Organization of the United Nations, Rome. ISBN 92-5-104219-5. <https://www.fao.org/3/x0490e/x0490e00.htm> – Last accessed in February 2023.
- Anderegg WRL, Berry JA, Smith DD, Sperry JS, Anderegg LDL, Field CB (2012) The roles of hydraulic and carbon stress in a widespread climate-induced forest die-off. *PNAS* 109:233–237. <https://doi.org/10.1073/pnas.1107891109>
- Asseng S, Ewert F, Martre P, Rötter RP, Lobell DB et al. (2015) Rising temperatures reduce global wheat production. *Nat Clim Change* 5:143–147. <https://doi.org/10.1038/nclimate2470>
- Ayarzagüena B, Barriopedro D, Garrido-Perez JM, Abalos M, de la Cámara A et al. (2018) Stratospheric Connection to the Abrupt End of the 2016/2017 Iberian Drought. *Geophys Res Lett* 45(22):12,639–12,646. <https://doi.org/10.1029/2018GL079802>
- Beguiría S, Vicente-Serrano SM, Reig F, Latorre B (2014) Standardized precipitation evapotranspiration index (SPEI) revisited: parameter fitting, evapotranspiration models, tools, datasets and drought monitoring. *Int J Climatol* 34(10):3001–3023 <https://doi.org/10.1002/joc.3887>
- BfG (2020) Catchment-DE. Geodata of drainage and river basins provided by the German Federal Institute for Hydrology, © WasserBLICK/BfG & Zuständige Behörden der Länder, 2020. <https://geoportal.bafg.de/inspire/download/HY/catchment/datasetfeed.xml> – Accessed in November 2020
- BGR (2014) Ackerbauliches Ertragspotential der Böden in Deutschland 1:1.000.000. Map in multiple electronic formats. Bundesanstalt für Geowissenschaften und Rohstoffe (BGR), Hannover. https://www.bgr.bund.de/DE/Themen/Boden/Ressourcenbewertung/Ertragspotential/Ertragspotential_node.html – Last accessed in October 2022.
- BMEL (2019) Erntebericht 2018 – Mengen und Preise. Bundesministerium für Ernährung und Landwirtschaft, Berlin, 28+10 pp. https://www.bmel.de/SharedDocs/Downloads/DE/_Landwirtschaft/Pflanzenbau/Ernte-Bericht/ernte-2018.pdf – Last accessed in February 2023.
- Boincean B (2012) Soil fertility and nitrogen fertilization in the modern sustainable farming systems of Moldova. In: Adewuyi B, Chukwu K (eds) *Soil Fertility: Characteristics, Processes and Management*, pp 91–121. Hauppauge, NY. ISBN 978-1-62081-087-3.
- Boincean B, Dent D (2019) Farming the Black Earth: Sustainable and Climate-Smart Management of Chernozem Soils. Cham, xxvii+226 pp. ISBN 978-3-030-22535-3 (softcover) 978-3-030-22533-9 (eBook). <https://doi.org/10.1007/978-3-030-22533-9>
- Boincean B, Lal R (2014) Conservation agriculture on chernozems in the republic of Moldova. In: Lal R, Stewart BA (eds) *Soil Management of Smallholder Agriculture*, pp 203–222. Boca Raton, FL. ISBN 978-0-429169854 (eBook). <https://doi.org/10.1201/b17747>
- Breshears DD, Adams HD, Eamus D, McDowell NG, Law DJ, Will RE, Williams AP, Zou CB (2013) The critical amplifying role of increasing atmospheric moisture demand on tree

- mortality and associated regional die-off. *Front Plant Sci* 4:266. <https://doi.org/10.3389/fpls.2013.00266>
- Brodribb TJ, Powers J, Cochard H, Choat B (2020) Hanging by a thread? Forests and drought. *Science* 368(6488):261–266. <https://doi.org/10.1126/science.aat7631>
- Bucheli J, Dalhaus T, Finger R (2022) Temperature effects on crop yields in heat index insurance. *Food Policy* 107:102214. <https://doi.org/10.1016/j.foodpol.2021.102214>
- Chen M, Xie P, Janowiak JE (2002) Global land precipitation: A 50-yr monthly analysis based on gauge observations. *J Hydrometeorol* 3(3):249–266. [https://doi.org/10.1175/1525-7541\(2002\)003<0249:GLPAYM>2.0.CO;2](https://doi.org/10.1175/1525-7541(2002)003<0249:GLPAYM>2.0.CO;2)
- Conley MM, Kimball BA, Brooks TJ, Pinter Jr PJ, Hunsaker DJ et al. (2001) CO₂ enrichment increases water-use efficiency in sorghum. *New Phytol* 151(2):407–412. <https://doi.org/10.1046/j.1469-8137.2001.00184.x>
- Conradt T, Koch H, Hattermann FF, Wechsung F (2012) Spatially differentiated management-revised discharge scenarios for an integrated analysis of multi-realisation climate and land use scenarios for the Elbe River basin. *Regional Environmental Change*, 12(3):633–648. <https://doi.org/10.1007/s10113-012-0279-4>
- Conradt T (2022) Choosing multiple linear regressions for weather-based crop yield prediction with ABSOLUT v1.2 applied to the districts of Germany. *International Journal of Biometeorology* 66:2287–2300. <https://doi.org/10.1007/s00484-022-02356-5>
- Conradt T, Engelhardt H, Menz C, Vicente-Serrano SM, Alvarez Farizo B et al. (2023) Cross-sectoral impacts of the 2018–2019 Central European drought and climate resilience in the German part of the Elbe River basin. *Regional Environmental Change* 23 (Article number 32, in press). <https://doi.org/10.1007/s10113-023-02032-3>
- Copernicus (2016) European Digital Elevation Model (EU-DEM), version 1.1. Copernicus Land Monitoring Service, part of the European Earth monitoring programme (GMES). <https://land.copernicus.eu/imagery-in-situ/eu-dem/eu-dem-v1.1> – Last accessed in December 2022.
- Copernicus (2020) CORINE Land Cover (CLC) 2018, version v.2020_20u1. Copernicus Land Monitoring Service, part of the European Earth monitoring programme (GMES). <https://land.copernicus.eu/pan-european/corine-land-cover/clc2018> – Accessed in March 2021.
- Coppola E, Nogherotto R, Ciarlo’ JM, Giorgi F, van Meijgaard E et al. (2021a) Assessment of the European Climate Projections as Simulated by the Large EURO-CORDEX Regional and Global Climate Model Ensemble. *J Geophys Res Atmos* 126(4):e2019JD032356. <https://doi.org/10.1029/2019JD032356>
- Coppola E, Raffaele F, Giorgi F, Giuliani G, Xuejie G et al. (2021b) Climate hazard indices projections based on CORDEX-CORE, CMIP5 and CMIP6 ensemble. *Clim Dyn* 57:1293–1383. <https://doi.org/10.1007/s00382-021-05640-z>
- Cornes RC, van der Schrier G, van den Besselaar EJM, Jones PD (2018) An Ensemble Version of the E-OBS Temperature and Precipitation Data Sets. *Journal of Geophysical Research: Atmospheres* 123(17):9391–9409. <https://doi.org/10.1029/2017JD028200>
- Critchley W, Siegert K, Finkel M (1991) A Manual for the Design and Construction of Water Harvesting Schemes for Plant Production. Series: Water harvesting (AGL/MISC/17/91). Food and Agricultural Organization of the United Nations, Rome. <https://www.fao.org/3/U3160E/u3160e00.htm> – Last accessed in February 2023.

- Dai A, Zhao T (2017) Uncertainties in historical changes and future projections of drought. Part I: estimates of historical drought changes. *Clim Change* 144:519–533. <https://doi.org/10.1007/s10584-016-1705-2>
- De Kauwe MG, Medlyn BE, Tissue DT (2021) To what extent can rising [CO₂] ameliorate plant drought stress? *New Phytol* 231(6):2118–2124. <https://doi.org/https://doi.org/10.1111/nph.17540>
- De Salvo M, Begalli D, Capitello R, Agnoli L, Tabouratzi E (2017) Determinants of winegrowers' profitability: evidence from an Eastern Europe wine region. *EuroMed J Business* 12(3):300–315. <https://doi.org/10.1108/EMJB-12-2016-0043>
- Deryng D, Conway D, Ramankutty N, Price J, Warren R (2014) Global crop yield response to extreme heat stress under multiple climate change futures. *Environmental Research Letters* 9(3):034011. <https://doi.org/10.1088/1748-9326/9/3/034011>
- Deshaies, M. (2017) The new post-mining energy landscapes in the lignite basin of Lower Lusatia (Germany). *Europa Regional* 25(3–4):29–41. <https://nbn-resolving.org/urn:nbn:de:0168-ssoar-62253-4>
- DESTATIS (2012ff) Wachstum und Ernte – Feldfrüchte. Fachserie / report series. Statistisches Bundesamt, Wiesbaden. https://www.statistischebibliothek.de/mir/receive/DESerie_mods_00000335 – Last accessed in January 2022.
- DESTATIS (2021a) Bodennutzung der Betriebe (Struktur der Bodennutzung). Statistisches Bundesamt, Wiesbaden, 228 pp. <https://www.destatis.de/DE/Themen/Branchen-Unternehmen/Landwirtschaft-Forstwirtschaft-Fischerei/Publikationen/Bodennutzung/bodennutzung-2030212217004.pdf> – Last accessed in November 2022.
- DESTATIS (2021b) Städte (Alle Gemeinden mit Stadtrecht) nach Fläche, Bevölkerung und Bevölkerungsdichte am 31.12.2020. Excel file, 258 kB. Statistisches Bundesamt, Wiesbaden. <https://www.destatis.de/DE/Themen/Laender-Regionen/Regionales/Gemeindeverzeichnis/Administrativ/05-staedte.html> – Accessed in September 2022.
- Durre I, Wallace JM, Lettenmaier DP (2000) Dependence of extreme daily maximum temperatures on antecedent soil moisture in the contiguous United States during summer. *J Clim* 13(14):2641–2651. [https://doi.org/10.1175/1520-0442\(2000\)013<2641:DOEDMT>2.0.CO;2](https://doi.org/10.1175/1520-0442(2000)013<2641:DOEDMT>2.0.CO;2)
- DWD (2022) Climatological maps of Germany. PNG graphics. <https://www.dwd.de/EN/ourservices/klimakartendeutschland/klimakartendeutschland.html> – Last accessed in September 2022.
- DWD-CDC (2022a) Grids of monthly averaged daily air temperature (2m) over Germany, version v1.0. ASCII files. Deutscher Wetterdienst, Wiesbaden. https://opendata.dwd.de/climate_environment/CDC/grids_germany/monthly/air_temperature_mean/ – Last accessed in October 2022.
- DWD-CDC (2022b) Grids of monthly total precipitation over Germany, version v1.0. ASCII files. Deutscher Wetterdienst, Wiesbaden. https://opendata.dwd.de/climate_environment/CDC/grids_germany/monthly/precipitation/ – Last accessed in October 2022.
- DWD-CDC (2022c) Historical daily station observations (temperature, pressure, precipitation, sunshine duration, etc.) for Germany. Deutscher Wetterdienst, Wiesbaden. https://opendata.dwd.de/climate_environment/CDC/observations_germany/climate/daily/kl/ – Last accessed in October 2022.

- Enke W, Deutschländer T, Schneider F, Küchler W (2005) Results of five regional climate studies applying a weather pattern based downscaling method to ECHAM4 climate simulations. *Meteorol Z* 14:247–257. <https://doi.org/10.1127/0941-2948/2005/0028>
- Eurogeographics (2020) EuroGlobalMap. 1:1 million scale topographic dataset, Version 2020. EuroGeographics, Brussels. <https://eurogeographics.org/maps-for-europe/open-data/> – Accessed in October 2020, current version available via <https://www.mapsforeurope.org/datasets/euro-global-map>
- Fabre J, Ruelland D, Dezetter A, Grouillet B (2016) Sustainability of water uses in managed hydrosystems: human- and climate-induced changes for the mid-21st century. *Hydrol Earth Syst Sci* 20(8):3129–3147. <https://doi.org/10.5194/hess-20-3129-2016>
- FGG Elbe (2021) Zweite Aktualisierung des Bewirtschaftungsplans nach § 83 WHG bzw. Artikel 13 der Richtlinie 2000/60/EG für den deutschen Teil der Flussgebietseinheit Elbe für den Zeitraum von 2022 bis 2027. Flussgebietsgemeinschaft Elbe, Magdeburg, 338 pp. <https://www.fgg-elbe.de/berichte/aktualisierung-nach-art-13-2021.html> – Last accessed in February 2023.
- Fontana G, Toreti A, Ceglar A, De Sanctis, G., 2015. Early heat waves over Italy and their impacts on durum wheat yields. *Nat Hazards Earth Syst Sci* 15(7):1631–1637. <https://doi.org/10.5194/nhess-15-1631-2015>
- Fragoso S, Aceña L, Guasch J, Mestres M, Busto O (2011) Quantification of phenolic compounds during red winemaking using FT-MIR spectroscopy and PLS-regression. *J Agric Food Chem* 59(20):10795–10802. <https://doi.org/10.1021/jf201973e>
- Garrido-Perez JM, Ordóñez C, Barriopedro D, García-Herrera R, Paredes D (2020) Impact of weather regimes on wind power variability in western Europe. *Appl Energy* 264:114731. <https://doi.org/https://doi.org/10.1016/j.apenergy.2020.114731>
- Geana I, Iordache A, Ionete R, Marinescu A, Ranca A, Culea M (2013) Geographical origin identification of Romanian wines by ICP-MS elemental analysis. *Food Chem* 138:1125–1134. <https://doi.org/10.1016/j.foodchem.2012.11.104>
- Gräler B, Pebesma E, Heuvelink G. (2016) Spatio-Temporal Interpolation using gstat. *The R Journal* 8(1):204. <https://doi.org/10.32614/RJ-2016-014>
- Grinsted A, Moore JC, Jevrejeva S (2004) Application of the cross wavelet transform and wavelet coherence to geophysical time series. *Nonlinear Proc Geophys* 11:561–566. <https://doi.org/10.5194/npg-11-561-2004>
- Grossiord C, Buckley TN, Cernusak LA, Novick KA, Poulter B et al. (2020) Plant responses to rising vapor pressure deficit. *New Phytol* 226:1550–1566. <https://doi.org/10.1111/nph.16485>
- Grouillet B, Fabre J, Ruelland D, Dezetter A (2015) Historical reconstruction and 2050 projections of water demand under anthropogenic and climate changes in two contrasted Mediterranean catchments. *J Hydrol* 522:684–696. <https://doi.org/10.1016/j.jhydrol.2015.01.029>
- Gulev SK, Thorne PW, Ahn J, Dentener FJ, Domingues CM et al. (2021) Changing State of the Climate System. In: MassonDelmotte V, Zhai P, Pirani A, Connors SL, Péan C et al. (eds) *Climate Change 2021: The Physical Science Basis. Contribution of Working Group I to the Sixth Assessment Report of the Intergovernmental Panel on Climate Change*. Cambridge and New York, pp 287–422. <https://www.ipcc.ch/report/ar6/wg1/chapter/chapter-2/> – Last accessed in February 2023.

- Gutowski JW, Giorgi F, Timbal B, Frigon A, Jacob D et al. (2016) WCRP COordinated Regional Downscaling EXperiment (CORDEX): A diagnostic MIP for CMIP6. *Geosci Model Dev* 9:4087–4095. <https://doi.org/10.5194/gmd-9-4087-2016>
- Hargreaves GH, Samani ZA (1985) Reference crop evapotranspiration from temperature. *Applied Engineering in Agriculture* 1(2):96–99. <https://doi.org/10.13031/2013.26773>
- Hari V, Rakovec O, Markonis Y, Hanel M, Kumar R (2020) Increased future occurrences of the exceptional 2018–2019 Central European drought under global warming. *Scientific Reports* 10(1):12207. <https://doi.org/10.1038/s41598-020-68872-9>
- Haro-Monteagudo D, Palazón L, Beguería S (2020) Long-term sustainability of large water resource systems under climate change: A cascade modeling approach. *J Hydrol* 582:124546. <https://doi.org/10.1016/j.jhydrol.2020.124546>
- Hennings V, Höper H, Mueller L (2016) Small-scale soil functional mapping of crop yield potentials in Germany. In: Mueller L, Sheudshen A, Eulenstein F (eds) *Novel methods for monitoring and managing land and water resources in Siberia*. Springer, Cham, pp. 597–617. https://doi.org/10.1007/978-3-319-24409-9_27
- Hernandez-Barrera S, Rodriguez-Puebla C, Challinor AJ (2017) Effects of diurnal temperature range and drought on wheat yield in Spain. *Theor Appl Climatol* 129:503–519. <https://doi.org/10.1007/s00704-016-1779-9>
- Herrero A, Buendia C, Bussi G, Sabater S, Vericat D et al. (2017) Modeling the sedimentary response of a large Pyrenean basin to global change. *J Soil Sediment* 17(11):2677–2690. <https://doi.org/10.1007/s11368-017-1684-6>
- Hersbach H, Bell B, Berrisford P, Hirahara S, Horányi A et al. (2020) The ERA5 global reanalysis. *Q J R Meteorol Soc* 146(730):1999–2049. <https://doi.org/10.1002/qj.3803>
- Hlavinka P, Trnka M, Semerádová D, Dubrovský M, Žalud Z, Možný M (2009) Effect of drought on yield variability of key crops in Czech Republic. *Agric For Meteorol* 149:431–442. <https://doi.org/10.1016/j.agrformet.2008.09.004>
- Huete A, Didan K, Miura T, Rodriguez EP, Gao X, Ferreira LG (2002) Overview of the radiometric and biophysical performance of the MODIS vegetation indices. *Remote Sens Environ* 83:195–213. [https://doi.org/10.1016/S0034-4257\(02\)00096-2](https://doi.org/10.1016/S0034-4257(02)00096-2)
- IPCC (2014) *Climate change 2014: Synthesis Report. Contribution of Working Groups I, II and III to the Fifth Assessment Report of the Intergovernmental Panel on Climate Change* [Core Writing Team, Pachauri RK, Meyer LA (eds)]. Intergovernmental Panel on Climate Change, Geneva, 151 pp. <https://www.ipcc.ch/report/ar5/syr/> – Last accessed in February 2023.
- Jaagus J, Aasa A, Aniskevich S, Boincean B, Bojariu R et al. (2021) Long-term changes in drought indices in eastern and central Europe. *Int J Climatol* 42(1):225–249. <https://doi.org/10.1002/joc.7241>
- Jacob D, Petersen J, Eggert B, Alias A, Christensen OB et al. (2014) EURO-CORDEX: new high-resolution climate change projections for European impact research. *Regional Environmental Change* 14(2):563–578. <https://doi.org/10.1007/s10113-013-0499-2>
- Jönsson P, Eklundh L. (2004) TIMESAT – A program for analyzing time-series of satellite sensor data. *Comput Geosci* 30(8):833–845. <https://doi.org/10.1016/j.cageo.2004.05.006>
- Jorda-Capdevila D, Gampe D, Huber García V, Ludwig R, Sabater S et al. (2019) Impact and mitigation of global change on freshwater-related ecosystem services in Southern Europe. *Sci Tot Envir* 651(Part 1):895–908. <https://doi.org/10.1016/j.scitotenv.2018.09.228>

- Juez C, Garijo N, Hassan MA, Nadal-Romero E (2021) Intraseasonal-to-Interannual Analysis of Discharge and Suspended Sediment Concentration Time-Series of the Upper Changjiang (Yangtze River). *Water Resour Res* 57:e2020WR029457. <https://doi.org/https://doi.org/10.1029/2020WR029457>
- Kaltofen M, Koch H, Schramm M, Grünwald U, Kaden S (2004) Anwendung eines Langfristbewirtschaftungsmodells für multikriterielle Bewertungsverfahren – Szenarien des globalen Wandels im bergbaugeprägten Spreengebiet. *Hydrologie und Wasserbewirtschaftung* 48(2):60–70. <https://www.hywa-online.de/download/gesamtes-hywa-heft-2-2004/> – Last accessed in February 2023.
- Kim D, Lee W-S, Kim ST, Chun JA (2019) Historical Drought Assessment Over the Contiguous United States Using the Generalized Complementary Principle of Evapotranspiration. *Water Resour Res* 55(7):6244–6267. <https://doi.org/10.1029/2019WR024991>
- Kleschenko AD, Zoidze EK (2005) Monitoring Agricultural Drought in Russia. In: Boken V, Cracknell A, Heathcote R (eds) *Monitoring and Predicting Agricultural Drought: A Global Study*. Oxford, pp 196–207. ISBN 978-0-197562109 (online) 978-0-195162349 (print). <https://doi.org/10.1093/oso/9780195162349.003.0024>
- Kohlenstatistik (2019) *Der Kohlenbergbau in der Energiewirtschaft der Bundesrepublik Deutschland im Jahre 2018*. Statistik der Kohlenwirtschaft e.V., Essen and Bergheim, 88 pp. https://kohlenstatistik.de/wp-content/uploads/2019/10/Kohlenwirt_Silberheft_final.pdf – Last accessed in February 2023.
- Kotlarski S, Keuler K, Christensen OB, Colette A, Déqué M et al. (2014) Regional climate modeling on European scales: A joint standard evaluation of the EURO-CORDEX RCM ensemble. *Geosci Model Dev* 7:1297–1333. <https://doi.org/10.5194/gmd-7-1297-2014>
- Kottek M, Grieser J, Beck C, Rudolf B, Rubel F (2006) World Map of the Köppen-Geiger climate classification updated. *Meteorologische Zeitschrift* 15(3): 259–263. <https://doi.org/10.1127/0941-2948/2006/0130>
- Krysanova V, Müller-Wohlfeil DI, Becker A (1998) Development and test of a spatially distributed hydrological/water quality model for mesoscale watersheds. *Ecological Modelling* 106(2–3):261–289. [https://doi.org/10.1016/S0304-3800\(97\)00204-4](https://doi.org/10.1016/S0304-3800(97)00204-4).
- Krysanova V, Wechsung F, Arnold J, Srinivasan R, Williams (2000) SWIM (Soil and Water Integrated Model) User Manual. PIK Report 69. Potsdam Institute for Climate Impact Research, Potsdam, 239 pp. <https://www.pik-potsdam.de/en/output/publications/pikreports/.files/pr69.pdf> – Last accessed in February 2023.
- Labat D, Ronchail J, Guyot JL (2005) Recent advances in wavelet analysis: Part 2 – Amazon, Parana, Orinoco and Congo discharges time scale variability. *J Hydrol* 314(314):289–311. <https://doi.org/10.1016/j.jhydrol.2005.04.004>
- Lal R (2004) Soil carbon sequestration impacts on global climate change and food security. *Science* 304(5677):1623–1627. <https://doi.org/10.1126/science.1097396>
- Lal R (2008) Carbon sequestration. *Philos Trans R Soc B Biol Sci* 363(1492):815–830. <https://doi.org/10.1098/rstb.2007.2185>
- Lange S (2019) Trend-preserving bias adjustment and statistical downscaling with ISIMIP3BASD (v1.0). *Geoscientific Model Development* 12(7):3055–3070. <https://doi.org/10.5194/gmd-12-3055-2019>.

- Lansu EM, van Heerwaarden CC, Stegehuis AI, Teuling AJ (2020) Atmospheric Aridity and Apparent Soil Moisture Drought in European Forest During Heat Waves. *Geophys Res Lett* 47(8):e2020GL087091. <https://doi.org/10.1029/2020GL087091>
- Lastrada E, Cobos G, Torrijo FJ (2020) Analysis of Climate Change's Effect on Flood Risk. Case Study of Reinosa in the Ebro River Basin. *Water* 12(4):1114. <https://doi.org/10.3390/w12041114>
- Lesk C, Anderson W, Rigden A, Coast O, Jägermeyr J, McDermid S, Davis KF, Konar M (2022) Compound heat and moisture extreme impacts on global crop yields under climate change. *Nature Reviews Earth & Environment* 3(12):872–889. <https://doi.org/10.1038/s43017-022-00368-8>
- Li J, Huo R, Chen H, Zhao Y, Zhao T (2021) Comparative Assessment and Future Prediction Using CMIP6 and CMIP5 for Annual Precipitation and Extreme Precipitation Simulation. *Front Earth Sci* 9:430. <https://doi.org/10.3389/feart.2021.687976>
- Liu Y, Pan Z, Zhuang Q, Miralles DG, Teuling AJ et al. (2015) Agriculture intensifies soil moisture decline in Northern China. *Sci Rep* 5:11261. <https://doi.org/10.1038/srep11261>
- LMBV (2021) Flutungsmanagement. Web page. Lausitzer und Mitteldeutsche Bergbau-Verwaltungsgesellschaft (LMBV), Senftenberg. <https://www.lmbv.de/aufgaben/wassermanagement/flutungsmanagement/> – Accessed in September 2022.
- LfU (2015) Deutsches Gewässerkundliches Jahrbuch 1999 Elbegebiet, Teil II Havel mit deutschem Odergebiet. Landesamt für Umwelt, Gesundheit und Verbraucherschutz, Potsdam, 234 pp. <https://lfu.brandenburg.de/lfu/de/ueber-uns/veroeffentlichungen/detail/~01-01-2000-deutsches-gewaesserkundliches-jahrbuch-1999> – Last accessed in February 2023.
- Lobell DB, Field CB (2007) Global scale climate–crop yield relationships and the impacts of recent warming. *Environ Res Lett* 2:014002. <https://doi.org/10.1088/1748-9326/2/1/014002>
- Lobell DB, Field CB, Cahill KN, Bonfils C (2006) Impacts of future climate change on California perennial crop yields: Model projections with climate and crop uncertainties. *Agric For Meteorol* 141:208–218. <https://doi.org/10.1016/j.agrformet.2006.10.006>
- Lobell DB, Hammer GL, Chenu K, Zheng B, McLean G, Chapman SC (2015) The shifting influence of drought and heat stress for crops in northeast Australia. *Glob Chang Biol* 21(11):4115–4127. <https://doi.org/10.1111/gcb.13022>
- Lobell DB, Schlenker W, Costa-Roberts J (2011) Climate Trends and Global Crop Production Since 1980. *Science* 333(6042):616–620. <https://doi.org/10.1126/science.1204531>
- López-Moreno JI, Zabalza J, Vicente-Serrano SM, Revuelto J, Gilaberte M et al. (2015) Impact of climate and land use change on water availability and reservoir management: Scenarios in the Upper Aragón River, Spanish Pyrenees. *Sci Tot Envir* 493:1222–1231. <https://doi.org/10.1016/j.scitotenv.2013.09.031>
- Lüttger AB, Feike T (2018) Development of heat and drought related extreme weather events and their effect on winter wheat yields in Germany. *Theor Appl Climatol* 132:15–29. <https://doi.org/10.1007/s00704-017-2076-y>
- Maček U, Bezak N, Šraj M (2018) Reference evapotranspiration changes in Slovenia, Europe. *Agric For Meteorol* 260–261:183–192. <https://doi.org/10.1016/j.agrformet.2018.06.014>

- McDowell NG, Brodribb TJ, Nardini A (2019) Hydraulics in the 21st century. *New Phytol* 224:537–542. <https://doi.org/https://doi.org/10.1111/nph.16151>
- McDowell NG, Fisher RA, Xu C, Domec JC, Hölttä T et al. (2013) Evaluating theories of drought-induced vegetation mortality using a multimodel-experiment framework. *New Phytol* 200(2):304–321. <https://doi.org/10.1111/nph.12465>
- McKee, T.B., Doesken, N.J., Kleist, J., 1993. The relationship of drought frequency and duration to time scales. *Proceedings of the Eighth Conference on Applied Climatology*, 17–22 January 1993, Anaheim, CA. https://www.droughtmanagement.info/literature/AMS_Relationship_Drought_Frequency_Duration_Time_Scales_1993.pdf – Last accessed in February 2023.
- Menezes-Silva PE, Loram-Lourenço L, Barros Alves RDF, Ferreira Sousa L, da Silva Almeida SE, Santos Farnese F (2019) Different ways to die in a changing world: Consequences of climate change for tree species performance and survival through an ecophysiological perspective. *Ecol Evol* 9(20):11,979–11,999. <https://doi.org/10.1002/ece3.5663>
- Menne MJ, Durre I, Vose RS, Gleason BE, Houston TG (2012) An Overview of the Global Historical Climatology Network-Daily Database. *J Atmos Ocean Technol* 29:897–910. <https://doi.org/10.1175/JTECH-D-11-00103.1>
- Meresa H, Donegan S, Golian S, Murphy C (2022) Simulated Changes in Seasonal and Low Flows with Climate Change for Irish Catchments. *Water* 14(10):1556. <https://doi.org/10.3390/w14101556>
- Mestre O, Domonkos P, Picard F, Auer I, Robin S et al. (2013) HOMER: A homogenization software – methods and applications. *Időjárás* 117(1):47–67. <https://www.met.hu/downloads.php?fn=/metadmin/newspaper/2013/04/117-1-4-mestre.pdf> – Last accessed in February 2023.
- Moore FC, Lobell DB (2015) The fingerprint of climate trends on European crop yields. *PNAS* 112(9):2670–2675. <https://doi.org/10.1073/pnas.1409606112>
- Moreno-Chamarro E, Caron L-P, Ortega P, Loosveldt Tomas S, Roberts MJ (2021) Can we trust CMIP5/6 future projections of European winter precipitation? *Environmental Research Letters* 16(5):054063. <https://doi.org/10.1088/1748-9326/abf28a>
- Morgan JA, Pataki DE, Körner C, Clark H, Del Grosso SJ et al. (2004) Water relations in grassland and desert ecosystems exposed to elevated atmospheric CO₂. *Oecologia* 140:11–25. <https://doi.org/10.1007/s00442-004-1550-2>
- Morrissey P, Nolan P, McCormack T, Johnston P, Naughton O et al. (2021) Impacts of climate change on groundwater flooding and ecohydrology in lowland karst. *Hydrol Earth Syst Sci* 25(4):1923–1941. <https://doi.org/10.5194/hess-25-1923-2021>
- Mueller L, Schindler U, Behrendt A, Eulenstein F, Dannowski R et al. (2007) The Muencheberg Soil Quality Rating (SQR) – Field manual for detecting and assessing properties and limitations of soils for cropping and grazing. Leibniz-Centre for Agricultural Landscape Research (ZALF), Müncheberg, 103 pp. https://www.zalf.de/de/forschung_lehre/publikationen/Documents/Publikation_Mueller_L/field_mueller.pdf – Last accessed in February 2023.
- Naumann G, Alfieri L, Wyser K, Mentaschi L, Betts RA et al. (2018) Global Changes in Drought Conditions Under Different Levels of Warming. *Geophys Res Lett* 45:3285–3296. <https://doi.org/10.1002/2017GL076521>

Nolan P, Flanagan J (2020) High-resolution Climate Projections for Ireland – A Multi-model Ensemble Approach. Research Report 339. Environmental Protection Agency, Dublin, 81 pp. ISBN 978-1-84095-934-5. <https://www.epa.ie/publications/research/climate-change/research-339-high-resolution-climate-projections-for-ireland--a-multi-model-ensemble-approach.php> – Last accessed in February 2023.

Nolan P, McKinstry A (2020) EC-Earth Global Climate Simulations: Ireland's Contributions to CMIP6. Research Report 310. Environmental Protection Agency, Dublin, 149 pp. ISBN 978-1-84095-891-1. <https://www.epa.ie/publications/research/climate-change/research-310-ec-earth-global-climate-simulations-irelands-contributions-to-cmip6.php> – Last accessed in February 2023.

O'Connor P, Murphy C, Matthews T, Wilby RL (2021) Reconstructed monthly river flows for Irish catchments 1766–2016. *Geoscience Data Journal* 8(1):34–54. <https://doi.org/10.1002/gdj3.107>

O'Connor P, Murphy C, Matthews T, Wilby RL (2022) Historical droughts in Irish catchments 1767–2016. *International Journal of Climatology* 42(11):5442–5466. <https://doi.org/10.1002/joc.7542>

O'Connor P, Murphy C, Matthews T, Wilby RL (2023) Relating drought indices to impacts reported in newspaper articles. *International Journal of Climatology* – in press. <https://doi.org/10.1002/joc.7946>

O'Driscoll C, Ledesma JIJ, Coll J, Murnane JG, Nolan P et al. (2018) Minimal climate change impacts on natural organic matter forecasted for a potable water supply in Ireland. *Sci Tot Envir* 630:869–877. <https://doi.org/10.1016/j.scitotenv.2018.02.248>

O'Leary M, Geoghegan A, O'Donovan MO, Shalloo L (2017) PastureBase Ireland – Increasing Grass Utilization on Irish Dairy Farms. Teagasc, Moorepark, Fermoy, Co. Cork, 3 pp. <https://www.teagasc.ie/media/website/crops/grassland/PastureBase-Ireland-Open-Day-paper-final-draft.pdf> – Last accessed in February 2023.

Obladen N, Dechering P, Skiadaresis G, Tegel W, Keßler J et al. (2021) Tree mortality of European beech and Norway spruce induced by 2018–2019 hot droughts in central Germany. *Agricultural and Forest Meteorology* 307:108482. <https://doi.org/10.1016/j.agrformet.2021.108482>

Olesen JE, Trnka M, Kersebaum KC, Skjelvåg AO, Seguin B et al. (2011) Impacts and adaptation of European crop production systems to climate change. *Eur J Agron* 34:96–112. <https://doi.org/10.1016/j.eja.2010.11.003>

Páscoa P, Gouveia CM, Russo AC, Bojariu R, Vicente-Serrano SM, Trigo RM (2020) Drought impacts on vegetation in southeastern Europe. *Remote Sens* 12(13):2156 <https://doi.org/10.3390/rs12132156>

Pebesma EJ (2004) Multivariable geostatistics in S: the gstat package. *Computers & Geosciences* 30(7):683–691. <https://doi.org/10.1016/j.cageo.2004.03.012>

Peel MC, Finlayson BL, McMahon TA (2007) Updated world map of the Köppen–Geiger climate classification. *Hydrology and Earth System Sciences* 11(5):1633–1644. <https://doi.org/10.5194/hess-11-1633-2007>

Peña-Angulo D, Vicente-Serrano SM, Dominguez-Castro F, Noguera I, Tomas-Burguera M et al. (2021) Unravelling the role of vegetation on the different trends between climatic and hydrologic drought in headwater catchments of Spain. *Anthropocene* 36:100309. <https://doi.org/10.1016/j.ancene.2021.100309>

- Peng S, Huang J, Sheehy JE, Laza RC, Visperas RM et al. (2004) Rice yields decline with higher night temperature from global warming. *PNAS* 101:9971–9975. <https://doi.org/10.1073/pnas.0403720101>
- Peters W, van der Velde IR, van Schaik E, Miller JB, Ciais P et al. (2018) Increased water-use efficiency and reduced CO₂ uptake by plants during droughts at a continental scale. *Nat Geosci* 11:744–748. <https://doi.org/10.1038/s41561-018-0212-7>
- Piniewski M, Eini MR, Chattopadhyay S, Okruszko T, Kundzewicz ZW (2022) Is there a coherence in observed and projected changes in riverine low flow indices across Central Europe? *Earth-Science Reviews* 233:104187. <https://doi.org/10.1016/j.earscirev.2022.104187>.
- Pomerleau J, Mckee M, Rose R, Haerpfer CW, Rotman D, Tumanov S (2008) Hazardous alcohol drinking in the former Soviet Union: A cross-sectional study of eight countries. *Alcohol and Alcoholism* 43(3):351–359. <https://doi.org/10.1093/alcalc/agm167>
- Potop V (2011) Evolution of drought severity and its impact on corn in the Republic of Moldova. *Theor Appl Climatol* 105:469–483. <https://doi.org/10.1007/s00704-011-0403-2>
- Potop V, Boroneanț C, Možný M, Štěpánek P, Skalák P (2014) Observed spatiotemporal characteristics of drought on various time scales over the Czech Republic. *Theor Appl Climatol* 115:563–581. <https://doi.org/10.1007/s00704-013-0908-y>
- Potopová V, Boroneanț C, Boincean B, Soukup J (2016) Impact of agricultural drought on main crop yields in the Republic of Moldova. *Int J Climatol* 36:2063–2082. <https://doi.org/10.1002/joc.4481>
- Potopová V, Trnka M, Hamouz P, Soukup J, Castravet T (2020) Statistical modelling of drought-related yield losses using soil moisture-vegetation remote sensing and multiscalar indices in the south-eastern Europe. *Agric Water Manag* 236:106168. <https://doi.org/10.1016/j.agwat.2020.106168>
- Ramos MC (2006) Soil water content and yield variability in vineyards of Mediterranean northeastern Spain affected by mechanization and climate variability. *Hydrol Process* 20:2271–2283. <https://doi.org/10.1002/hyp.5990>
- Ramos MC, Jones GV, Martínez-Casasnovas JA (2008) Structure and trends in climate parameters affecting winegrape production in northeast Spain. *Clim Res* 38:1–15. <https://doi.org/10.3354/cr00759>
- Ramos MC, Martínez-Casasnovas JA (2010) Effects of precipitation patterns and temperature trends on soil water available for vineyards in a Mediterranean climate area. *Agric Water Manag* 97:1495–1505. <https://doi.org/10.1016/j.agwat.2010.05.003>
- Rauthe M, Steiner H, Riediger U, Mazurkiewicz A, Gratzki A (2013) A Central European precipitation climatology – Part I: Generation and validation of a high-resolution gridded daily data set (HYRAS). *Meteorologische Zeitschrift* 22(3):235–256. <https://doi.org/10.1127/0941-2948/2013/0436>
- Sah RP, Chakraborty M, Prasad K, Pandit M, Tudu VK et al. (2020) Impact of water deficit stress in maize: Phenology and yield components. *Sci Rep* 10:2944. <https://doi.org/10.1038/s41598-020-59689-7>
- Samaniego L, Thober S, Kumar R, Wanders N, Rakovec O et al. (2018) Anthropogenic warming exacerbates European soil moisture droughts. *Nat Clim Change* 8:421–426. <https://doi.org/10.1038/s41558-018-0138-5>

- Schlenker W, Roberts MJ (2009) Nonlinear temperature effects indicate severe damages to U.S. crop yields under climate change. *PNAS* 106:15,594–15,598. <https://doi.org/10.1073/pnas.0906865106>
- Schoenheinz D, Grünwald U, Koch H (2011) Aspects of Integrated Water Resources Management in River Basins Influenced by Mining Activities in Lower Lusatia. *Die Erde – Journal of the Geographical Society of Berlin* 142(1–2):163–186. <https://www.die-erde.org/index.php/die-erde/article/view/47> – Last accessed in February 2023.
- Senatsverwaltung (2019) Bevölkerungsprognose für Berlin und die Bezirke 2018–2030. Senatsverwaltung für Stadtentwicklung und Wohnen Ref. I A – Stadtentwicklungsplanung in Zusammenarbeit mit dem Amt für Statistik Berlin-Brandenburg, Berlin, 41 pp. <https://www.demografie-portal.de/DE/Service/Publikationen/2019/bevoelkerungsprognose-fuer-berlin-und-die-Bezirke-2018-2030.pdf> – Last accessed in February 2023.
- Seneviratne SI, Corti T, Davin EL, Hirschi M, Jaeger EB et al. (2010) Investigating soil moisture-climate interactions in a changing climate: A review. *Earth-Science Rev* 99:125–161. <https://doi.org/10.1016/j.earscirev.2010.02.004>
- Siebert S, Ewert F (2014) Future crop production threatened by extreme heat. *Environmental Research Letters* 9(4):041001. <https://doi.org/10.1088/1748-9326/9/4/041001>
- Smart DR, Schwass E, Lakso A, Morano L (2006) Grapevine rooting patterns: A comprehensive analysis and a review. *Am J Enol Vitic* 57(1):89–104. <https://doi.org/10.5344/ajev.2006.57.1.89>
- Sordo-Ward A, Granados A, Iglesias A, Garrote L, Bejarano MD (2019) Adaptation Effort and Performance of Water Management Strategies to Face Climate Change Impacts in Six Representative Basins of Southern Europe. *Water* 11(5):1078. <https://doi.org/10.3390/w11051078>
- Spinoni J, Barbosa P, Buchignani E, Cassano J, Cavazos T et al. (2020) Future Global Meteorological Drought Hot Spots: A Study Based on CORDEX Data. *J Clim* 33:3635–3661. <https://doi.org/10.1175/JCLI-D-19-0084.1>
- Spinoni J, Vogt JV, Naumann G, Barbosa P, Dosio A (2018) Will drought events become more frequent and severe in Europe? *Int J Climatol* 38:1718–1736. <https://doi.org/10.1002/joc.5291>
- Sulman BN, Roman DT, Yi K, Wang L, Phillips RP (2016) High atmospheric demand for water can limit forest carbon uptake and transpiration as severely as dry soil. *Geophys Res Lett* 43:9686–9695. <https://doi.org/10.1002/2016GL069416>
- Tebaldi C, Lobell DB (2008) Towards probabilistic projections of climate change impacts on global crop yields. *Geophys Res Lett* 35(8):L08705. <https://doi.org/10.1029/2008GL033423>
- Terray L, Demory M-E, Déqué M, de Coetlogon G, Maisonnave E (2004) Simulation of late-twenty-first-century changes in wintertime atmospheric circulation over Europe due to anthropogenic causes. *J Clim* 17:4630–4635. <https://doi.org/10.1175/JCLI-3244.1>
- Teuling AJ, Seneviratne SI, Williams C, Troch PA (2006) Observed timescales of evapotranspiration response to soil moisture. *Geophys Res Lett* 33(23):L23403. <https://doi.org/10.1029/2006GL028178>
- Teuling AJ, Van Loon AF, Seneviratne SI, Lehner I, Aubinet M et al. (2013) Evapotranspiration amplifies European summer drought. *Geophys Res Lett* 40(10):2071–2075. <https://doi.org/10.1002/grl.50495>

- Torrence C, Compo GP (1998) A Practical Guide to Wavelet Analysis. *Bull Am Meteorol Soc* 79:61–78. [https://doi.org/10.1175/1520-0477\(1998\)079<0061:APGTWA>2.0.CO;2](https://doi.org/10.1175/1520-0477(1998)079<0061:APGTWA>2.0.CO;2)
- UFZ (2022) Dürremonitor Deutschland [Drought Monitor Germany]. Website with downloadable data. Helmholtz Zentrum für Umweltforschung, Leipzig. <https://www.ufz.de/index.php?de=37937> – Accessed in September 2022.
- Vautard R, Kadygrov N, Iles C, Boberg F, Buonomo E et al. (2021) Evaluation of the Large EURO-CORDEX Regional Climate Model Ensemble. *JGR Atmospheres* 126(17):e2019JD032344. <https://doi.org/10.1029/2019JD032344>
- Vicente-Serrano SM, Beguería S, López-Moreno JI (2010) A multiscalar drought index sensitive to global warming: The standardized precipitation evapotranspiration index. *J Clim* 23(7):1696–1718. <https://doi.org/10.1175/2009JCLI2909.1>
- Vicente-Serrano SM, Azorin-Molina C, Sanchez-Lorenzo A, Revuelto J, López-Moreno JI et al. (2014) Reference evapotranspiration variability and trends in Spain, 1961–2011. *Glob Planet Change* 121:26–40. <https://doi.org/10.1016/j.gloplacha.2014.06.005>
- Vicente-Serrano S, McVicar TR, Miralles DG, Yang Y, Tomas-Burguera M (2020) Unraveling the influence of atmospheric evaporative demand on drought and its response to climate change. *WIREs Clim Chang* 11:e632. <https://doi.org/10.1002/wcc.632>
- Vicente-Serrano SM, Peña-Angulo D, Murphy C, López-Moreno JI, Tomas-Burguera M (2021a) The complex multi-sectoral impacts of drought: Evidence from a mountainous basin in the Central Spanish Pyrenees. *Science of The Total Environment* 769:144702. <https://doi.org/10.1016/j.scitotenv.2020.144702>
- Vicente-Serrano S, Domínguez-Castro F, Murphy C, Hannaford J, Reig F et al. (2021b) Long term variability and trends of droughts in Western Europe (1851–2018). *Int J Climatol* 41(S1):E690–E717. <https://doi.org/10.1002/joc.6719>
- Vicente-Serrano SM, Domínguez-Castro F, Murphy C, Peña-Angulo D, Tomas-Burguera M et al. (2021c) Increased Vegetation in Mountainous Headwaters Amplifies Water Stress During Dry Periods. *Geophysical Research Letters* 48(18):e2021GL094672. <https://doi.org/10.1029/2021GL094672>
- Vicente-Serrano SM, García-Herrera R, Peña-Angulo D, Tomas-Burguera M, Domínguez-Castro F et al. (2022) Do CMIP models capture long-term observed annual precipitation trends? *Climate Dynamics* 58(9–10):2825–2842. <https://doi.org/10.1007/s00382-021-06034-x>
- Wang H, Vicente-Serrano SM, Tao F, Zhang X, Wang P et al. (2016) Monitoring winter wheat drought threat in Northern China using multiple climate-based drought indices and soil moisture during 2000–2013. *Agric For Meteorol* 228–229:1–12. <https://doi.org/10.1016/j.agrformet.2016.06.004>
- Wasserportal Berlin (2022a) Wasserportal Gewässerkundliche Messdaten - Sophienwerder - Durchfluss. Website. <https://wasserportal.berlin.de/station.php?anzeige=dd&station=5827700&stable=odf> – Accessed in September 2022.
- Wasserportal Berlin (2022b) Wasserportal Gewässerkundliche Messdaten - Tiefwerder - Durchfluss. Website. <https://wasserportal.berlin.de/station.php?anzeige=dd&station=5803200&stable=ows> – Accessed in September 2022.
- Willuweit L, O’Sullivan JJ, Shahumyan H (2016) Simulating the effects of climate change, economic and urban planning scenarios on urban runoff patterns of a metropolitan region. *Urb Water J* 13(8):803–818. <https://doi.org/10.1080/1573062X.2015.1036086>

Winterrath T, Brendel C, Hafer M, Junghänel T, Klameth A et al. (2018) Radar climatology (RADKLIM) version 2017.002; gridded precipitation data for Germany: Radar-based gauge-adjusted one-hour precipitation sum (RW). Dataset, including extensions up to 2020-12. Deutscher Wetterdienst, Offenbach on Main. https://doi.org/10.5676/DWD/RADKLIM_RW_V2017.002 – Last accessed in February 2023.

World Bank (2021) Special Focus Note: Moldova's Vulnerability to Natural Disasters and Climate Risks. The World Bank, Washington, DC. Online document, 3 pp. <https://thedocs.worldbank.org/en/doc/7bf12b95f10a3daf7b570718b2100e15-0080012021/related/MEU-DRM-Special-Topic-May-2021-FINAL-eng-Copy.pdf> – Last accessed in February 2023.

Wriedt, G. (2020) Grundwasserbericht Niedersachsen: Sonderausgabe zur Grundwasserstandssituation in den Trockenjahren 2018 und 2019. vol 41. Cloppenburg: Niedersächsischer Landesbetrieb für Wasserwirtschaft, Küsten- und Naturschutz, Norden, 31 pp. https://www.nlwkn.niedersachsen.de/download/156169/NLWKN_2020_Grundwasserbericht_Niedersachsen_Sonderausgabe_zur_Grundwasserstandssituation_in_den_Trockenjahren_2018_und_2019_Band_41_.pdf – Last accessed in February 2023.

Xu Z, Jiang Y, Jia B, Zhou G (2016) Elevated-CO₂ response of stomata and its dependence on environmental factors. *Front Plant Sci* 7:657. <https://doi.org/10.3389/fpls.2016.00657>

Zampieri M, Ceglar A, Dentener F, Toreti A (2017) Wheat yield loss attributable to heat waves, drought and water excess at the global, national and subnational scales. *Environ Res Lett* 12:064008. <https://doi.org/10.1088/1748-9326/aa723b>

Zappa G, Shepherd TG (2017) Storylines of atmospheric circulation change for European regional climate impact assessment. *J Clim* 30:6561–6577. <https://doi.org/10.1175/JCLI-D-16-0807.1>